

(4)

AD-A207 727

CONTRACT REPORT BRL-CR-607

BRL

MODELING OF HOT FRAGMENT CONDUCTIVE IGNITION
OF SOLID PROPELLANTS WITH APPLICATION TO MELTING
AND EVAPORATION OF SOLIDS

DTIC
SELECTED
MAY 16 1989
S D
(b) D

K. K. KUO
W. H. HSIEH
K. C. HSIEH

~~MARCH 1989~~
Dec. 1988

APPROVED FOR PUBLIC RELEASE; DISTRIBUTION UNLIMITED.

U.S. ARMY LABORATORY COMMAND
BALLISTIC RESEARCH LABORATORY
ABERDEEN PROVING GROUND, MARYLAND

88 10 081

UNCLASSIFIED

SECURITY CLASSIFICATION OF THIS PAGE

Form Approved
OMB No. 0704-0188

AD P.307 727

REPORT DOCUMENTATION PAGE			
1a. REPORT SECURITY CLASSIFICATION UNCLASSIFIED		1b. RESTRICTIVE MARKINGS	
2a. SECURITY CLASSIFICATION AUTHORITY		3. DISTRIBUTION/AVAILABILITY OF REPORT Approved for public release; distribution unlimited	
2b. DECLASSIFICATION/DOWNGRADING SCHEDULE		5. MONITORING ORGANIZATION REPORT NUMBER(S)	
4. PERFORMING ORGANIZATION REPORT NUMBER(S) BRL-CR-607		6a. NAME OF PERFORMING ORGANIZATION Data Base	
6c. ADDRESS (City, State, and ZIP Code) Suite 426-B 315 S. Allen St. State College, PA 16801		6b. OFFICE SYMBOL (If applicable) SLCBR-IBD	
7a. NAME OF MONITORING ORGANIZATION USA Ballistic Research Lab		7b. ADDRESS (City, State, and ZIP Code) APG, MD 21005-5066	
8a. NAME OF FUNDING/SPONSORING ORGANIZATION USA Ballistic Research Lab		8b. OFFICE SYMBOL (If applicable) SLCBR-IBD	
8c. ADDRESS (City, State, and ZIP Code) APG, MD 21005-5066		9. PROCUREMENT INSTRUMENT IDENTIFICATION NUMBER	
10. SOURCE OF FUNDING NUMBERS			
		PROGRAM ELEMENT NO.	PROJECT NO.
		TASK NO.	WORK UNIT ACCESSION NO.
11. TITLE (Include Security Classification) Modeling of Hot Fragment Conductive Ignition of Solid Propellants With Application to Melting and Evaporation of Solids			
12. PERSONAL AUTHOR(S) K. K. Kuo, W. H. Hsieh, and K. C. Hsieh			
13a. TYPE OF REPORT Contractor Report	13b. TIME COVERED FROM _____ TO _____	14. DATE OF REPORT (Year, Month, Day) 88 Dec	15. PAGE COUNT
16. SUPPLEMENTARY NOTATION			
17. COSATI CODES	18. SUBJECT TERMS (Continue on reverse if necessary and identify by block number)		
FIELD	GROUP	SUB-GROUP	
19. ABSTRACT (Continue on reverse if necessary and identify by block number) A comprehensive theoretical model has been formulated for studying the degree of vulnerability of various solid propellants being heated by hot spall fragments. The model stimulates the hot fragment conductive ignition (HFCI) processes caused by direct contact of hot inert particles with solid propellant samples. The model describes the heat transfer and displacement of the hot particle, the generation of the melt (or foam) layer caused by the liquefaction, pyrolysis, and decomposition of the propellant, and the regression of the propellant as well as the time variation of its temperature distributions. To partially validate the theoretical model in the absence of the necessary chemical kinetic data, an ice-melting and evaporation experiment was designed and conducted. These experiments provide features of the conductive heating, melting, and evaporating processes. Calculated results compare well with experimental data in temperature-time traces, spall particle-sinking velocity, and displacement.			
(n/a)			
20. DISTRIBUTION/AVAILABILITY OF ABSTRACT <input checked="" type="checkbox"/> UNCLASSIFIED/UNLIMITED <input type="checkbox"/> SAME AS RPT <input type="checkbox"/> DTIC USERS		21. ABSTRACT SECURITY CLASSIFICATION UNCLASSIFIED	
22a. NAME OF RESPONSIBLE INDIVIDUAL Martin Miller		22b. TELEPHONE (Include Area Code) (301) 278-6156	22c. OFFICE SYMBOL SLCBR-IBD

Acknowledgment

This work was performed under Contract DAAK11-83-C-0015 sponsored by the Applied Ballistics Branch of the Ballistics Research Laboratories, under the management of Dr. Joseph J. Rocchio, Dr. Martin S. Miller, and Mr. Norman Gerri. The authors would also like to acknowledge Drs. Martin S. Miller and Art Cohen of BRL for many helpful discussions during this research investigation. We would like to thank Dr. Miller for supplying DSC results and kinetic data for XM 39 propellant used as input parameters to the computer code. We would also like to thank Dr. Cohen for his help in supplying HFCI experimental data for model validation. The support and encouragement of Dr. Rocchio is highly appreciated.

We would also like to thank Mrs. Mary Jane Coleman and Mrs. Ginny Smith for clerical assistance throughout this project.



Request for	
TIS CR-81	
TAS	
Distribution	
Approved	
By	
Dist	
Availability Dates	
Dist	Actual Author Special
A-1	

CONTENTS

	<u>Page</u>
ACKNOWLEDGEMENT	
LIST OF FIGURES	v
1 INTRODUCTION	1
ATTACHMENT 1	3
ATTACHMENT 2	45
ATTACHMENT 3	63
ATTACHMENT 4	77
DISTRIBUTION LIST	79

FIGURES

	<u>Page</u>
1. Physical event of hot fragment conductive ignition (HFCI) processes represented by various cases in two different time periods	32
2. Schematic diagram of model	33
3a. Energy fluxes associated with the gas phase in region 1	34
3b. Energy fluxes associated with the liquid phase in region 1	35
4. Temperature distributions in a cylindrical shaped spall particle	36
5. Measured temperature-time traces from ice melting and evaporating experiments	37
6. A color schlieren photograph of ice melting and evaporating experiment	38
7. Comparison of calculated sinking velocity of the spall particle with the measured data obtained from ice-melting and evaporating experiment	39
8. Comparison of calculated spall particle trajectory with data obtained from ice-melting and evaporating experiment	40
9. Comparison of the measured temperature-time trace of TC2 with calculated temperature-time traces at the spall-particle base, TC2 and maximum temperature locations of the spall particle	41
10. Calculated radial temperature profiles at the top surface, middle section, and bottom surface locations of the spall particle for various times	42
11. Calculated temperature profiles in the ice block at various times	43
12. Calculated time variation of heat fluxes \dot{q}_{spall}'' and \dot{q}_{pr}''	44

FINAL REPORT
Under Contract No. DAAK11-83-C-0015

K. K. Kuo, W. H. Hsieh and K. C. Hsieh

Submitted to
Ballistic Research Laboratories
Aberdeen Proving Ground, Maryland

During this contract period, substantial progress was made in the development of a comprehensive model for simulating hot fragment conductive ignition (HFCI) of low-vulnerability ammunition (LOVA) propellants. A numerical code was also developed to solve the HFCI model. The work has resulted in three major publications, included herein as Attachments 1, 2 and 3.

Attachment 1: Kuo, K. K., Hsieh, W. H., Hsieh, K. C., and Miller, M. S., "Modeling of Hot Fragment Conductive Ignition of Solid Propellants with Applications to Melting and Evaporation of Solids," to be published in Journal of Heat Transfer.
(acceptance for publication included as Attachment 4)

Attachment 2: Hsieh, K. C., Hsieh, W. H., Kuo, K. K., and Miller, M. S., "Modeling of Hot Fragment Conductive Ignition Processes of LOVA Propellants," presented at the 24th JANNAF Combustion Meeting, Naval Postgraduate School, Monterey, California, October 5 - 9, 1987.

Attachment 3: Hsieh, K. C., Hsieh, W. H., Kuo, K. K., and Miller, M. S., "Validation of a Theoretical Model for Hot Fragment Conductive Ignition Processes of LOVA Propellants," Proceedings from the 10th International Symposium on Ballistics (San Diego, California, October 27 - 29, 1987), Vol. 1, Section 2.

The model and code developed under this contract can be applied in studying the vulnerability of various propellants heated by spall fragments.

Attachment 1

Modeling of Hot Fragment Conductive Ignition
of Solid Propellants

With Applications to Melting and Evaporation of Solids

Paper No. 87-F-509

MODELING OF HOT FRAGMENT CONDUCTIVE IGNITION OF SOLID PROPELLANTS WITH APPLICATIONS TO MELTING AND EVAPORATION OF SOLIDS

K. K. KUO, W. H. HSIEH, K. C. HSIEH
Department of Mechanical Engineering
The Pennsylvania State University
University Park, Pennsylvania

M. S. Miller
U.S. Ballistics Research Laboratories
Aberdeen Proving Ground, Maryland

ABSTRACT

A comprehensive theoretical model has been formulated for studying the degree of vulnerability of various solid propellants being heated by hot spall fragments. The model simulates the hot fragment conductive ignition (HFCI) processes caused by direct contact of hot inert particles with solid propellant samples. The model describes the heat transfer and displacement of the hot particle, the generation of the melt (or foam) layer caused by the liquefaction, pyrolysis, and decomposition of the propellant, and the regression of the propellant as well as the time variation of its temperature distributions.

To partially validate the theoretical model in the absence of the necessary chemical kinetic data, an ice melting and evaporation experiment was designed and conducted. These experiments provide features of the conductive heating, melting, and evaporating processes. Calculated results compare well with experimental data in temperature-time traces, spall particle sinking velocity, and displacement.

NOMENCLATURE

A	Arrhenius frequency factor of chemical reaction of melt or foam layer in Region 1, kg/m ³ -s
A _i	Interface area between liquid melt and gas bubbles, m ²
C _p	constant-pressure specific heat, J/kg-K
C _{pr}	specific heat of LOVA propellant, J/kg-K
C _s	specific heat of spall particle, J/kg-K
D _b	averaged diameter of bubbles generated from gasification process, m
E _a	activation energy of chemical reaction of melt or foam layer, J/mole

$h_{c1,2}$	convective heat transfer coefficient on top and lateral surfaces of spall particle, $\text{W/m}^2\text{-K}$
h_{c3}	convective heat transfer coefficient on top surface of LOVA propellant, $\text{W/m}^2\text{-K}$
ΔH_f°	heat of formation, J/kg
h_{fg}	latent heat of liquid melt, J/kg
h_l	instantaneous height of melt or foam layer in Region 2, m
h_p	instantaneous distance traveled by spall particle, m
L_m	height of melt or foam layer in Region 1, m
l_s	height of the spall particle, m
m_b	rate of conversion of reactant (R) into product (P), kg/s
\dot{m}_{gB}	rate of mass generation of reactant species from the base of spall particle, kg/s
\dot{m}_{net1}	net rate of production of gaseous mass in Region 1 of foam layer, kg/s
n	order of chemical reaction in gas bubbles
p	pressure, N/m^2
q_{min}	critical heat flux for producing gaseous bubbles from melt of LOVA propellant on surface of spall particle, W/m^2
\dot{q}_{m1}	heat flux on submerged lateral surface of spall particle, W/m^2
\dot{q}_{m2}	heat flux from foam layer to LOVA propellant, W/m^2
\dot{q}_{pr}	net heat generation in LOVA propellant, W/m^3
\dot{q}_{pr}	heat flux transferred to LOVA propellant from melt or foam layer in Region 1, W/m^2
\dot{q}_{rad}	net radiant heat flux, W/m^2
q_{spall}	heat flux at base of spall particle, W/m^2
r	radial coordinate, m
R_u	Universal gas constant, $8314.4 \text{ J/kg-mole-K}$
r_m	outer radius of melt or foam layer in Region 2, m
r_s	radius of spall particle, m
$T_b (=T_{sat})$	boiling temperature of liquid melt, K
T_g	gas temperature, K
T_m	bulk temperature of melt or foam layer, K
T_{melt}	melting temperature of LOVA propellant, K
T_p	temperature of LOVA propellant, K
T_{ps}	average surface temperature of LOVA propellant exposed to air, K
T_s	temperature of spall particle, K
v_b	average axial velocity of bubbles in Region 1 of foam layer, m/s
v_{lr}	radial velocity of melt or foam layer in Region 1, m/s
v_m	axial velocity of boundary surface of melt or foam layer in Region 1, m/s

v_{mr}	outward radial velocity of foam layer in Region 2, m/s
v_s	sinking velocity of spall particle, m/s
z	axial distance above base of spall particle, m
z^*	axial distance below instantaneous surface of propellant under foam layer, m

Greek Symbols

α	thermal diffusivity, m ² /s
β	bubble contact angle, degree
λ	thermal conductivity, W/m-K
ρ	density, kg/m ³
ψ	average porosity (void fraction) of foam layer in Region 1
ϵ_s	emissivity of spall particle
σ	Stefan-Boltzmann constant, = 5.6696×10^{-8} W/m ² -K ⁴
σ_s	surface tension of liquid melt of LOVA propellant, N/m
μ	dynamic viscosity, kg/m-s
ψ_B	average void fraction of spall base surface in contact with gas bubbles

Subscripts

g	gas-phase
i	initial condition
l	liquid-phase
$melt$	liquid melt
pr	propellant
r	room condition
1	region 1 of foam layer

Superscript

$$* \quad T^* = T - T_{ref}$$

INTRODUCTION

Ignition of solid gun propellants in go/no-go tests which employ a hot metallic element of well-defined geometry as the source of energy has been a conventional method of determining the vulnerability of propellants (Gol'dshleger, 1973), especially in the Low Vulnerability Ammunition (LOVA) development program (Wise et al., 1980; Law and Rocchio, 1981; and Wise and Rocchio, 1981). Hot fragment conductive ignition (HFCI) studies help to determine the survivability of weapon systems (such as tanks, ships, etc.) containing stowed ammunition (Gol'dshleger et al., 1973; Wise et al., 1980; Law and Rocchio, 1981; and Wise and Rocchio, 1981). Ignition of propellant

charges by hot metallic spall fragments can be generated through such threats as shaped charges and kinetic energy penetrators.

Review of HFCI processes indicates that both experimental and theoretical investigations have been conducted. The experiments generally employ hot steel balls of known diameters and temperatures which are suddenly brought into contact with the propellant (Gol'dshleger et al., 1973a; Wise et al., 1980; Law and Rocchio, 1981; and Wise and Rocchio, 1981).

Gol'dshleger et al. (1973a) used a hot steel ball with a diameter of 0.4-2.5 mm and smooth surface finish ($<0.1 \mu\text{m}$) to ignite the propellant. They noted that ignition does not occur when the particle temperature is below a critical value, and that results are dependent upon contact between the hot particle and the propellant. They also proposed a theoretical model and obtained numerical solutions.

Wise et al. (1980 and 1981) and Law and Rocchio (1981) conducted similar experiments to characterize LOVA propellants. They used hot steel balls (with diameters between 3.2 and 11.1 mm), and a cluster of propellant slabs. The ignition boundary for propellants was determined in terms of minimum temperature for a given size steel ball, using go/no-go tests. Their HFCI experiments indicated that the binder composition may be one of the most important factors in the determination of LOVA propellant vulnerability.

Kirshenbaum et al. (1983) studied the sensitivity properties of various candidate LOVA propellants using various tests, including HFCI. Their study showed that LOVA candidates are significantly less susceptible to thermal ignition than conventional propellants. Caveny et al. (1973) also investigated the effect of additives on the flammability limits of propellants, investigated the effect of additives on flammability limits of propellants, and evaluated three types of additives (including coolants, char formers, and flame inhibitors) for reducing flammability.

Prior to the present study, several attempts have been made to model the ignition process encountered in HFCI experiments (Gol'dshleger et al., 1973a; Vilyunov and Kolchin, 1966; Anderson et al., 1972; Gol'dshleger et al., 1973b; Linan and Kindelan, 1981; and Tyler and Jones, 1981). However, because most of the existing models of conductive ignition employ numerous simplifying assumptions and asymptotic solution procedures, their validity and usage are limited. Grossman and Rele (1974) obtained numerical solutions for the ignition of cellulose by impingement of hot, high-velocity spherical particles. They concluded that the total energy of the metal particle (both

thermal and kinetic) is important in determining whether or not ignition occurs.

None of the theoretical models to date have attempted to describe the foam and/or melt layer which has been experimentally observed on the propellant surface in contact with hot particles. Nor has the effect of binder composition been studied in previous models. A theoretical model for simulating the ignition processes of solid propellants in HFCI tests is needed in order to evaluate new propellant formulations with respect to their ability to resist conductive ignition and thereby reduce system vulnerability.

Specific objectives of this study are: 1) to formulate a comprehensive model for simulating the ignition of solid propellants under HFCI situations; 2) to identify chemical and physical input parameters required for the model; 3) to design and conduct simplified melting and evaporation experiments to partially validate the theoretical model under special limiting conditions; and (4) to demonstrate the capability of the theoretical model to simulate ice melting and evaporation processes.

METHOD OF APPROACH

Selection of Particle Geometry and Description of Physical Events

In actual HFCI processes, the hot fragments (spall particles) generated from the penetration of shaped charge jets of armor plates are in different shapes and sizes. In order to understand the physical and chemical processes, a particular particle shape has to be selected in the formulation of the theoretical model. Since no particular shape can truly represent the actual geometry of spall fragments, any particle geometry (e.g. spherical, cylindrical, cubic, parallel piped) could be chosen. The cubic or parallel piped particles require three-dimensional and unsteady solution, which is more complex than the cylindrical and spherical cases. The spherical particle geometry seems simpler than cylindrical; however, the heat transfer process involved does not satisfy the point symmetry condition. Therefore, the cylindrical particle geometry has been selected. One additional advantage of the cylindrical spall particle is due to its flat-bottomed surface, which can easily maintain a good contact with a flat propellant surface.

Consider a typical HFCI experiment using a hot spall particle with cylindrical geometry. At time equals zero, the spall particle is placed on a cold propellant sample. In the early phase of the process (Time Period I), heat is conducted from the hot

particle to the propellant without any phase change or pyrolysis (see Fig. 1). As time progresses, the temperature of the propellant increases and that of the particle decreases. Following a period of inert heating, the propellant starts to decompose, melt, and/or gasify (Time Period II). Since the density of the metal particle is much higher than the density of the decomposed propellant, it displaces the decomposed propellant and becomes imbedded in (sinks into) the propellant, as shown in Fig. 1. The amount of imbedding depends on the temperature and size of the hot particle and the composition of the propellant. The decomposed species can further react exothermically in the gas and/or condensed (solid or liquid (foam)) phase to cause ignition. Self-sustained ignition will occur only if the heat generated by the exothermic reactions exceeds the heat losses. The entire process is strongly dependent upon the energy content of the hot particle and physicochemical properties of the propellant.

Governing Equations and Boundary Conditions. The mathematical model consists of governing equations and their associated initial and boundary conditions for the hot particle, the propellant, and the melt (or foam) layer. Figure 2 schematically shows these regions and the coordinate system. The energy equations for the hot spall particle and the propellant are as follows.

Hot spall particle:

$$\frac{\partial}{\partial t} (\rho_s C_s T_s) = \frac{1}{r} \frac{\partial}{\partial r} (\lambda_s r \frac{\partial T_s}{\partial r}) + \frac{\partial}{\partial z} (\lambda_s \frac{\partial T_s}{\partial z}) \quad (1)$$

Propellant:

$$\begin{aligned} \frac{\partial}{\partial t} (\rho_{pr} C_{pr} T_p) - v_s \frac{\partial}{\partial z} (\rho_{pr} C_{pr} T_p) &= \frac{1}{r} \frac{\partial}{\partial r} (\lambda_{pr} r \frac{\partial T_p}{\partial r}) \\ &+ \frac{\partial}{\partial z} (\lambda_{pr} \frac{\partial T_p}{\partial z}) + \dot{q}_{pr}'' \end{aligned} \quad (2)$$

During the HFCI tests, a foam layer could be generated, and the gases pyrolyzed from liquid melt may undergo exothermic chemical reactions to generate heat for further reactions. In order to take the above processes into consideration, the conservation equations for the foam region must be formulated. The following assumptions are adopted:

- 1) The liquefaction process at the interface of the propellant and liquid melt involves no gasification;

- 2) The gaseous mixtures are produced from the base of the spall particle or at the liquid-gas interfaces according to the Arrhenius rate law; and
- 3) The energy release process in the gas phase can be represented by a single-step forward reaction



where R represents the gaseous reactant mixtures, and P represents the gaseous products.

The mass continuity equation for the reactant species can be derived from consideration of mass-flux balance in region 1 of the foam layer as

$$\begin{aligned} \frac{D}{Dt} (\gamma_R \rho_{g_1} \psi L_m \pi r_s^2) &= -2\pi r_s L_m \gamma_R \rho_{g_1} v_{lr} \psi \\ &+ \dot{m}_{g_{net1}} + \dot{m}_{g_B} - \dot{m}_b \end{aligned} \quad (4)$$

The mass continuity equation for the product species can be written as

$$\begin{aligned} \frac{D}{Dt} [(1 - \gamma_R) \rho_{g_1} \psi L_m \pi r_s^2] &= \\ -2\pi r_s L_m (1 - \gamma_R) \rho_{g_1} v_{lr} \psi + \dot{m}_b \end{aligned} \quad (5)$$

The source terms \dot{m}_b and $\dot{m}_{g_{net1}}$ can be expressed as follows according to the Arrhenius law,

$$\dot{m}_b = A_g \rho_{g_1} \gamma_R^n \exp\left(-\frac{E_a, g}{R_u T_{g_1}}\right) \quad (6)$$

$$\dot{m}_{g_{net1}} = A_{lg} A_{i_1} \rho_i \exp\left(-\frac{E_{a, lg}}{R_u T_{i_1}}\right) \quad (7)$$

where A_{lg} represents the Arrhenius coefficient of the reaction at the interface of liquid and gas phases.

The mass continuity equation for the liquid phase of the foam layer in region 1 can be given as

$$\frac{D}{Dt} [\rho_{g_1} (1 - \Psi) L_m \pi r_s^2] = -2\pi r_s L_m \rho_{g_1} v_{lr} (1 - \Psi) - \dot{m}_{g_{net_1}} + \dot{m}_{g_B} + \rho_{pr} \pi r_s^2 (-v_m) \quad (8)$$

Rearranging equations (4) and (5), one can obtain the following equation.

$$\frac{DY_R}{Dt} = \frac{1}{\rho_{g_1} \Psi L_m \pi r_s^2} [(1 - Y_R)(\dot{m}_{g_{net_1}} + \dot{m}_{g_B}) - \dot{m}_b] \quad (9)$$

By considering the energy fluxes shown in Fig. 3a, one can derive the following equation describing the rate of accumulation of the gas-phase energy.

$$\begin{aligned} \frac{D}{Dt} [\Psi \rho_{g_1} \pi r_s^2 L_m (C_{vg} T_{g_1}^* + \Delta H_{f,g}^\circ)] &= \\ &- (\Delta H_{f,g}^\circ + C_{pg} T_{g_1}^*) \rho_g v_{lr}^2 \pi r_s L_m \Psi + \dot{q}_{gas}'' \Psi B \pi r_s^2 \\ &+ \dot{m}_{g_{net_1}} (C_{p,R} T_b^* + \Delta H_{f,R}^\circ) - p \frac{D}{Dt} (\pi r_s^2 L_m \Psi) \\ &+ \dot{m}_{g_B} (C_{p,R} T_b^* + \Delta H_{f,R}^\circ) - \dot{q}_{gas-liq}'' A_{i_1} \end{aligned} \quad (10)$$

For the liquid phase, the balance of energy fluxes are given in Fig. 3b, and the energy equation can be

written as

$$\begin{aligned}
 & \frac{D}{Dt} [(1 - \Psi) \rho_L \pi r_s^2 L_m (C_{vg} T_{L1}^* + \Delta H_{f,L})] \\
 & = -(\Delta H_{f,L}^0 + C_{pg} T_{L1}^*) \rho_L v_{ir}^2 \pi r_s^2 L_m (1 - \Psi) \\
 & + \dot{q}_{liq}'' (1 - \Psi_B) \pi r_s^2 - \dot{m}_{g_{net}} (C_{pg,R} T_b^* + \Delta H_{f,R}^0) \\
 & + (-v_m) \rho_{pr} \pi r_s^2 (C_{pg} T_{melt}^* + \Delta H_{f,L}^0) - \dot{q}_{liq-solid}'' \pi r_s^2 \\
 & - \dot{m}_{g_B} (C_{pg,R} T_b^* + \Delta H_{f,R}^0) + \dot{q}_{gas-liq}'' A_{i_1} \quad (11)
 \end{aligned}$$

where

$$\Delta H_{f,g}^0 = Y_R \Delta H_{f,R}^0 + (1 - Y_R) \Delta H_{f,P}^0 \quad (12)$$

$$C_{vg} = Y_R C_{y,R} + (1 - Y_R) C_{v,P} \quad (13)$$

$$C_{pg} = Y_R C_{p,R} + (1 - Y_R) C_{p,P} \quad (14)$$

both \dot{q}_{liq}'' and $\dot{q}_{liq-solid}''$ are positive for downward heat fluxes.

Initial and Boundary Conditions. In order to solve the temperature distributions inside the spall particle and solid propellant, a set of initial and boundary conditions must be specified for equations (1) and (2). There are two sets of conditions: one corresponds to Time Period I ($t < t_{melt}$); the other corresponds to Time Period II ($t \geq t_{melt}$). The initial conditions for Time Period I are

$$T_s(0) = T_{si} \quad (15)$$

$$T_p(0) = T_{pi} \quad (16)$$

The initial conditions for Time Period II are the temperature profiles solved at the end of Time Period I.

The boundary conditions for spall particles in Time Period I can be specified readily; some of the boundary conditions are special cases of those for Time Period II. Therefore, the are omitted here. The boundary conditions for the spall particle of Case (a) in Fig. 1 during Time Period II are given as

$$\text{at } z = L_s : -\lambda_s \frac{\partial T_s}{\partial z} = h_{c1}(T_s - T_\infty) + \epsilon_s \sigma (T_s^4 - T_\infty^4) \quad (17)$$

$$\begin{aligned} \text{at } z = 0 : \lambda_s \frac{\partial T_s}{\partial z} = & - \frac{1}{\pi r_s^2} \dot{m}_{g_B} (C_{p1} T_b^* + \Delta H_{f,1}^\circ) \\ & + \Psi_B \dot{q}_{gas}'' + (1 - \Psi_B) \dot{q}_{liq}'' + \\ & \frac{1}{\pi r_s^2} \dot{m}_{g_B} (C_{p,R} T_b^* + \Delta H_{f,R}^\circ) \end{aligned} \quad (18)$$

$$\text{at } r = 0 : \frac{\partial T}{\partial r} = 0 \quad (19)$$

$$\text{at } r = r_s : \left. \begin{aligned} & - \frac{1}{\lambda_s} h_{eff2_1} (t, z) [T_s(t, r_s, z) - T_m(t)] \\ & - \frac{\dot{q}_{m1}}{\lambda_s} \quad (\text{for } 0 < z \leq h_1) \end{aligned} \right\} \quad (20a)$$

$$\left. \begin{aligned} & - \frac{1}{\lambda_s} h_{eff2_g} (t, z) [T_s(t, r_s, z) - T_g] \\ & \quad (\text{for } h_1 < z \leq L_s) \end{aligned} \right\} \quad (20b)$$

The boundary conditions for LOVA propellant in Time period II for Case (a) can be written as follows

$$\text{at } z = -\infty : T_p = T_{pi} \quad (21)$$

$$\text{at } z = -L_m : T_p = T_{melt} \quad (22)$$

$$\text{at } r = \infty : T_p = T_{pi} \quad (23)$$

$$\begin{aligned} \text{at } r = r_m : \quad & -\lambda_{pr} \frac{\partial T_p}{\partial r} = \dot{q}_{m2}'' \quad (\text{if } v_{mr} = 0) \\ z \leq h_1 & \quad T_p = T_{melt} \quad (\text{if } v_{mr} > 0) \end{aligned} \quad (24)$$

$$\text{at } r = r_m: -\lambda_{pr} \frac{\partial T_p}{\partial r} = \dot{q}_{rad,p}^n + h_{c2}(T_g - T_{ps}) \quad (\text{if } v_{mr} = 0) \\ h_l < z \quad (25)$$

$$T_p = T_{melt} \quad (\text{if } v_{mr} > 0) \\ \text{at } z = h_p: -\lambda_{pr} \frac{\partial T_p}{\partial z} = h_{c3}(T_{ps} - T_\infty) - \dot{q}_{rad,p}^n \\ r > r_m \quad (26)$$

The boundary conditions for the spall particle and LOVA propellant in Time Period II for Cases (b), (c), and (d) can be written in a similar manner and are omitted here to save space.

Simplifications of the Mathematic Model.

Although the above set of governing equations can be solved with their boundary and initial conditions, together with a set of adequate heat transfer correlations, the calculation of the above PDE model is extremely time-consuming. In order to bypass this difficulty in solving many coupled partial differential equations (PDEs) and intricate boundary conditions, the theoretical model has been recast into a set of ordinary differential equations (ODEs) using the Goodman's (1964) integral method.

In general, the instantaneous temperature distribution inside the spall particle with a cylindrical shape is a function of radial and axial positions. During the interval of contact with the LOVA propellant, the heat fluxes across the boundaries of the spall particle are high enough to generate non-negligible temperature gradients inside the particle. Therefore, lumped-parameter analysis cannot be used for this situation. To obtain approximate solution of the HFCI model based upon PDE formulation, the temperature profile is assumed to obey the following polynomial form (see Fig. 4).

$$\frac{T_s(t, r, z)}{T_u(t)} = [1 + C_1(t)r^2 + C_2(t)r^3] \cdot \\ [1 + C_3(t)(z - z_m) + C_4(t)(z - z_m)^2 \\ + C_5(t)(z - z_m)^3 + C_6(t)(z - z_m)^4] \quad (27)$$

where $T_u(t)$ represents either the temperature of the uniform-temperature zone in the spall or the maximum instantaneous temperature when the uniform-temperature zone shrinks to zero. The height z_m represents either that of the midpoint of the uniform-temperature zone or that of the maximum temperature point. z_m can be calculated from the following equations

$$z_m = \begin{cases} \frac{1}{2}[\delta_{th_B} + (L_s - \delta_{th_T})] & \text{for finite uniform-} \\ & \text{temperature zone} \end{cases} \quad (28)a$$

$$\delta_{th_B} \quad \text{after uniform-temperature} \quad (28)b$$

$$\text{zone disappears}$$

$C_1(t)$ through $C_6(t)$ are time-dependent coefficients to be determined by various boundary and smooth conditions discussed later.

Following Goodman's (1964) integral method, by integrating equation (1) twice with respect to z and r and applying the polynomial form of equation (27), the PDE for the spall particle is reduced to

$$\frac{dP(t)}{dt} = r_s^2 \alpha_s T_u(t) S(t) \quad (29)$$

where the parameters $P(t)$ and $S(t)$ are defined as

$$P(t) = \frac{1}{\pi C_s \rho_s} [\theta_B(t) + \theta_T(t) + \theta_L(t) + \theta_u(t)] \quad (30)$$

$$S(t) = \frac{1}{r_s^2} [r_s^2 + \frac{C_1}{2} [r_s^4 - (r_s - \delta_{th_L})^4] + \frac{2}{5} C_2 \cdot \\ [r_s^5 - (r_s - \delta_{th_L})^5] \cdot [2C_4 L_s + 3C_5 [(L_s - z_m)^2 - z_m^2] \\ + 4C_6 [(L_s - z_m)^3 + z_m^3]] + 2(2C_1 + 3C_2 r_s) \cdot \\ [L_s + \frac{C_3}{2} [(L_s - z_m)^2 - z_m^2] + \frac{C_4}{3} [(L_s - z_m)^3 - z_m^3] \\ + \frac{C_5}{4} [(L_s - z_m)^4 - z_m^4] + \frac{C_6}{5} [(L_s - z_m)^5 - z_m^5]] \quad (31)$$

In equation (30), θ_B , θ_T , and θ_L represent the thermal energy content in the bottom, top, and lateral thermal penetrated zone of the spall particle; their mathematical definitions are as follows:

$$\theta_B(t) = \int_0^{\delta_{th_B}(t)} \int_0^{r_s} C_s \rho_s T_s 2\pi r dr dz \quad (32)$$

$$\theta_T(t) = \int_{L_s - \delta_{th_T}(t)}^{L_s} \int_0^{r_s} C_s \rho_s T_s 2\pi r dr dz \quad (33)$$

$$\theta_L(t) = \int_{\delta_{th_B}(t)}^{L_s - \delta_{th_T}(t)} \int_{r_s - \delta_{th_L}(t)}^{r_s} C_s \rho_s T_s 2\pi r dr dz \quad (34)$$

The thermal energy storage in the uniform temperature zone, $\theta_u(t)$, can be expressed as

$$\theta_u(t) = \int_{\delta_{th_B}(t)}^{L_s - \delta_{th_T}(t)} \int_{r_s - \delta_{th_L}(t)}^{r_s} C_s \rho_s T_s 2\pi r dr dz \quad (35)$$

The above four θ s are expressed in terms of thermal wave penetration depths and constants C_1 through C_6 . These six constants are solved from a set of coupled linear algebraic equations obtained from the boundary and smooth conditions. Their explicit forms are given by Kuo et al. (1985).

To evaluate the thicknesses of the thermal waves near the top and bottom of the spall particle, the following equations, deduced from the expression obtained by Goodman (1964), can be used.

$$\delta_{th_T}(t) = \sqrt{6\alpha} \left\{ \frac{1}{h_{eff,1C}(t)(T_{s,TC} - T_g)} \right. \\ \left. \int_0^t h_{eff,1C}(t) (T_{s,TC} - T_g) dt \right\}^{1/2} \quad (36a)$$

$$\delta_{th_B}(t) = \sqrt{6\alpha} \left[\frac{1}{\dot{q}_{spall_1}''(t)} \int_0^t \dot{q}_{spall_1}(t) dt \right]^{1/2} \quad (36b)$$

where the subscript TC stands for top center location of the spall particle. The thickness of the thermal wave penetration depth in the lateral direction can also be given in a similar form.

Using a third-degree polynomial in z^* to represent the temperature profile in the solid propellant and integrate equation (2) with respect to z^* , the time variation of the thermal wave penetration depth (the thickness of the heated zone), δ_{pr} , can be determined from

$$\frac{d\delta_{pr}^2(t)}{dt} = 6 \alpha_{pr} + 2v_m(t)\delta_{pr}(t) \quad (37)$$

The initial condition for δ_{pr} is

$$\delta_{pr}(0) = 0 \quad (38)$$

After $\delta_{pr}(t)$ is solved, $\dot{q}_{pr}''(t)$ can be calculated from

$$\dot{q}_{pr}''(t) = 3\lambda_p \frac{(T_{melt} - T_{pi})}{\delta_{pr}(t)} \quad (39)$$

Heat Transfer Correlations Employed in the Theoretical Model. To complete the model formulation, the following heat-transfer correlations are presented as a part of physical input to the model.

a. Heat Transfer at the Base of Spall Particle. The rates of heat transfer from the spall particle base to the liquid and gas bubbles in the foam layer (\dot{q}_{liq}'' and \dot{q}_{gas}'') can be evaluated from

$$\dot{q}_{liq}'' = h_{base} (\bar{T}_{SB} - T_{l_1}) \quad (40)$$

$$\dot{q}_{gas}'' = h_{base} (\bar{T}_{SB} - T_{g_1}) \quad (41)$$

When the average temperature at the base of the spall particle (\bar{T}_{SB}) is higher than the saturation temperature of the liquid melt, the boiling heat transfer correlation should be used. According to the empirical correlations of Jakob and Hawkins (1957) and Holman (1977), h_{base} is related to the temperature difference between T_{SB} and saturation temperature \bar{T}_{sat} by the following equation.

$$h_{base} = \begin{cases} 1042 (\bar{T}_{SB} - T_{sat})^{1/3} & \text{if } \dot{q}_{spall}'' < 15770. \\ 5.56 (\bar{T}_{SB} - T_{sat})^3 & \text{if } 15770 < \dot{q}_{spall}'' < 2.365 \times 10^5 \end{cases} \quad (42)$$

This equation was developed from boiling heat-transfer data of water at one atmospheric pressure on a horizontal plate. Strictly speaking, this correlation is not completely suitable for the downward heating from the spall particle base to the foam layer, but in the absence of better correlations, it is temporarily adopted and used with caution. According to Cheung (1985), the boiling heat transfer for the downward-heating case may follow the same temperature-difference dependence, but the constants could be approximately two to three times higher than the upward heating. In view of the confined space available between the base of the spall particle and the solid propellant, the gas bubble may be trapped momentarily in this foam layer region. If this happens, the material in the foam layer could accumulate thermal energy and reduce the rate of boiling heat transfer. Because the downward-heating effect may compensate for the confined-space effect, equation (42) is used at present for the simulation of melting and evaporation of ice to be discussed in a later section.

After the base temperature of the spall particle has dropped below the boiling temperature, gas bubbles could still be generated from the spall surface (due to transient heating of the foam layer) until \dot{q}_{spall}'' decreases to the level of \dot{q}_{min}'' . \dot{q}_{min}'' can be calculated from the following equation based upon the studies of Chang (1959), Zuber (1959), and Lienhard and Dhir (1980).

$$\dot{q}_{min}'' = 0.177 \rho_g h_{fg} \left[\frac{\sigma_s g (\rho_l - \rho_g)}{(\rho_l - \rho_g)^2} \right]^{1/4} \quad (43)$$

where g is the gravitational acceleration.
The average velocity of bubbles leaving the heated surface area is

$$v_b = 0.59 \left[g \sigma_s (\rho_l - \rho_g) / \rho_l^2 \right]^{1/4} \quad (44)$$

which is based upon the relationship reported by Rohsenow and Choi (1969). The average bubble diameter

at detachment from the heating surface, based upon the empirical formula of Fritz (1935), is

$$D_b = C_d \beta \sqrt{\frac{2\sigma_s}{g(\rho_l - \rho_g)}} \quad (45)$$

where β is approximately 40° and $C_d = 0.0148$ for water in the ice melting and evaporation simulation.

The void fraction at the base of the spall particle, Ψ_B , can be evaluated from the following approximation.

$$\Psi_B = \frac{1}{\pi} \tan^{-1} \left[a \left(\frac{\dot{q}_{\text{spall}}''}{\dot{q}_{\text{min}}''} \right) - b \right] + \frac{1}{2} \quad (46)$$

where a is a stretching constant in the order of one, and b is a specific heat-flux ratio at which Ψ_B versus $\dot{q}_{\text{spall}}''/\dot{q}_{\text{min}}''$ has a point of inflection. This equation is formulated based upon the fact that it satisfies the limiting case of film boiling, which requires that $\Psi_B \rightarrow 1$ when $\dot{q}_{\text{spall}}'' \gg \dot{q}_{\text{min}}''$. It also satisfies the condition that when $\dot{q}_{\text{spall}}'' = \dot{q}_{\text{min}}''$, Ψ_B should approach zero.

When T_{SB} is lower than the saturation temperature of the liquid melt, the heat-transfer coefficient between the fluid in the foam layer and the bottom surface of the spall particle can be evaluated from the following Kercher's empirical correlation taken from the General Electric Heat Transfer Data Book (1979).

$$h_{\text{base}} = \frac{C_1 \phi_2 \lambda_{\text{mixture}}}{D_b} \left(\frac{\rho_g v_b D_b}{\mu_g} \right)^m \left(\frac{L_m}{D_b} \right)^{0.091} (Pr_g)^{1/3} \quad (47)$$

where λ_{mixture} is calculated from

$$\lambda_{\text{mixture}} = \Psi_B \lambda_{\text{vapor}} + (1 - \Psi_B) \lambda_{\text{liq}} \quad (48)$$

ϕ_1 and ϕ_2 of equation (47) are correction factors which depend upon the ratio of bubble separation distance (X_n), bubble diameter, and the Reynolds number ($= \rho_g v_b D_b / \mu_g$). The above equation was initially developed for gases to flow through an array of

circular holes of a porous plate, located at the top of a horizontal gap. Numerous jets impinge on a bottom horizontal plate located a small distance from the top porous plate. The bubbles generated at the base of the spall can be regarded as gases injected downward through a horizontal porous plate. Even though the locations of bubbles vary from time to time, as long as the bubble sizes and separation distances are properly calculated, the flow agitation and heat transfer processes are quite similar to those of a porous plate. The average separation distance between bubbles is calculated from the bubble size and the void fraction in the foam layer by the following equation.

$$x_n = 0.5 \sqrt{\frac{\pi}{\Psi_B} D_b} \quad (49)$$

The heat-transfer coefficient given in equation (47) is used to determine the energy fluxes, q''_{gas} and q''_{liq} , until T_{SB} decreases to T_{melt} .

b. Heat Transfer at the Interface Between Liquid Melt and Solid Material. The heat-transfer process in the foam layer at the interface with solid material is governed by the condensation of bubbles at the interface. Levenspiel's correlation of steam-bubble condensation (Soo, 1967) has been adopted to calculate the instantaneous heat-transfer coefficient and the heat flux $q''_{\text{liq-solid}}$. The heat transfer coefficient can be written as

$$h_c(t) = 3.54 D_{b_{\text{eff}}} (t) \rho_g(t) h_{fg} \quad (50)$$

To adequately calculate the values of $h_c(t)$, the effective bubble diameter is used in the above equation to replace the instantaneous diameter of a single bubble. During the condensation process, the rate of decrease of bubble diameter can be described by the following equation (Soo, 1967).

$$\frac{d \ln D_b(t)}{dt} = 7.08 [T_{pr}(t,0) - T_{g_1}(t)] \quad (51)$$

Both the propellant or ice surface temperature and the bulk temperature of the gas bubble are functions of time. However, experimental evidence indicates that the bubble lifetime is much shorter than the foam-layer action time; hence, T_{g_1} can be treated as a constant in estimating single bubble lifetime. Setting the propellant surface temperature equal to T_{melt} , equation (51) can be integrated with respect to time to give

$$D_b(t) = D_b(0) \exp[-7.08 (T_{g_1} - T_{melt}) t] \quad (52)$$

Using the same functional form, the effective bubble diameter can be expressed as

$$D_{b_{\text{eff}}}(t) = D_b \exp[-kt] \quad (53)$$

where D_b (the average diameter at detachment) is calculated from equation (45) and k^{-1} represents the characteristic decay time. The physical meaning of the effective bubble diameter is associated with the averaged void fraction of the surface area due to bubble impingement on the propellant surface. As the spall particle sinks into the ice block, the particle is cooled by transferring the heat to its adjacent material. The boiling process becomes less intense and generates fewer gas bubbles to impinge on the ice block. Therefore, the effective diameter decreases with respect to time. The k value used in equation (53) is in the order of 0.2 sec^{-1} . To account for the above effect caused by the reduction of bubble number density in terms of effective bubble diameter, the decay time (k^{-1}) used in the computation is considerably longer than the bubble lifetime.

c. Heat Transfer at the Top and Lateral Surfaces of the Spall Particle. The top surface of a spall particle can be considered as a horizontal plate where the heat-transfer mechanism is due mainly to natural convection (McAdams, 1954; and Goldstein et al., 1973). The Nusselt number is expressed as a function of the Rayleigh number in the commonly used McAdams' (1954) correlation.

The lateral surface of the spall particle in contact with the foam layer experiences natural convection or conduction since the velocity of the melt layer is quite small. On the other hand, the lateral surface of the spall particle which is exposed to the air experiences forced convection due to the flow of pyrolyzing gaseous species above the melt

layer. In order to consider these two different mechanisms, it is necessary to determine the different heat-transfer coefficients caused by forced and free convection.

For laminar flows, the conventional correlation for parallel external flow, along the axis of a cylinder, is used to relate the local Nusselt number to the local Reynolds and Prandtl numbers (Holman, 1972). For turbulent flows, Schlichting's (1968) local friction coefficient is used to relate Reynolds numbers with the local Nusselt number.

Application of the HFCI Model for Simulating the Melting and Evaporation of Ice upon Direct Contact with a Hot Element

In order to verify the theoretical model developed for predicting HFCI phenomena, a set of input parameters and functions is required. At present, although some measurements are being conducted by Miller (1986), many critical parameters for LOVA propellants are not fully characterized. In view of this situation, experiments must be conducted in a simpler system to simulate HFCI phenomena.

One obvious way to simulate the conductive heating, melting, and evaporating processes of HFCI tests is to heat an ice block with a hot metal rod. In such an experiment, uncertainties in chemical kinetics in the melt layer are avoided, and data from experiments can be used to validate the theoretical model under the limiting condition without involving chemical reactions. The reason ice was selected for melting and evaporation simulation is due to the well-known boiling heat transfer characteristics of water, as well as its thermal properties. The ice cube is also readily available for experiments.

The regression velocity of the ice surface, v_m , is computed from the heat-flux balance at the interface between the foam layer and ice by the following equation.

$$v_m = \frac{\dot{q}_{\text{liq-solid}}^* - \dot{q}_{\text{pr}}^*}{\rho_{\text{pr}} [C_{\text{pr}} - C_{\text{pl}}] T_{\text{melt}}^* + \Delta H_{f,\text{pr}}^* - \Delta H_{f,l}^*]} \quad (54)$$

Major and minor unknowns, together with the numbers of equations for their determination, are listed in Tables 1 and 2.

Table 1. Major Unknowns and Equations

Region	Unknown	Equation
Spall	T_s	(27)
Particle	P	(29)
	T_u	(30), (31-35)
Foam	γ_R	-0
Layer	T_{g1}	(10)
	T_{l1}	(11)
	v_m	(54)
	Ψ	(4)
Ice	δ_{pr}	(37)

Table 2. Minor Unknowns and Equations

Region	Unknown	Equation	Unknown	Equation
Spall Particle	θ_B	(32)	θ_L	(34)
	θ_T	(33)	θ_u	(35)
	δ_{thT}	(36) _a	δ_{thB}	(36) _b
	δ_{thL}	(36) _a & (36) _b	z_m	(28) _a or (28) _b
Foam Layer	$\Delta H_f,g^\circ$	(12)	D_b	(45)
	C_{vg}	(13)	C_{pg}	(14)
	h_{base}	(42) or (47)	\dot{q}_{liq}''	(40)
	h_c	(50)	\dot{q}_{gas}''	(41)
			Ψ_B	(46)
Ice	\dot{q}_{pr}''	(39)	----	----

TEST SETUP AND RESULTS FOR ICE MELTING AND EVAPORATION EXPERIMENTS

An ice-melting and evaporating experiment has been devised and conducted. To be compatible with the theoretical model, a steel cylindrical rod with a diameter of 1.27 cm and a length of 2.54 cm is connected at one end to a 10.16 cm-long guiding steel rod with a diameter of 0.3175 cm. Four Copper-Constantan thermocouples with bead sizes of 0.025 cm and wire diameters of 0.0075 cm were soldered to different locations of the heating element (shown in

Fig. 5). In these tests, the heating element was heated inside an oven with preselected temperature. The heating element was placed on top of an ice cube, and the temperature-time variations at different locations were recorded. A typical set of recorded temperature-time traces is shown in Fig. 5.

In addition to temperature-time measurements, a video movie camera was used to record the ice melting and evaporating phenomena. The instantaneous position of the heating element was recorded on the video camera. The displacement and velocity of the heating element were determined by reading the instantaneous top surface location of the heating element against a stationary scale and the digital time counter on the video screen. Time variations of the measured velocity of the heating element are compared with theoretical results in a later section.

In order to observe the flow pattern of the gas and steam surrounding the heating element, a Schlieren optical system (Settles, 1970; and Kuo et al., 1985) was used. A typical color Schlieren photograph obtained from an ice-melting and evaporating experiment is shown in Fig. 6. Several interesting observations are made from the video and temperature records of these experiments:

- 1) Although all four temperature-time traces in Fig. 5 showed similar variations, there are some differences among these traces. The temperatures on the main body of the heating element decay at a slower rate than those on the guiding rod. This is due to the fact that the surface area per unit volume is much larger on the guiding rod than that of the main body.
- 2) Based upon the slope changes of the temperature decay, the overall process can be divided into the three time zones shown in Fig. 5. In the initial time zone, the temperature of the heating element decays slowly with time since the element was taken from the oven and cooled by natural convection in air and radiation to the surrounding. A small amount of energy is lost from the guiding rod to a room-temperature clamp by conduction. In the second time zone, a significant amount of steam was generated at the contact zone of the heating element and the ice. The flow around the cylindrical rod was highly turbulent. Associated with steam generation, the temperatures at all thermocouple locations decrease drastically in 1.2 seconds, as shown in Fig. 5. In the last time zone, steam generation is gradually replaced by ice melting and slow sinking of the heating element into the ice block. Eventually, the heating element stopped at a terminal position inside the ice block.

- 3) The downward velocity of the heating element was highest upon initial contact with the ice block, and then decayed monotonically to zero velocity.
- 4) From the color Schlieren photographs, one can see clearly that the steam-jet velocity is mostly in the radial direction at the initial time interval. The steam jet then changed from radial outward direction to vertical upward direction. Associated with steam-jet action, the flow field surrounding the cylinder is highly turbulent. Following the decay of steam generation, the flow became laminar at the later stage.

COMPARISON OF NUMERICAL RESULTS WITH TEST DATA OF ICE MELTING AND EVAPORATION

To partially verify the HFCI model, numerical solutions were compared with experimental data obtained from an ice-melting and evaporating experiment. Input data for this numerical simulation is given in Table 3. Figure 7 presents a comparison of the calculated sinking velocity of the spall particle with the measured data. It is quite obvious that agreement between calculated results and measured data is reasonably close. The trend of sharp decline followed by a much slower rate of sinking is exhibited in both theoretical and experimental results. Figure 8 shows the comparison of calculated spall particle trajectory with experimental data. The agreement is not extremely close; however, the calculated trend of traveling distance variation with time and the magnitude of h_p are not far from the measured data.

Table 3. Input Data Used in the Ice-Melting and Evaporation Simulation

Region	Parameter	Value	Parameter	Value
Spall Particle	r_s	0.635×10^{-2}	λ_s	6.39×10^{-1}
	L_s	2.54×10^{-2}	C_s	4.34×10^2
	ρ_s	7.83×10^3	T_{si}	4.90×10^2
	ρ_l	9.87×10^2	λ_l	4.52×10^{-2}
Foam Layer	C_{pl}	4.18×10^3	$\Delta H_{f,l}^\circ$	-1.59×10^7
	C_{pg}	1.87×10^3	$\Delta H_{f,g}^\circ$	-1.34×10^7
	C_{vg}	1.41×10^3		
Ice	C_{pr}	2.04×10^3	λ_{pr}	2.21
	ρ_{pr}	9.13×10^2	$\Delta H_{f,pr}^\circ$	-1.55×10^7

From the comparison of the calculated and measured temperature-time traces at the thermocouple TC2 location shown in Fig. 9, it is evident that the two traces are very close. In the same figure, calculated traces for the average temperature at the base of the spall particle (T_{SB}) and the maximum spall particle temperature (T_u) are plotted. It is interesting to note that the temperature difference between T_u and T_{SB} is much larger than that between T_u and TC2. This implies that a significant temperature gradient exists near the base of the spall particle because of the high heat flux leaving the spall particle base region.

The temperature gradient in the radial direction in the middle of the cylindrical spall particle is nearly negligible due to relatively low radial heat fluxes and high thermal conductivity of the material.

Figure 10 shows the calculated radial temperature profiles at the top surface, middle section, and bottom surface of the spall particle for various times. Most of the profiles are quite flat, but there is some gradient in the radial direction, especially during the early part of the event. Calculated temperature profiles in the ice are shown in Fig. 11. It is clear that the thermal wave penetration depth increases monotonically with respect to time, while the surface temperature is maintained at a fixed value.

The calculated time variations of \dot{q}_{spall} and \dot{q}_{pr} are shown in Fig. 12. It is useful to point out that \dot{q}_{spall} is significantly higher than \dot{q}_{pr} for a long period of time. This indicates that a substantial amount of energy is carried away by evaporation of liquid melt in the foam layer. The sharp declines of \dot{q}_{spall} and \dot{q}_{pr} in the initial time period dictate the rapid decrease of sinking velocity with respect to time.

SUMMARY AND CONCLUSIONS

- (1) A comprehensive theoretical model for simulating hot fragment conductive ignition processes of LOVA propellants has been formulated. This model simulates: heat-transfer processes between the spall particle and propellant; formation of the liquid-melt or foam layer; propellant pyrolysis processes; displacement of the hot spall particle; and propellant ignition or quenching of the spall particle.
- (2) The partial differential equations governing the transient heat-transfer processes in the spall particle and LOVA propellant have been successfully converted to a set of ordinary differential equations. This leads to a major reduction in computational time.
- (3) The HFCI model has been applied to the ice melting and evaporation processes under the direct contact with a hot element. Experimental tests were conducted with temperature measurements and flow visualization using a color Schlieren system.

- (4) Good agreement between calculated results and test data of ice-melting and evaporation experiments shows that the HFCI model is capable of predicting the major heat- and mass-transfer characteristics in the melting and evaporation of a solid with known thermal properties and boiling characteristics of its liquid melt.
- (5) During the initial contact between the spall particle and ice block, a strong steam jet in the radial direction is generated. As time progresses, the steam jet changes from the radial to the vertical direction as its strength decays. A substantial amount of energy is carried away by the steam jet generated from evaporation of liquid melt in the foam layer.
- (6) The input parameters and types of correlations required for studying the HFCI processes of a given solid propellant can be identified from the theoretical model presented in this paper. The full validation of the HFCI model cannot be performed until a set of input parameters and correlations become available.

ACKNOWLEDGMENT

This work was performed under Contract DAAK11-83-C-0015, sponsored by the Applied Ballistics Branch of the Ballistic Research Laboratories under the support and encouragement of Dr. Joseph J. Rocchio and Mr. Norman Gerri. The authors would like to thank Dr. M. Kumar for his participation in the early stage of this research.

REFERENCES

Anderson, W. H., Brown, R. E., and Louie, N. A., 1972, Proceedings of the 9th JANNAF Combustion Meeting, CPIA Publication 231, pp. 67-82.

Caveny, L. H., Summerfield, M., Strittmater, R. C., and Barrows, A. W., 1973, "Solid Propellant Flammability Including Ignitability and Combustion Limits," CPIA Publication 243, Vol. III, pp. 133-155.

Chang, Y. P., 1959, "A Theoretical Analysis of Heat Transfer in Natural Convection and in Boiling," Trans ASME, Vol. 79, p. 1501.

Cheung, F. B., 1985, Private Communication, The Pennsylvania State University, University Park, PA.

Fritz, H. K., 1935, Physik, pp. 36, 379.

General Electric Heat Transfer Data Book, 1979.

Gol'dshleger, U. I., Barzykin, V. V., Ivleva, T. P., 1973, Combustion, Explosion and Shock Waves, Vol. 9, No. 5, pp. 642-647.

Gol'dshleger, U. I., Pribytkova, K. V., and Barzykin, V. V., 1973, Combustion, Explosion and Shock Waves, Vol. 9, No. 1, pp. 99-102.

Goldstein, R. J., Sparrow, E. M., and Jones, D. C., 1973, "Natural Convection Mass Transfer Adjacent to Horizontal Plates," International Journal of Heat and Mass Transfer, Vol. 16, p. 1025.

Goodman, T. R., 1964, "Application of Integral Methods to Transient Nonlinear Heat Transfer," Advances in Heat Transfer, ed. by Irvine, T. F. and Hartnett, J. P., Jr., Vol. 1.

Grossman, E. D. and Rele, P. J., 1974, "Ignition of Cellulose Nitrate by High Velocity Particles," Combustion Science and Technology, Vol. 9, pp. 55-60.

Holman, J. P., 1972, Heat Transfer, McGraw-Hill, New York, Third Edition, Chapter 5.

Holman, J. P., 1977, Heat Transfer, McGraw-Hill, New York, Fourth Edition, Chapter 9.

Jakob, M. and Hawkins, G., 1957, Elements of Heat Transfer, John Wiley and Sons, Inc., New York, Third Edition.

Kirshenbaum, M. S., Avrami, L., and Strauss, B., 1983, "Sensitivity Characterization of Low Vulnerability (LOVA) Propellants," U.S. Army ARRADCOM Technical Report, ARLCD-TR-83005.

Kuo, K. K., Hsieh, W. H., and Hsieh, K. C., 1985, Eighth Quarterly Progress Report to Army Ballistic Research Laboratory, Contract No. DAAK11-83-C-0015.

Kuo, K. K., Hsieh, W. H., Hsieh, K. C., and Kumar, M., 1985, "A Comprehensive Model for Simulating Hot Fragment Conductive Ignition of Low Vulnerability Ammunition Propellant," Scientific Report, Contract No. DAAK-11-83-C-0015.

Law, H. C. and Rocchio, J. J., 1981, Proceedings of the 18th JANNAF Combustion Meeting, CPIA Publication No. 347, Vol. 2, pp. 321-334.

Lienhard, J. H. and Dhir, V. K., 1980, "On the Prediction of the Minimum Pool Boiling Heat Flux," ASME Journal of Heat Transfer, Vol. 102.

Linan, A. and Kindelan, M., 1981, Combustion in Reactive Systems, ed. by J. Ray Bowen et al., Progress in Astronautics and Aeronautics, Vol. 76, pp. 412-426.

McAdams, W. H., 1954, Heat Transmission, McGraw-Hill, New York, Third Edition, Chapter 7.

Miller, M. S., 1986, Private Communication, Ballistic Research Laboratory, Aberdeen Proving Ground, MD.

Rohsenow, W. M. and Choi, H. Y., 1969, Heat Mass and Momentum Transfer, Prentice-Hall, Inc., Chapter 9.

Schlichting, H., Boundary Layer Theory, 1968, McGraw-Hill, New York, Sixth Edition, Chapter 5.

Settles, G. S., 1970, "A Direction-Indicating Color Schlieren System," AIAA Journal, Vol. 8, No. 12.

Soo, S. L., 1967, Fluid Dynamics of Multiphase Systems, Blaisdell Publishing Company, Waltham, MA, p. 113.

Tyler, B. J. and Jones, D. R., 1981, Combustion and Flame, Vol. 42, pp. 147-156.

Vityunov, V. N. and Kolchin, A. K., Combustion, Explosion and Shock Waves, 1966, Vol. 2, No. 3, pp. 61-65.

Wise, S. and Rocchio, J. J., 1981, Proceedings of the 18th JANNAF Combustion Meeting, CPIA Publication No. 347, Vol. 2, pp. 305-320.

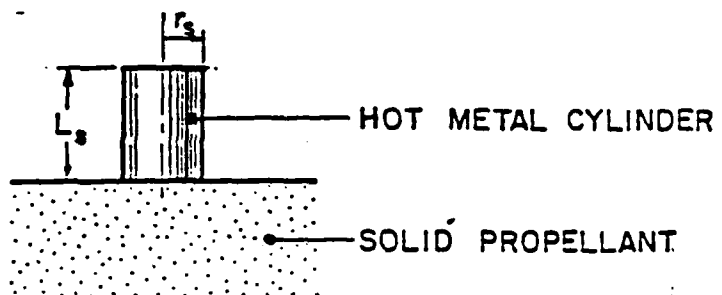
Wise, S., Rocchio, J. J., and Reeves, H. J., 1980, Proceedings of the 17th JANNAF Combustion Meeting, CPIA Publication 329, Vol. 3, pp. 457-475.

Zuber, N., 1959, "Hydrodynamic Aspects of Boiling Heat Transfer," Physics and Mathematics, AEC Report No. AECU-4439.

VARIOUS CASES CONSIDERED

32

TIME PERIOD I (BEFORE THE FORMATION OF A MELT LAYER)



TIME PERIOD II (AFTER THE FORMATION OF A MELT LAYER)

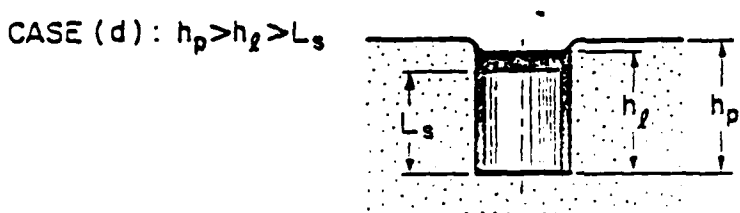
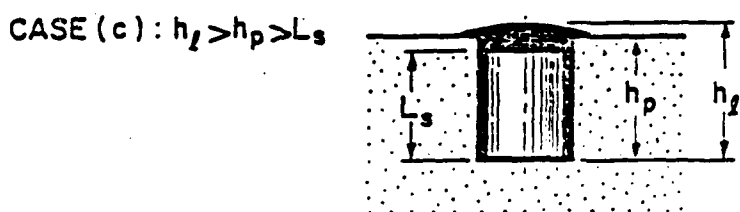
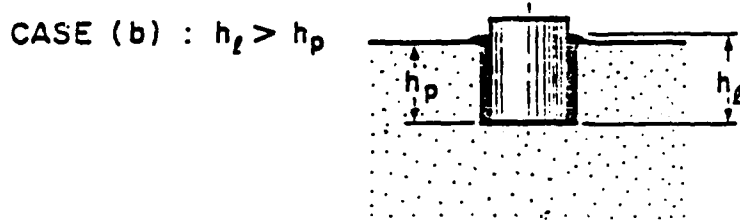
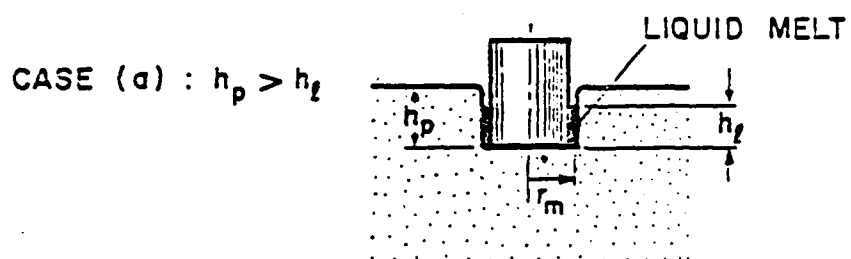


Fig. 1 Physical Event of Hot Fragment Conductive Ignition (HFCI) Processes Represented by Various Cases in Two Different Time Periods

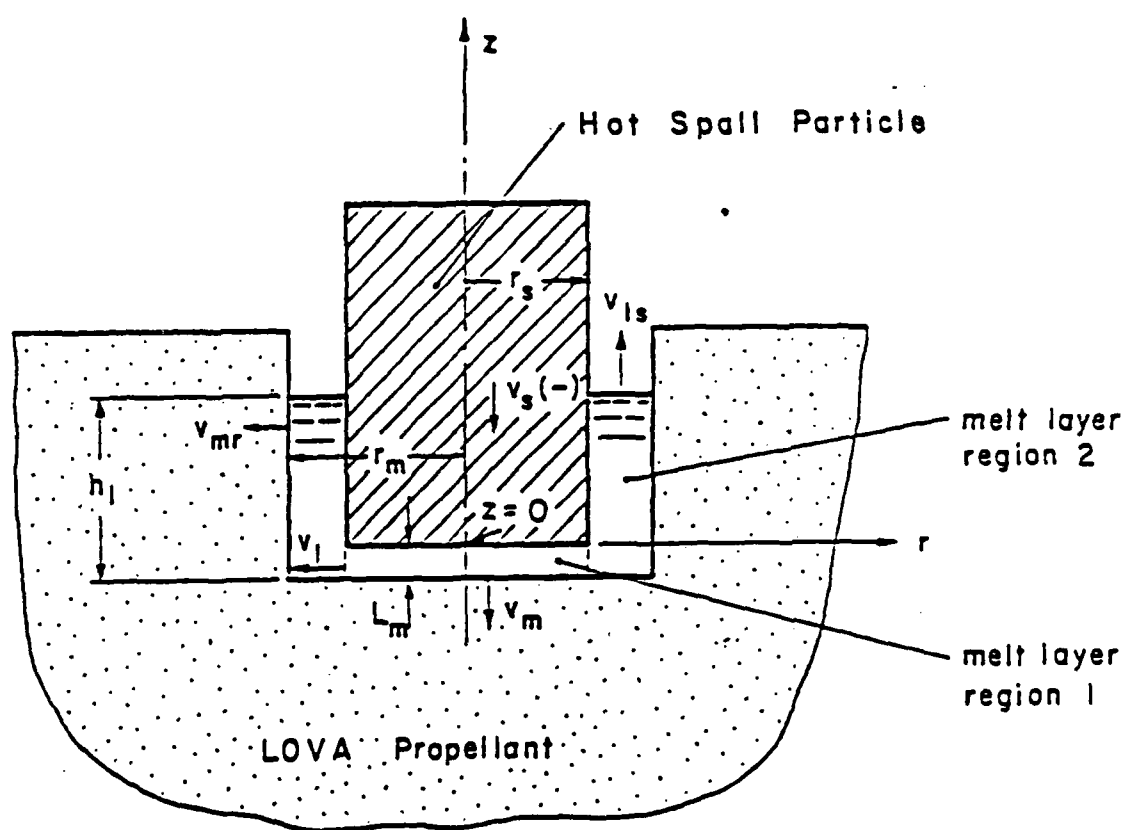


Fig. 2 Schematic Diagram of the Model

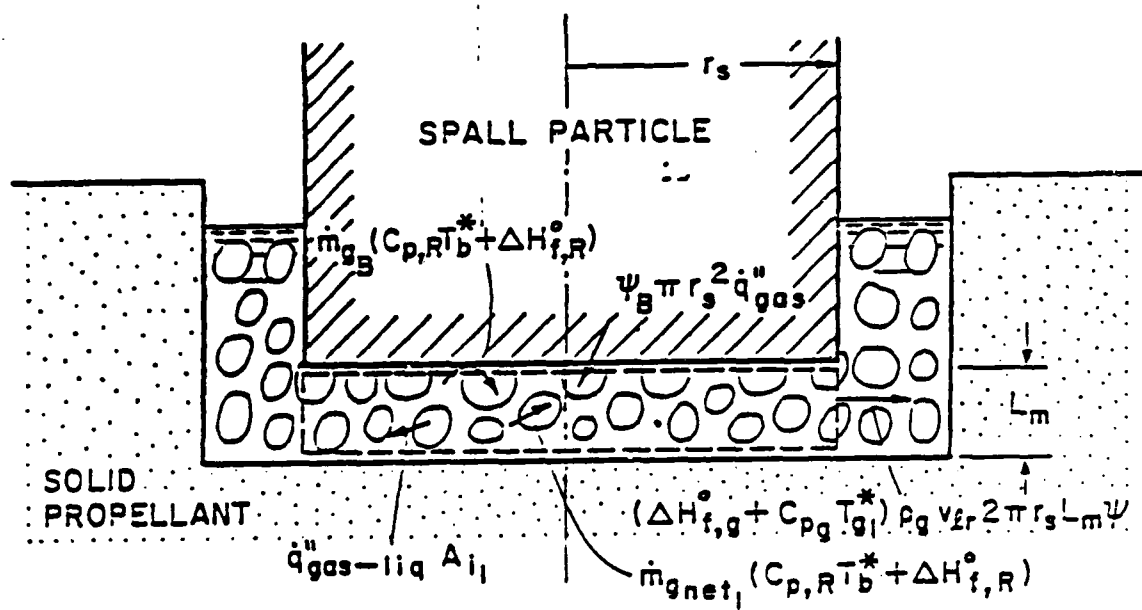


Fig. 3a Energy Fluxes Associated with the Gas Phase in Region 1 (The Thickness of Foam Layer is Highly Exaggerated)

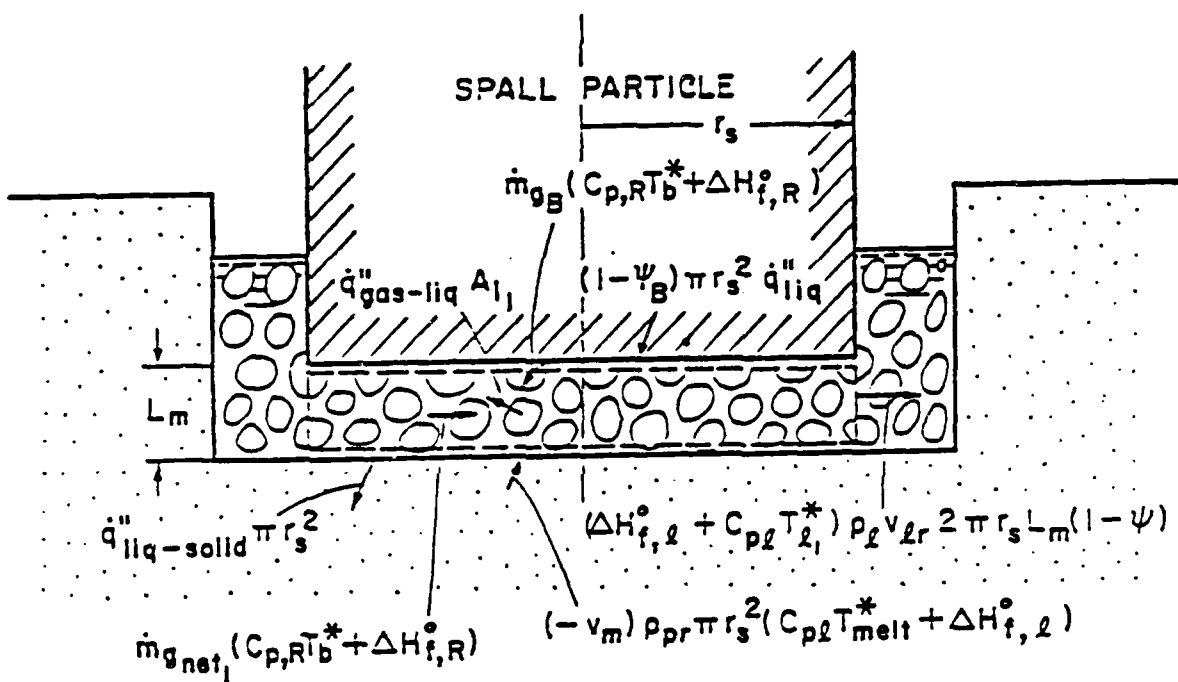


Fig. 3b Energy Fluxes Associated with the Liquid Phase in Region 1 (Thickness of Foam Layer is Highly Exaggerated)

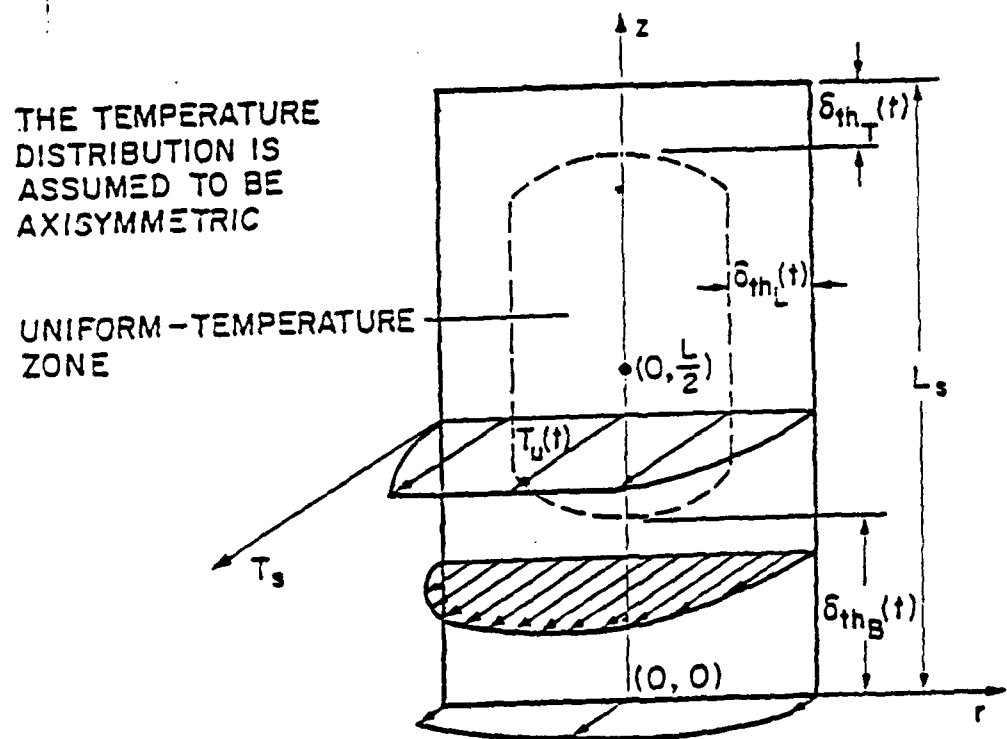


Fig. 4 Temperature Distributions in a Cylindrical Shaped Spall Particle

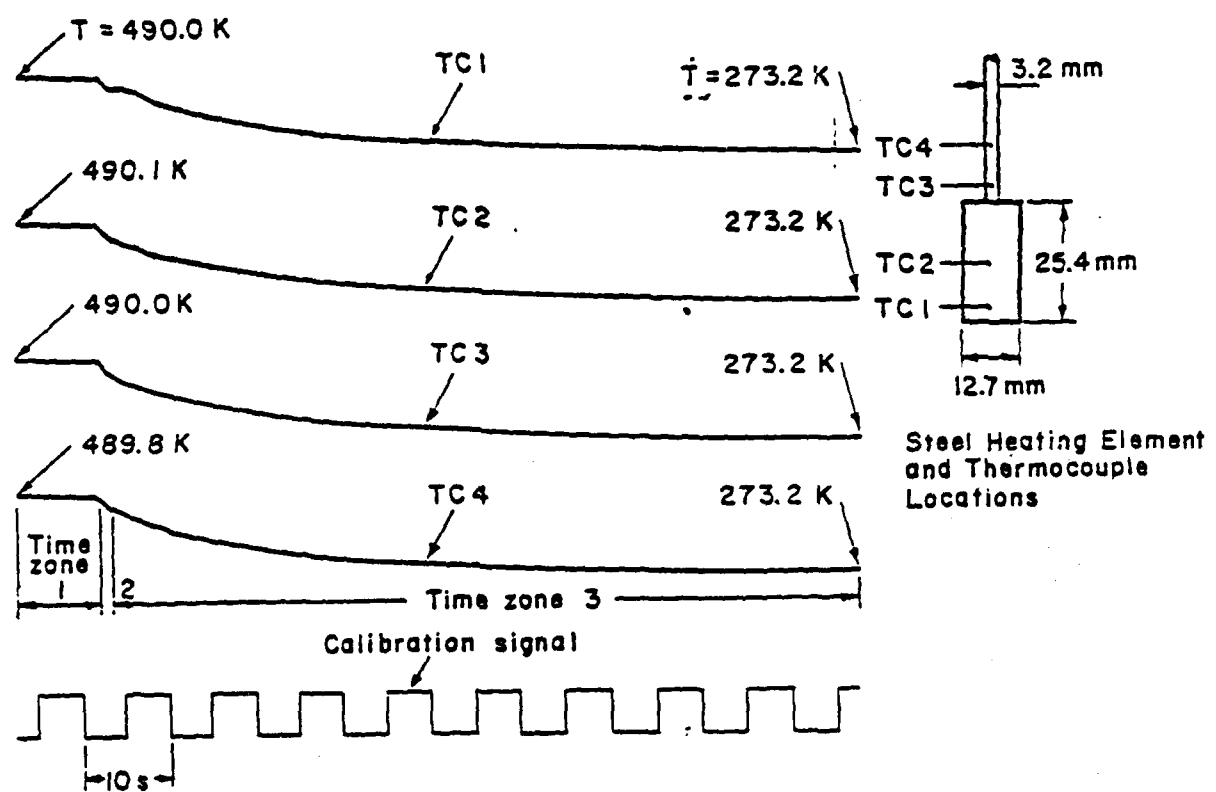


Fig. 5 Measured Temperature-Time Traces from Ice Melting and Evaporating Experiments



$t = 0.41 \text{ s}$

Fig. 6 A Color Schlieren Photograph of Ice Melting
and Evaporating Experiment

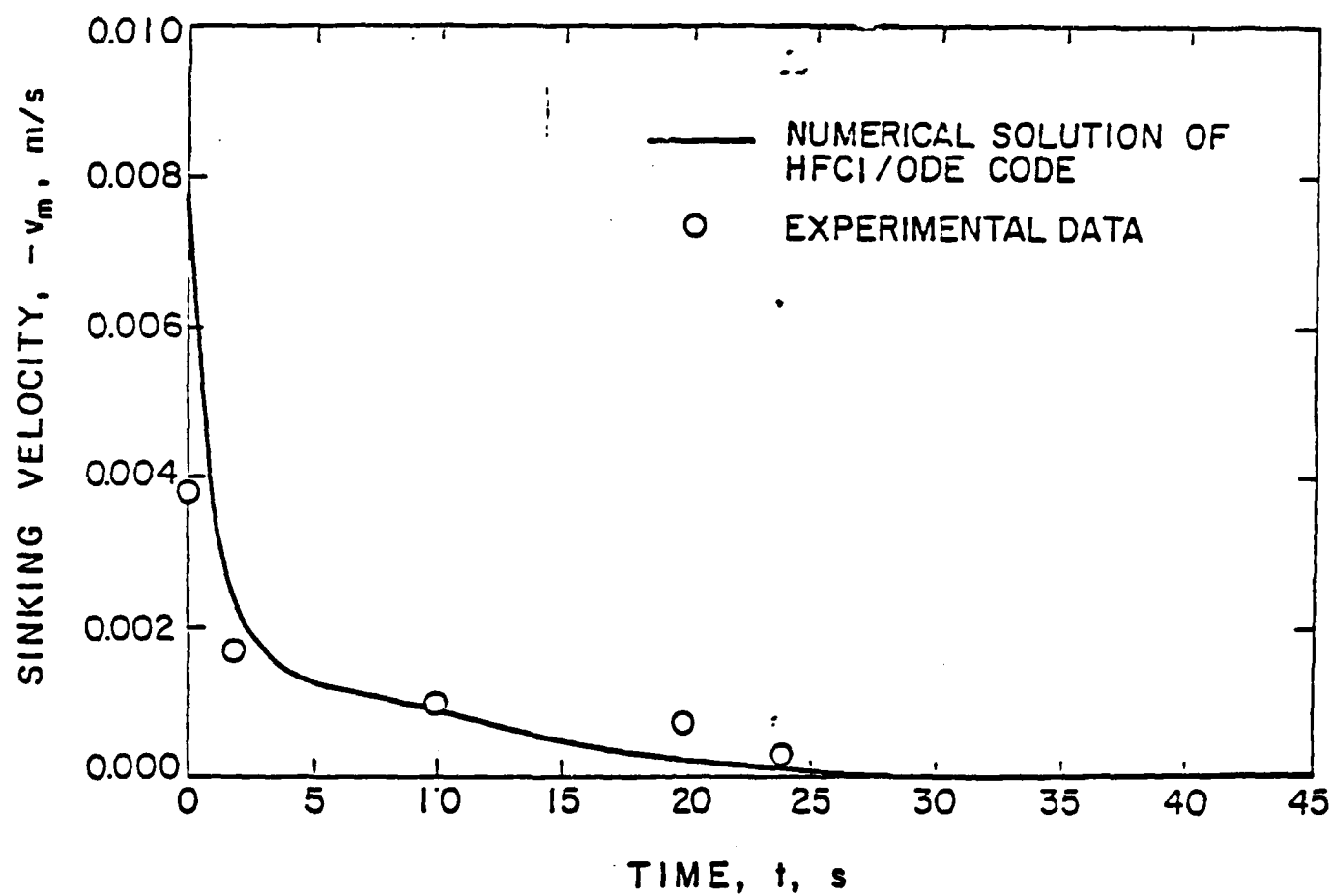


Fig. 7 Comparison of Calculated Sinking Velocity of the Spall Particle with the Measured Data Obtained from Ice-Melting and Evaporating Experiment

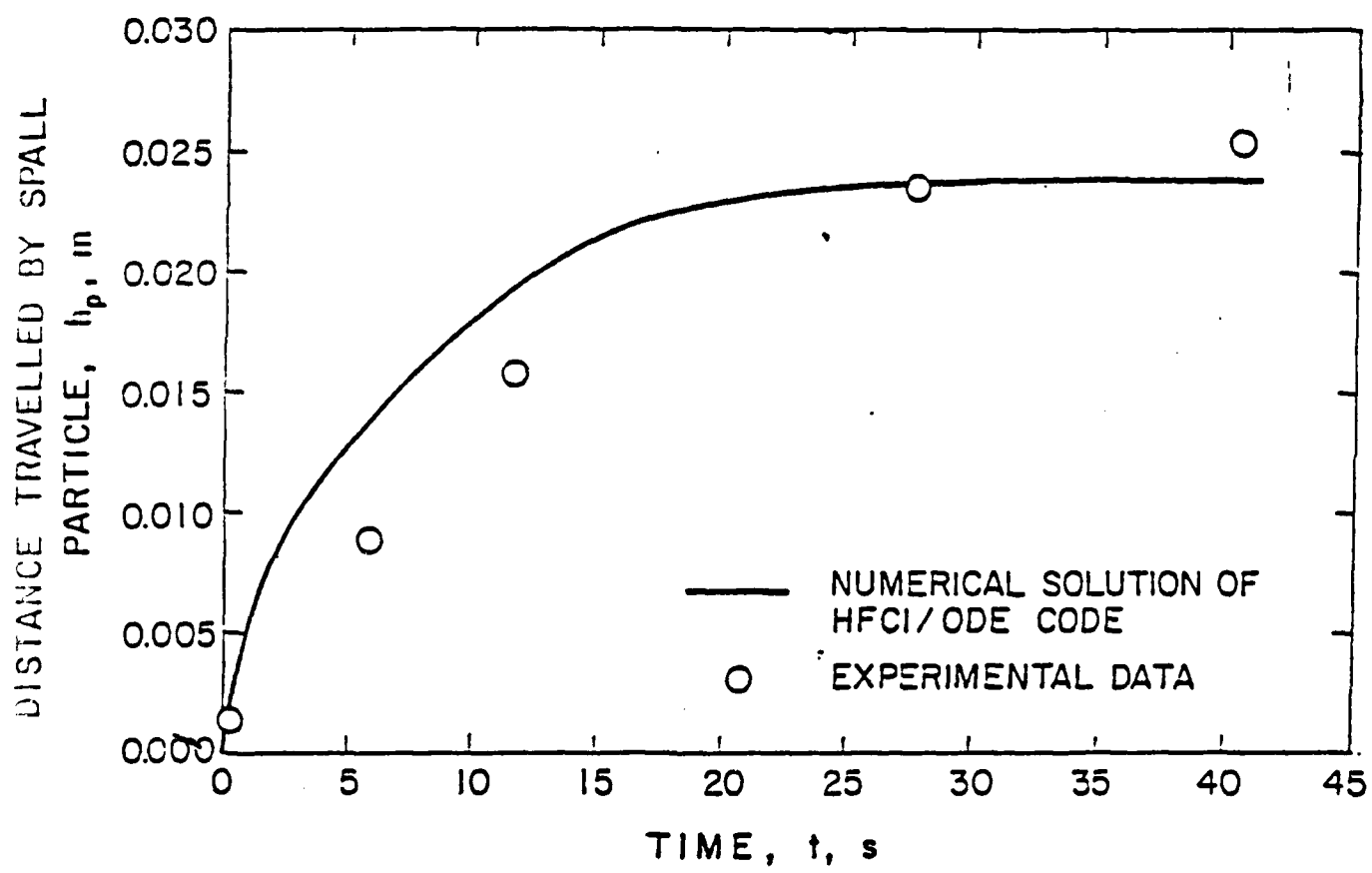


Fig. 8 Comparison of Calculated Spall Particle Trajectory with Data Obtained from Ice-Melting and Evaporating Experiment

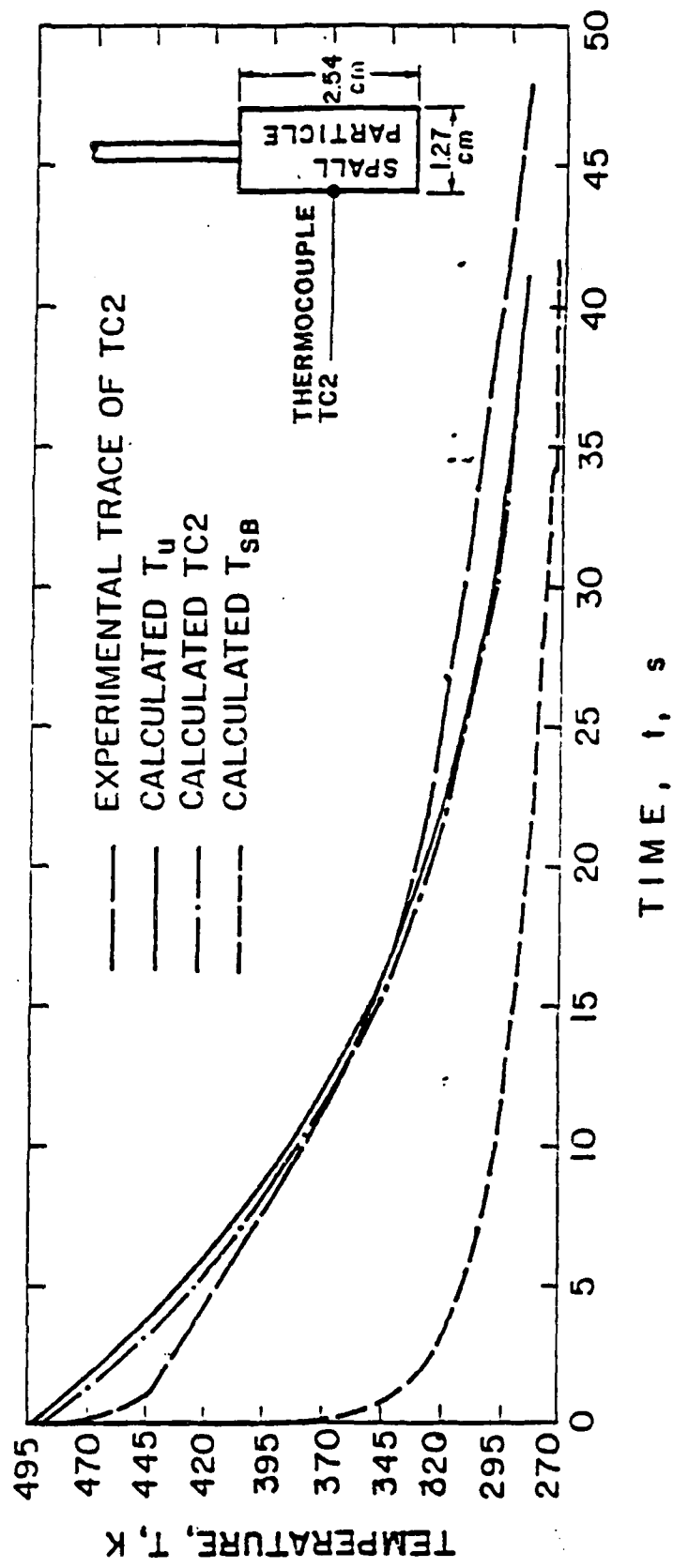


Fig. 9 Comparison of the Measured Temperature-Time Trace of TC2 with Calculated Temperature-Time Traces at the Spall-Particle Base, TC2 and Maximum Temperature Locations of the Spall Particle

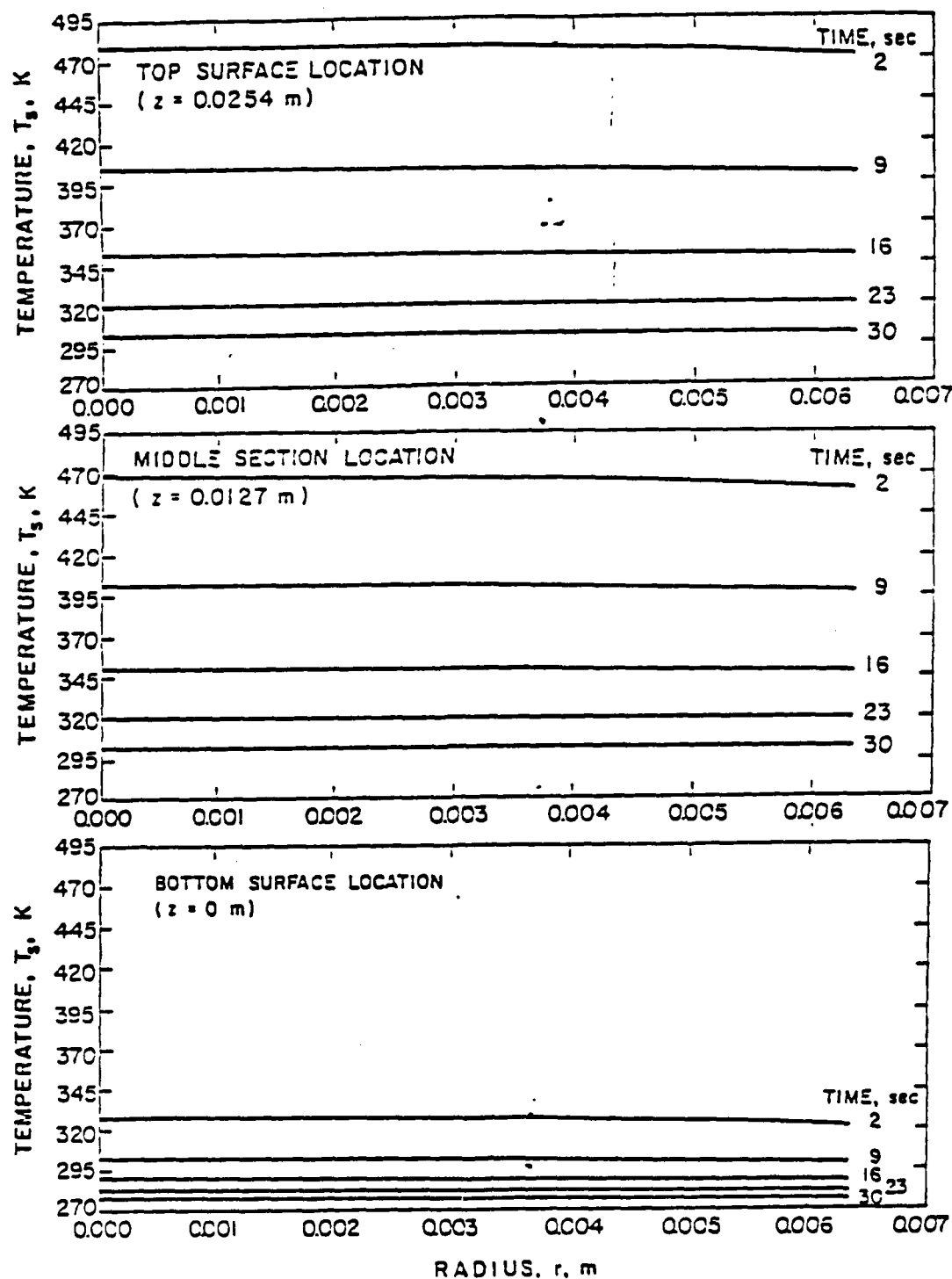


Fig. 10 Calculated Radial Temperature Profiles at the Top Surface, Middle Section, and Bottom Surface Locations of the Spall Particle for Various Times

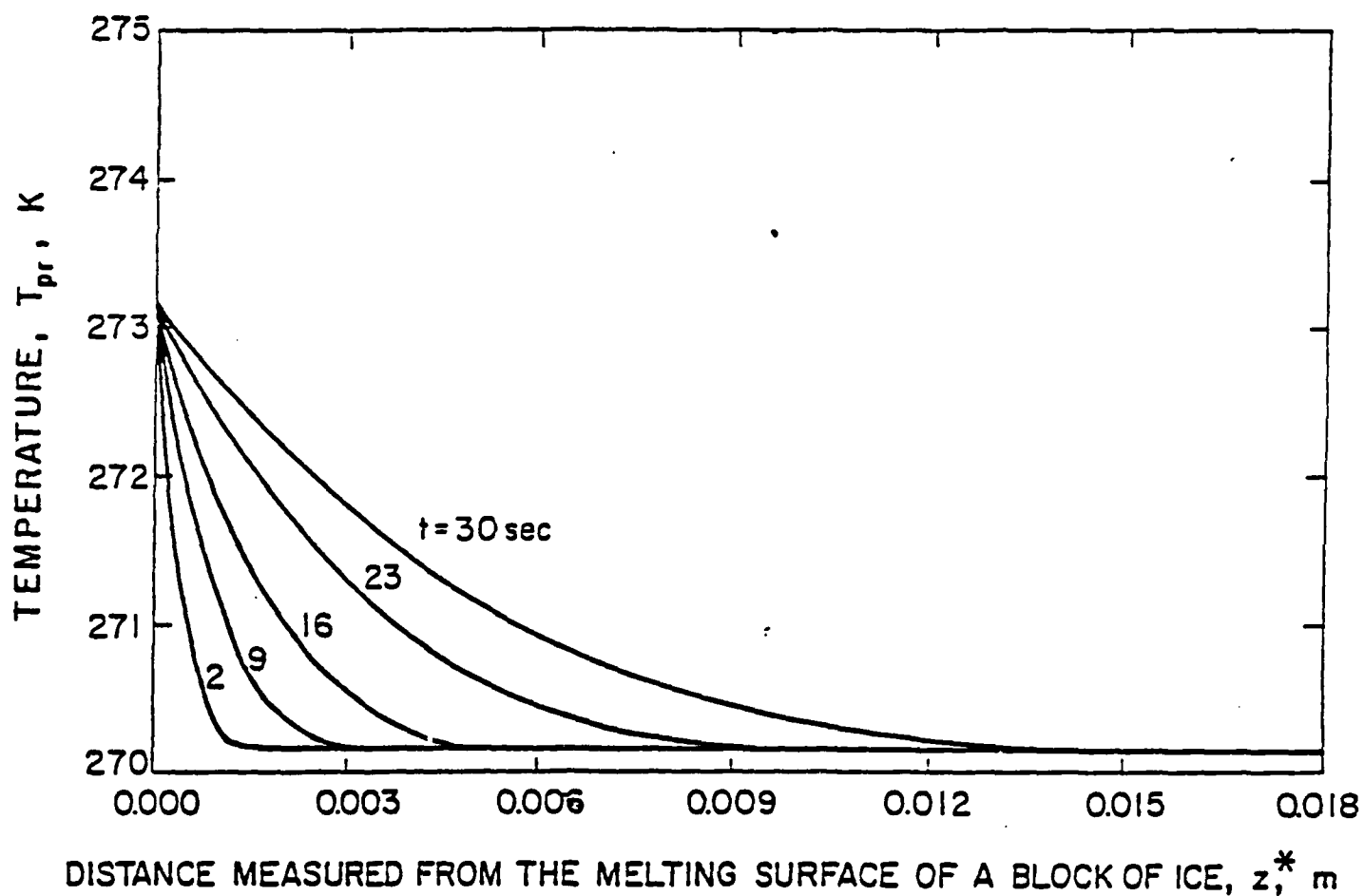


Fig. 11 Calculated Temperature Profiles in the Ice Block at Various Times

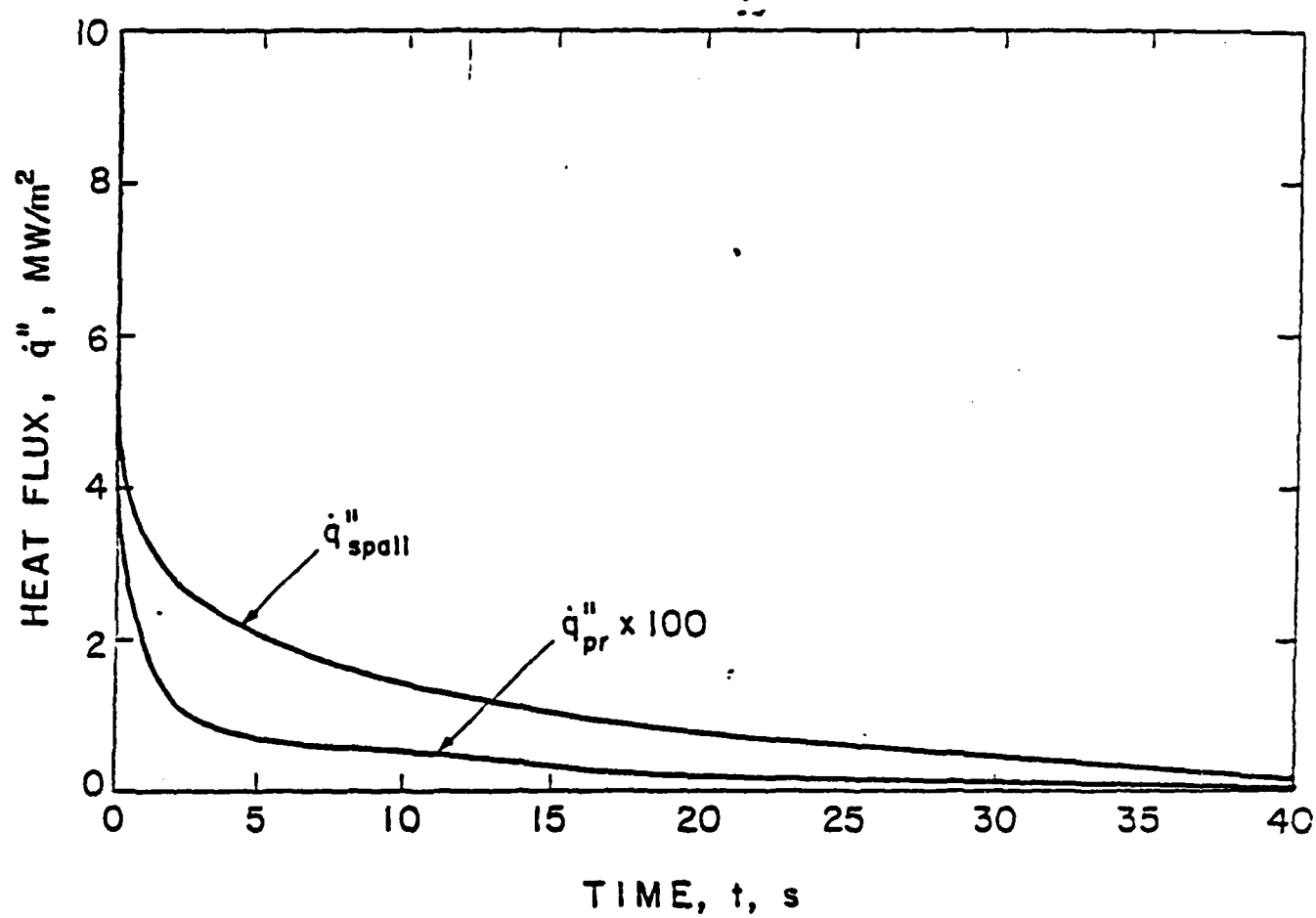


Fig. 12 Calculated Time Variation of Heat Fluxes
 \dot{q}''_{spall} and \dot{q}''_{pr}

Attachment 2

**Modeling of Hot Fragment Conductive Ignition Processes
of LOVA Propellants**

MODELING OF HOT FRAGMENT CONDUCTIVE IGNITION PROCESSES OF LOVA PROPELLANTS

K. C. Hsieh,* W. H. Hsieh,* K. K. Kuo[†]
 Department of Mechanical Engineering
 The Pennsylvania State University
 University Park, PA 16802

and

M. S. Miller#
 U.S. Army Ballistic Research Laboratories
 Aberdeen Proving Ground, Maryland 21005

ABSTRACT

A comprehensive theoretical model and an efficient numerical program have been developed to simulate the hot fragment conductive ignition (HFCI) processes for characterizing the degree of vulnerability of various gun propellants. In the formulation of the theoretical model, three sets of governing equations and their boundary conditions were derived for different regions consisting of the hot spall particle, the LOVA propellant, and the foam layer produced by liquefaction, pyrolysis, and decomposition of the propellant. In terms of chemical kinetic scheme, a two-step reaction model is proposed, based upon DSC experiments. The model contains an endothermic decomposition process followed by an exothermic pyrolysis of the propellant. Calculated results compared well with experimental data in temperature-time traces, trajectory of spall particles sinking into the LOVA propellant, and terminal position of the particle for quenched cases.

NOMENCLATURE

A	Arrhenius frequency factor of chemical reaction of melt or foam layer in Region 1, kg/m ³ -s
A _i	Interface area between liquid melt and gas bubbles, m ²
C _p	constant-pressure specific heat, J/kg-K
C _s	specific heat of spall particle, J/kg-K
D _b	averaged diameter of bubbles generated from gasification process, m
E _a	activation energy of chemical reaction of melt or foam layer, J/mole
ΔH _f	heat of formation, J/kg
L _m	height of melt or foam layer in Region 1, m
ṁ _{gnet}	net rate of production of gaseous mass in Region 1 of foam layer, kg/s
Q _L	heat release due to exothermic reaction from liquid melt to gaseous products, J/kg
Q _{melt}	heat of endothermic reaction from solid propellant to liquid melt, J/kg
q _{gas}	heat flux transferred to gas phase from spall particle base, W/m ²
q _{gas-liq}	heat flux transferred to liquid phase from gas phase through interface, W/m ²
q _{liq}	heat flux transferred to liquid phase from spall particle base, W/m ²
q _{liq-solid}	heat flux transferred to propellant surface from foam layer, W/m ²
q _{pr}	heat flux transferred to LOVA propellant from melt or foam layer in Region 1, W/m ²
q _{spall}	heat flux at base of spall particle, W/m ²

*This work was performed under contract DAAK11-83-C-0015, sponsored by the Applied Ballistic Branch of the Ballistic Research Laboratories under the support and encouragement of Dr. Joseph J. Rocchio and Mr. Norman Gerri. The authors would like to thank Dr. M. Kumar for his participation in the early stage of this research.

#Research Assistant

†Distinguished Alumni Professor of Mechanical Engineering

#Research Physicist

R_u	Universal gas constant, 8314.4 J/kg-mole-K
r_s	radius of spall particle, m
$T_b (=T_{sat})$	boiling temperature of liquid melt, K
T_g	gas temperature, K
T_m	bulk temperature of melt or foam layer, K
T_{melt}	melting temperature of LOVA propellant, K
T_p	temperature of LOVA propellant, K
T_{ps}	average surface temperature of LOVA propellant exposed to air, K
T_s	temperature of spall particle, K
v_{gr}	radial velocity of melt or foam layer in Region 1, m/s
v_s or $-v_m$	sinking velocity of spall particle, m/s
z	axial distance above base of spall particle, m
z^*	axial distance below instantaneous surface of propellant under foam layer, m

Greek Symbols

α	thermal diffusivity, m^2/s
δ_{pr}	thermal penetration depth from propellant surface, m
λ	thermal conductivity, W/m-K
ρ	density, kg/m ³
ψ	average porosity (void fraction) of foam layer in Region 1
ν	dynamic viscosity, kg/m-s

Subscripts

g	gas-phase
i	initial condition
l	liquid-phase
$melt$	melt liquid melt
pr or p	propellant
r	room condition
1	Region 1 of foam layer

Superscript

* $T^* = T - T_{ref}$

INTRODUCTION

In the selection of low vulnerability ammunition (LOVA) propellants, go/no-go ignition tests with hot metallic elements are often conducted to simulate hot fragment conductive ignition (HFCI) processes. These hot fragments can be considered as those generated from the penetration of armor plates by shaped charge jets or kinetic energy penetrators. One way to negate the threat of propellant ignition by hot spalls is to use a propellant which is resistant to conductive ignition. A number of investigations on this subject have been conducted, both theoretically and experimentally, in recent years [1-12]. Since a review of pertinent work is given in the paper by Kuo et al. [12], detailed reviews are omitted here. Only major findings of HFCI processes are listed below.

- Binders of nitramine composite propellants were found to have a strong effect on conductive ignition. Some binders can act as fire retardant coolants.
- The relative susceptibility of LOVA propellants to ignition by spall particles can be determined from ignition map based upon the plot of the initial temperature versus weight of the spall fragment.
- The contact resistance between hot particle and propellant significantly affects the delay time for onset of runaway ignition.

4. Binders which endothermically decompose under acid catalysis are more desirable for LOVA propellant binder ingredients.
5. The ignition temperatures of LOVA propellants are similar to their nitramine fillers.
6. For certain LOVA propellants, liquefaction and bubble formation were observed during conductive heating. This suggests that the thermal insulation properties of binder products may be important in the determination of ignition sensitivities of LOVA propellants.
7. Based upon surface thermocouple measurements during HFCI tests, the initial condensed phase reactions are endothermic. The endothermicity of these reactions showed good correlation with propellant sensitivity for thermal ignition.
8. The minimum spall particle temperature (for a fixed spall particle weight) depends strongly on binder composition.
9. Chemical reactions leading to ignition of certain LOVA propellants during HFCI experiments can be idealized as a two-step sequence of global reactions in which an endothermic reaction is followed by an exothermic reaction.

Several attempts were made to model the hot fragment conductive ignition processes [9-11]; however, these models have serious limitations in simulating actual HFCI processes. The model proposed in Ref. 9 is strictly one-dimensional, and allows no space for the products in the gas or liquid phases to exit at the interface between propellant samples and hot inert fragments. The model proposed in Ref. 10 requires no depletion of propellant when the hot fragment penetrates the combustible material. Also, no surface reaction is allowed in the model. An interesting theoretical analysis of the ignition of reactive solids by direct contact with a hot inert body was performed by Linan and Kindelan [11]. Their analysis considered both cylindrical and spherical geometries. Asymptotic solutions for large activation energies were obtained. The solution indicated the existence of an ignition boundary beyond which runaway ignition occurred. Although the theoretical results indicated the correct trend in terms of inert particle initial temperature and particle size, their solutions were not compared with any experimental data. Furthermore, the assumption of high activation energies are invalid for various LOVA propellants. There was no provision for the development of a foam layer at the interface region between hot fragment and propellant.

A comprehensive theoretical model was recently developed by Kuo et al. [12] to describe the heat transfer processes in hot fragment and solid propellant, as well as the development of a foam and/or melt layer which has been experimentally observed at the interface zone between solid propellant surface and hot spall particle. In this model, the liquefaction, surface reaction, and gas-phase reactions in the foam layer were considered. The effect of binder composition can also be studied by using measured kinetic data from separate DSC experiments for LOVA propellants with various binders. Thus, the ability of resisting conductive ignition of new propellant formulations can be evaluated for achieving reduced system vulnerability.

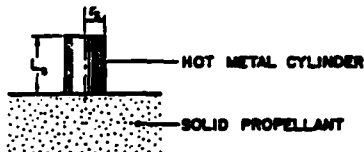
Although the model presented in Ref. 12 includes both reacting and non-reacting cases, only the non-reacting part of the model was verified by ice-melting and evaporation experiments. The main objective of this paper is to verify the chemically reacting part of the model. The latest reaction mechanism and data obtained by Miller et al. [8] have been incorporated into the model. Numerical simulation of HFCI processes of certain LOVA propellants have been conducted, and the results are compared with the data obtained by Miller and Cohen [13] for model validation.

METHOD OF APPROACH

DESCRIPTION OF PHYSICAL EVENTS

In an HFCI experiment, a hot metal particle comes into contact with a cold propellant at Time 0. In the early phase of the process (Time Period I), heat is conducted from the hot particle to the propellant without any phase change or pyrolysis (see Fig. 1). As time progresses, the temperature of the propellant increases and that of the particle decreases. Following a period of inert heating, the propellant starts to decompose, melt, and/or gasify (Time Period II). During Time Period II, a foam or melt layer usually exists near the interface region between the hot fragment and solid propellant. Since the density of the metal particle is much higher than the density of the decomposed propellant, it displaces the decomposed propellant and becomes imbedded in (sinks into) the propellant, as shown in Fig. 1. The decomposed species can further react exothermically in the gas phase, foam layer, and/or condensed (solid, liquid) phase to cause ignition. If the rate of heat release in the foam layer is lower than that of the heat loss to the surrounding and ambient materials, the spall particle will be quenched without introducing ignition. Self-sustained ignition will occur only if the rate of heat generated by the exothermic reactions exceeds the rate of heat loss. In view of the importance of chemical reactions in the foam layer and surface region of solid propellants, effective kinetic mechanisms must be determined and accurate kinetic data obtained. This information and data are then fed into the theoretical model for realistic simulations.

TIME PERIOD I (BEFORE THE FORMATION OF A MELT LAYER)



TIME PERIOD II (AFTER THE FORMATION OF A MELT LAYER)

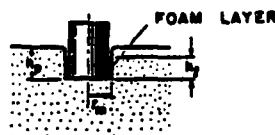


Fig. 1 Physical Event of Hot Fragment Conductive Ignition (HFCI) Processes Represented by Various Cases in Two Different Time Periods

DETERMINATION OF EFFECTIVE IGNITION KINETICS FOR THE SAMPLE PROPELLANT

Efforts to identify elementary reactions and measure their reaction rates were ruled out as probably infeasible from a technical standpoint, and certainly inappropriate to the scope of the modeling effort and the resources available for numerical computations.

Since the main interest in these reactions is the energy source (or sink) terms in heat transfer equations, Differential Scanning Calorimetry (DSC) was chosen as a suitable technique for measuring reactive heat exchange of decomposing propellant in contact with a metal surface. Operated in ramp mode, this instrument can increase the sample temperature linearly with time at rates up to 100°C/min. Although ignition by hot fragments could involve much higher instantaneous heating rates, these high rates cannot be sustained for any appreciable time due to conductive and convective loss mechanisms. Because observations of hot fragment ignition under controlled conditions indicate that 5 seconds or more are required to establish ignition, the 100°C/minute limitation may not be too restrictive.

The propellant used in this study has a unimodal distribution of RDX particle sizes (about 5 micron average). The DSC test samples were microtomed to a uniform thickness of about 0.4 mm with mass of about 1 mg (±5%) and placed in covered and crimped pans perforated in four places with a straight pin. The pan perforations allow for pressure release, while retaining the bulk of any decomposition heat resulting from reactions occurring at or very near the propellant surface. Thus, the technique does not distinguish between energetic reactions in the solid, liquid, or gas phase; the goal is only to measure net "localized" energy release (or absorption).

DSC thermograms for the test propellant used here typically exhibited an endotherm of about 20 cal/g, starting at about 185°C and followed by an exotherm of about 300 cal/g which peaks at about 260°C. At the onset of this study, the intention was to treat the exotherm as a simple global reaction and the endotherm as a phase change. Ultimately, both were described as separate single reactions, each with its own set of kinetic parameters. A detailed analysis was reported in Ref. 8. The reaction mechanism proposed by Miller et al. [8] is a two-step sequence of global reactions represented by the following equations.



where the specific reaction rate constants k_1 and k_2 can be expressed in the Arrhenius form

$$k_1 = A_1 \exp\left(-\frac{E_1}{R_u T}\right) \quad (2)$$

$$k_2 = A_2 \exp\left(-\frac{E_2}{R_u T}\right) \quad (3)$$

In the curve-fitting process, Miller et al. found that the Arrhenius coefficient, A_1 can be satisfactorily represented by a constant, and A_2 can either be approximated by constants or expressed as a power law of heating rate (r) in their DSC experiments, i.e.,

$$A_2 = \text{constant} \quad \text{or } A_2 = a_2 r^b \quad (4)$$

A typical comparison of the data with the fitted curve is shown in Fig. 2. The constant A_2 fitted curve is slightly different from the curve shown in Fig. 2, and is equally acceptable for numerical simulation of HFCI processes. Considering the enormous simplification of the actual chemistry afforded by the irreversible two-step idealization, the quality of representation is quite good. Good representations of the data are found for a wide range of heating rates and inert gas purge flow rates. The DSC data for the sample propellant is summarized in Table 1, where Q_1 and Q_2 are the specific heat release for endothermic and exothermic reactions.

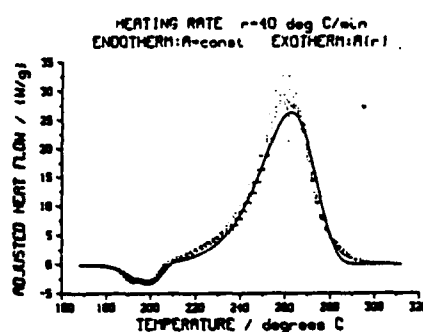


Fig. 2 Comparison of Composite DSC Thermograms (Points) to Fitted Curve Using Heating Rate Dependent A_2 Factor

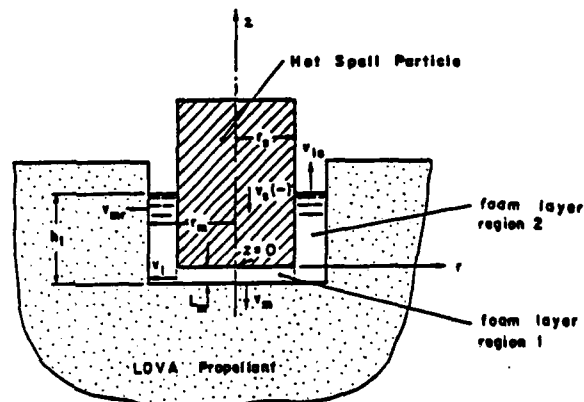


Fig. 3 Schematic Diagram of the Model

Table 1. Kinetic Constants Determined from DSC

A_1 (s^{-1})	A_2 (s^{-1})	E_1 (Kcal/mol)	E_2 (Kcal/mol)	a_2 (s^{b_2-1}/k^{b_2})	b_2 (--)	Q_1 (cal/g)	Q_2 (cal/g)
1.31×10^{31}	1.98×10^{14}	69.4	38.2	----	----	-21.1	297
$\pm 0.57 \times 10^{31}$	$\pm 0.80 \times 10^{14}$	± 0.4	± 0.4	----	----	± 5.6	± 26
----	----	----	47.2	7.79×10^{17}	-0.516	----	297
----	----	----	± 0.4	$\pm 2.89 \times 10^{17}$	± 0.014	----	± 26

Incorporation of Two-Step Global Reaction Kinetics into the HFCI Theoretical Model

Before describing the specific steps taken in incorporating the two-step global reaction kinetics into the HFCI model, it is useful to give a brief summary of the model structure. As described in Ref. 12, the physical model is divided into various regions (see Fig. 3): 1) spall particle region; 2) foam layer region 1; 3) foam layer region 2; and 4) LOVA propellant region. Each region has its own governing equations and boundary conditions.

In order to incorporate the two-step global kinetics into the HFCI model, the main modification is concentrated on the formulation of foam layer Region 1, which is the area controlling the onset of ignition.

Due to the limited kinetic data resources available for LOVA propellants at the time the HFCI model was initially formulated, a more general consecutive three-step reaction from solid propellant to gaseous products was adopted, i.e.,



With the consideration of the third reaction, the heat released in the gas-phase reaction could increase the temperature of the gases in the foam layer. However, from the DSC experiments [8], a two-step global reaction was proposed, as discussed above.

Based upon two-step reaction kinetics and energy flux balance shown in Fig. 4a, the equation describing the rate of change of gas-phase temperature can be derived as follows.

$$\begin{aligned} \pi r_s^2 L_m \rho_{pg} C_{pg} \frac{DT}{Dt} &= \dot{q}_{gas}'' \pi r_s^2 - \dot{q}_{gas-liq}'' A_{11} \\ &+ \dot{m}_{g_{net},1} [(C_{pg} T_l^* + \Delta H_{f,l}^0) - (C_{pg} T_g^* + n \Delta H_{f,g}^0)] \\ &+ RT_{ref} \rho_g v_{lri}^2 \pi r_s^2 L_m \psi f \end{aligned} \quad (6)$$

where n can be considered as the combustion efficiency in the foam layer.

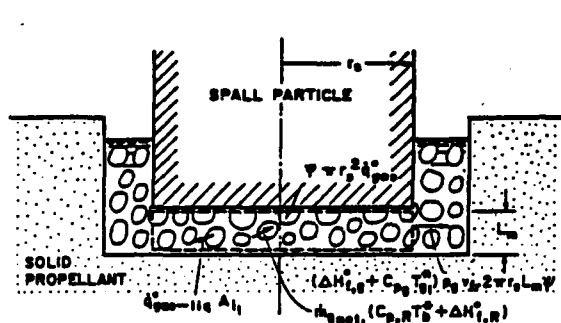


Fig. 4a Energy Fluxes Associated with the Gas Phase in Region 1 (The Thickness of Foam Layer is Highly Exaggerated)

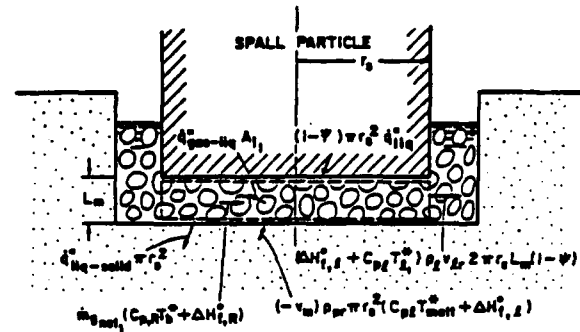


Fig. 4b Energy Fluxes Associated with the Liquid Phase in Region 1 (Thickness of Foam Layer is Highly Exaggerated)

For the liquid phase, the balance of energy fluxes are given in Fig. 4b, and the equation of liquid-phase temperature can be written as

$$\begin{aligned} (1-\psi) \pi r_s^2 L_m \rho_l C_{pl} \frac{DT}{Dt} &= v_m \rho_{pr} \pi r_s^2 C_{pl} (T_l - T_{ps}) \\ &+ \dot{q}_{liq}'' (1-\psi) \pi r_s^2 - \dot{q}_{liq-solid}'' \pi r_s^2 + \dot{q}_{gas-liq}'' A_{11}, \end{aligned} \quad (7)$$

From the mass balances for both gas and liquid phases, the following equations can be obtained after certain manipulations.

$$\begin{aligned} \frac{D\psi}{Dt} &= \frac{(1-\psi)R}{(1-\psi+f\psi) \pi r_s^2 L_m \rho_{pg} C_{pg}} \{ \dot{q}_{gas}'' \pi r_s^2 - \dot{q}_{gas-liq}'' A_{11} \\ &+ RT_{ref} \rho_g v_{lri}^2 \pi r_s^2 L_m \psi f + \dot{m}_{g_{net},1} Q_L \} \\ &+ \left[\frac{(1-\psi) \rho_l + f\psi \rho_g}{(1-\psi+f\psi) \rho_g} \right] \frac{\dot{m}_{g_{net},1}}{L_m \pi r_s^2 \rho_l} + \frac{f\psi \rho_{pr}}{(1-\psi+f\psi) L_m \rho_l} v_m \end{aligned} \quad (8)$$

where

$$Q_L = (C_{pl} T_l^* + \Delta H_{f,l}^0) - (C_{pg} T_g^* + n \Delta H_{f,g}^0) \quad (9)$$

$$\begin{aligned} v_{\text{int}} = & \frac{R}{2\pi r_s^2 m C_p g} [q''_{\text{gas}} \psi r_s^2 - q''_{\text{gas-liq}} A_1 + \dot{m}_{g_{\text{net},1}} Q_L] \\ & + \frac{\rho_g - \rho_{\text{pr}}}{2L_m \rho_i} \dot{m}_{g_{\text{net},1}} - \frac{r_s \rho_{\text{pr}}}{2L_m \rho_i} v_m / [(1-\psi+f\psi) - \frac{RT_{\text{ref}} \psi f}{C_p T_g}] \quad (10) \end{aligned}$$

In addition to the above four governing equations (three ODES, one algebraic equation), the perfect gas law is used to evaluate gas density. The energy flux balance at the interface between liquid melt and propellant surface can be given as

$$\dot{q}_{\text{liq-solid}} = \dot{q}_{\text{pr}} + Q_{\text{melt}} (v_s) \rho_{\text{pr}} \quad (11)$$

where the heat of reaction Q_{melt} is defined as

$$Q_{\text{melt}} (\Delta H_{f,i}^0 + C_{p,i} T_{\text{melt}}^*) = (\Delta H_{f,pr}^0 + C_{p,pr} T_{\text{melt}}^*) \quad (12)$$

The endothermic reaction from solid propellant to liquid melt absorbs heat from liquid phase via the last term in Eq. (11). The liquid phase is heated by energy transferred from gas phase through bubble interfaces in the foam layer. This mechanism is modeled as $\dot{q}_{\text{gas-liq}} A_1$ in Eq. (7). The exothermic reaction (from liquid melt to gaseous products) releases heat to elevate gas-phase temperature via the source term associated with $\dot{m}_{g_{\text{net},1}}$ in Eq. (6).

In order to close the above system, the parameter f , which relates v_{erg} (the radial velocity of the liquid phase at the lateral surface of foam layer in region 1) and v_{erg} ($v_{\text{erg}} = f v_{\text{int}}$), was expressed as

$$f = C \left[\frac{\dot{m}_{g_{\text{net},1}}}{\pi r_s^2 (-v_m + \epsilon) \rho_g} \right]^n \quad (13)$$

The above equation is based upon various limiting conditions given below.

Case 1: $f \approx 0$, when the volumetric gas generation rate is much smaller than the volumetric regression rate of the melt layer, i.e.

$$\pi r_s^2 (-v_m) \gg \dot{m}_{g_{\text{net},1}} / \rho_g$$

Case 2: $f \approx 1$, when $\pi r_s^2 (-v_m) \approx \dot{m}_{g_{\text{net},1}} / \rho_g$

Case 3: $f \gg 1$, when $\pi r_s^2 (-v_m) \ll \dot{m}_{g_{\text{net},1}} / \rho_g$

To avoid singularity at the onset of melting or liquefaction of LOVA propellants, a small parameter, ϵ , in the order of 0.0001 is inserted in the denominator of Eq. (13). The coefficient C and exponent n are taken to be the unit in the HFCl simulation.

The foam layer region 1 thus contains six major unknown parameters (ψ , T_g , T_f , v_{int} , f , ρ_g , solved from Eqs. (6), (7), (8), (10), and (13), and the perfect gas law.

EMPIRICAL CORRELATIONS AND INPUT PARAMETERS

The exothermic chemical reaction plays an important role in the HFCl process, since high rates of heat release could lead to runaway ignition. Therefore, it is necessary to acquire an appropriate correlation for the chemical reaction rate. The kinetic data used in numerical calculations was obtained from Miller's DSC experiments [8]. The rate of production of gaseous mass in Region 1 of the foam layer is expressed as

$$\dot{m}_{\text{g,net}} = c_m \pi r_s^2 (1-\psi) \rho_i A_i \exp\left(-\frac{E_{\text{ag}}}{R_u T_i}\right) \quad (14)$$

where A_i is the same as A_2 given in Table 1, and c_m is a constant smaller than 1. The temperature distribution in the liquid phase of the foam layer is not strictly uniform. Most of the liquid is at a temperature lower than the liquid surface temperature of bubbles. This can influence the value of c_m . Also, the reacting surface layer of bubbles could be a small fraction of the liquid in the foam layer. Furthermore, the Arrhenius law is highly nonlinear. All of these factors could influence the effective mass generation rate. In the present lumped parameter analysis for the foam layer, the selected value of c_m in HFCI simulation is 0.02 for all cases studied.

In addition to the kinetic correlation, suitable empirical correlations for heat fluxes (e.g., $\dot{q}_{\text{liq-solid}}$, \dot{q}_{liq} , \dot{q}_{gas} , and $\dot{q}_{\text{gas-liq}}$) are also needed to properly predict heat transfer rates and system eigenvalues, that is, the sinking velocity (v_s or $-v_m$) and the propellant surface temperature (T_{ps}). The heat transfer coefficients for $\dot{q}_{\text{liq-solid}}$, \dot{q}_{liq} , and \dot{q}_{gas} are adopted in the combined form of forced convection and conduction. In the early stage of time period II (described in physical events) or before propellant ignition, the radial velocity in Region 1 of the foam layer can be quite high. Therefore, the forced convection effect dominates heat transfer among the spall particle, foam layer, and propellant. However, in the quenched cases, the conduction heat transfer is not the main mechanism during most of time period II. Some of the heat transfer correlations used are given in Ref. 12. In consideration of various forms of heat transfer correlation, it is noted that the heat transfer measurements available for foam layers are very scarce. In fact, heat transfer rates of foams generated by liquefaction and pyrolysis of solid propellant are completely unavailable. This is an area requiring further research. The heat fluxes mentioned above can be expressed as follows:

$$\dot{q}_{\text{gas}} = h_{\text{conv}} (\bar{T}_{\text{SB}} - T_g) \quad (15)$$

$$\dot{q}_{\text{liq}} = h_{\text{conv}} (\bar{T}_{\text{SB}} - T_l) \quad (16)$$

$$\dot{q}_{\text{liq-solid}} = h_{\text{conv}} (\bar{T}_m - T_{\text{ps}}) \quad (17)$$

$$\text{where } \bar{T}_m = \frac{(1-\psi)\rho_i C_{pi} T_i + \psi_p C_{pg} T_p}{(1-\psi)\rho_i C_{pi} + \psi_p C_{pg}} \quad (18)$$

The heat flux at propellant surface (\dot{q}_{pr}) is calculated from the following equation, as described in Ref. 12.

$$\dot{q}_{\text{pr}} = 3\lambda_p \left(\frac{T_{\text{ps}} - T_{\text{pi}}}{\delta_{\text{pr}}} \right) \quad (19)$$

where the coefficient $3\lambda_p$ results from a third-order polynomial approximation for the temperature profile. The time variation of the thermal wave penetration depth, δ_{pr} , is determined from

$$\frac{d\delta_{\text{pr}}^2}{dt} = 24 a_{\text{pr}} + 8 v_m \delta_{\text{pr}} - \frac{2\delta_{\text{pr}}^2}{(T_{\text{ps}} - T_{\text{pi}})} \frac{dT_{\text{ps}}}{dt} \quad (20)$$

After δ_{pr} is solved from Eq. (20), the propellant surface temperature can be determined from Eq. (11) through the use of Eqs. (17) and (19).

The sinking velocity can then be calculated by

$$v_s = \left(\frac{\dot{q}_{\text{liq-solid}} - \dot{q}_{\text{pr}}}{\rho_{\text{pr}} Q_{\text{melt}}} \right) \quad (21)$$

In addition to the above correlations and data provided in Table 1, a set of input data was prepared and listed in Table 2. The thermodynamic and transport properties were obtained from open literature [14-19].

OVERALL STRUCTURE OF THEORETICAL MODEL

The theoretical model consists of governing equations and their associated initial and boundary conditions for the hot particle, the propellant, and the foam layer. Governing equations for the

Table 2. Input Data Used in the HFCI Simulation

Region	Parameter	Value	Unit
Spall	r_s	0.3175×10^{-2} or 0.4851×10^{-2}	m
Particle	L_s	0.3937×10^{-2} or 0.98×10^{-2}	m
	λ_s	16.246	W/m-K
	C_s	5.02×10^2	J/kg-K
	ρ_s	8.0×10^3	kg/m ³
Foam Layer	λ_f	2.094×10^{-1}	W/m-K
	ρ_f	1.60×10^3	kg/m ³
	C_f	1.465×10^3	J/kg-K
	μ_f	0.832×10^{-3}	kg/m-s
	E_a, lg	1.597×10^5	J/mole
	A_2	1.98×10^{14}	1/s
	$\Delta H_{f,l}^0$	-6.695×10^5	J/kg
	$\Delta h_{f,g}^0$	-1.912×10^6	J/kg
	λ_g	36.29×10^{-3}	W/m-K
	C_{pg}	1.465×10^3	J/kg-K
	n	0.80	----
LOVA Propellant	C_{pr}	$3.852 \times 10^2 + 2.598 \times T(K)$	J/kg-K
	ρ_{pr}	1.678×10^3	kg/m ³
	λ_{pg}	2.094×10^{-1}	W/m-K
	$\Delta H_{f,pr}^0$	-7.579×10^5	J/kg
	E_a, pl	2.9×10^5	J/mole
	A_1	1.31×10^{31}	1/s

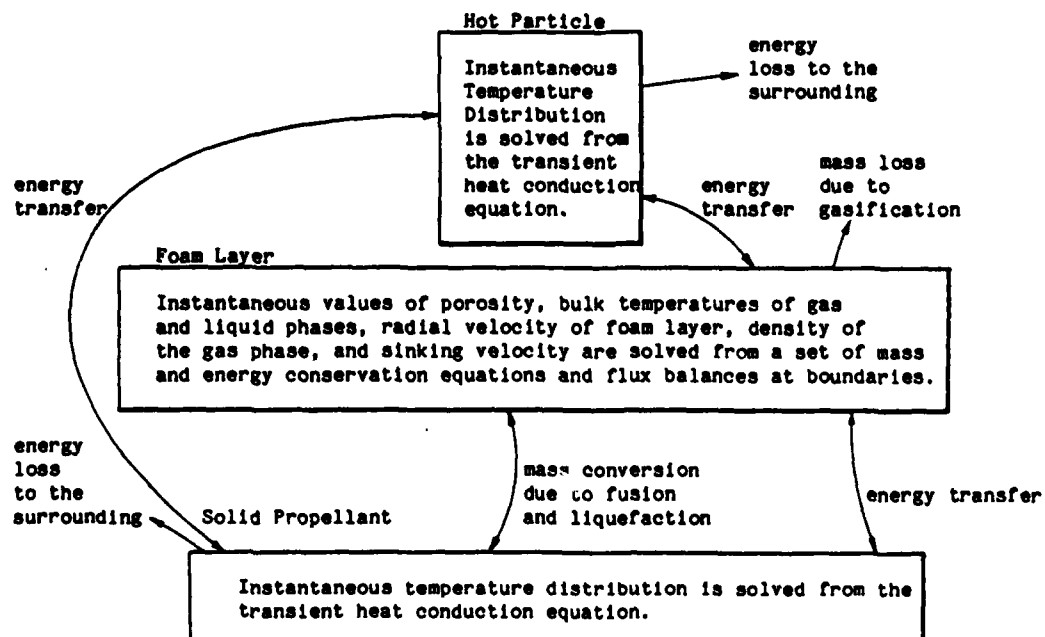


Figure 5. Block Diagram Showing the Mathematical Formulation and Coupling Relationship Between Hot Particle, Foam Layer, and Solid Propellant

hot particle and the propellant are transient heat conduction equations written in two-dimensional cylindrical form. These equations were recast into ordinary differential equations by integral methods. In these two regions, instantaneous temperature distributions are solved from the governing equations coupled to the foam layer through flux balances at their boundaries (see Fig. 5). The solution of major unknowns in the foam layer is also delineated in the same figure.

DISCUSSION OF RESULTS

In the following, one set of HFCI simulation results is compared with experimental results, and two sets of parametric runs are presented and discussed in detail. To study the initial temperature effect of the spall particle, two different temperatures (768 and 1000 K) were considered for the same spall particle size ($L_s = 0.3937$ cm, $r_s = 0.3175$ cm). The calculated results from the case with an initial temperature of 768 K are compared with experimental data obtained by Miller and Cohen [13]. The third set of results was obtained for studying the mass effect on the HFCI process using a large spall particle ($L_s = 0.98$ cm, $r_s = 0.4851$ cm).

Figure 6 shows a set of propellant subsurface temperature profiles at different times before the spall particle begins to sink into the LOVA propellant. As one can see from the temperature profile variation, the thermal wave penetration depth becomes deeper as time increases. However, the surface temperature remains approximately at the 735 K range.

The axial temperature variation at the center line of the spall particle is shown in Fig. 7 for different times in time period I. This figure indicates the decay of maximum temperature at a distance far from the spall particle base. The temperature gradient at the base of the spall drops from a large value upon initial contact, to a much lower level at 1.3 s. At the end of time period I, the axial temperature distribution becomes quite uniform.

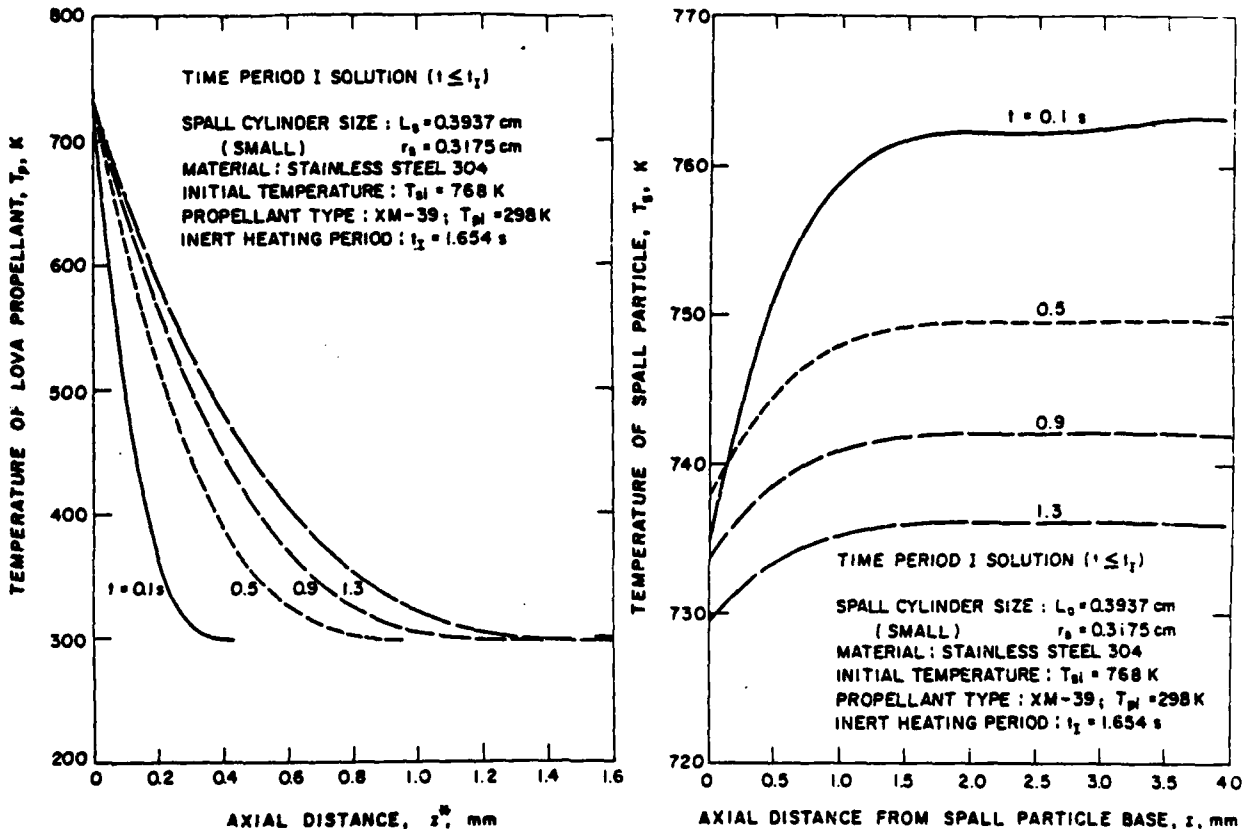


Fig. 6 Calculated Temperature Distributions in the LOVA Propellant at Various Times

Fig. 7 Calculated Axial Temperature Distributions Along the Centerline of the Spall Particle at Various Times

In time period II, the spall particle sinks into the LOVA propellant. The calculated sinking distance versus time is compared with measured data in Fig. 8. The calculated sinking velocity is also shown in this figure. Note that the sinking velocity (the slope of the curve) increases rapidly at the very beginning, starts to decrease at $t = 0.75$ s, and approaches zero at the end of the calculation ($t=34$ s). The final calculated sinking distance is about 15% larger than the measured one. This discrepancy could be caused by errors in experimental measurement as well as any inappropriate of heat transfer correlation used in the foam layer of the theoretical model. In general, this comparison shows a reasonable agreement between calculated and measured results.

The calculated time variation of the void fraction in the foam layer [$\psi(t)$] is shown in Fig. 9. When the spall particle starts to sink into the LOVA propellant, ψ increases drastically due to intensive heating, and then slows down significantly as time increases at the end of computation; only 72% of the space in the foam layer is occupied by the gas. The calculated time variations of center and base temperatures of the spall particle are compared with thermocouple measurements at corresponding locations in Figs. 10 and 11, respectively. Comparison of the predicted base temperature is better than comparison of the predicted center temperature with experimental data. Both of these temperatures decline monotonically as the particle begins to sink into the LOVA propellant and approach asymptotic levels near the end of computation.

The calculated time variation of the instantaneous subsurface temperature of the first thermocouple location (6 mm below the initial propellant surface) compares well with measured data, as shown in Fig. 12. Like the measured data, the calculated subsurface temperature at the second thermocouple location (12 mm below the surface) shows no response at the end of calculation ($t=34$ s).

Comparison of bulk temperatures of gas and liquid phases in the foam layer is shown in Fig. 13. During time period II, the gas-phase temperature is always higher than that of the liquid. The temperature difference decreases monotonically and reaches a small difference near the end of computation.

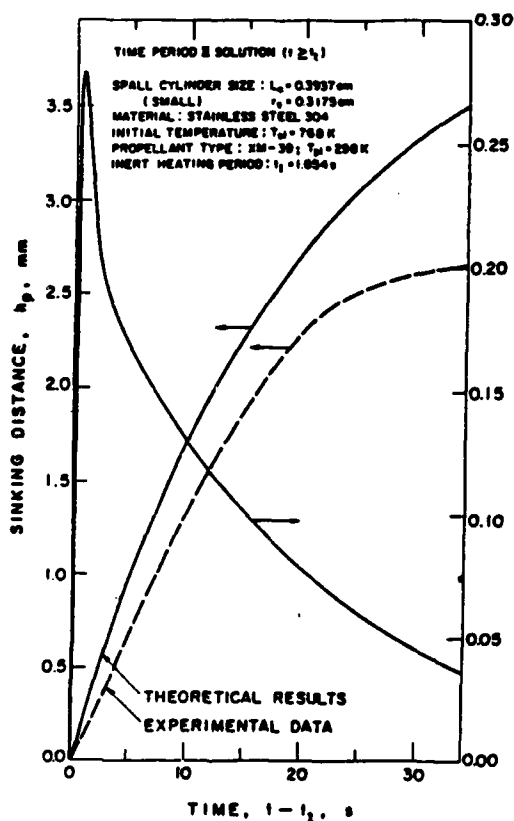


Fig. 8 Comparison of Calculated Time Variations of Sinking Distances with Experimental Data and Calculated Time Variation of Sinking Velocity of the Spall Particle

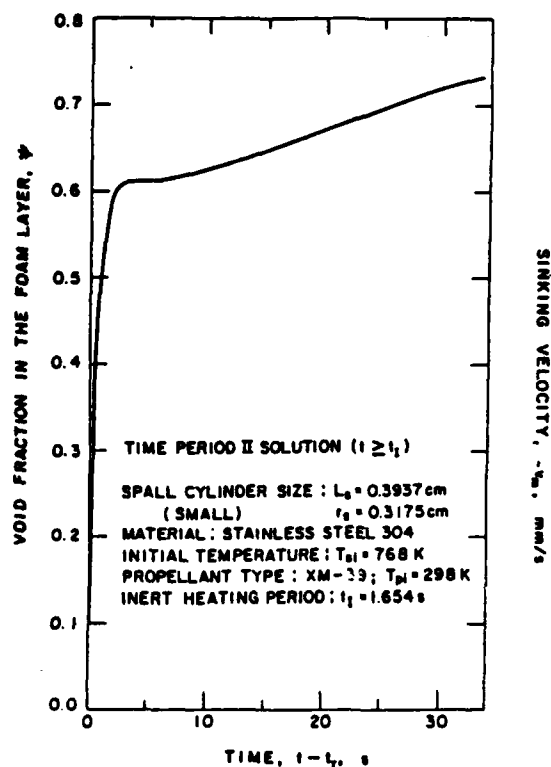


Fig. 9 Calculated Time Variation of the Void Fraction in the Foam Layer

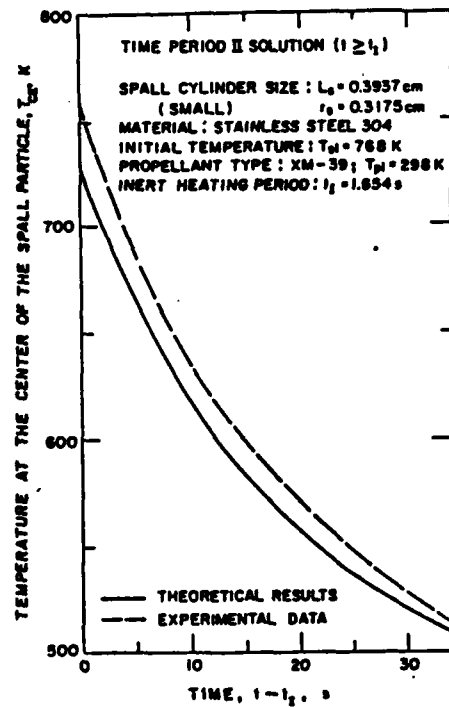


Fig. 10 Comparison of Calculated Temperature-Time Trace at the Center of the Spall Particle with Experimental Data

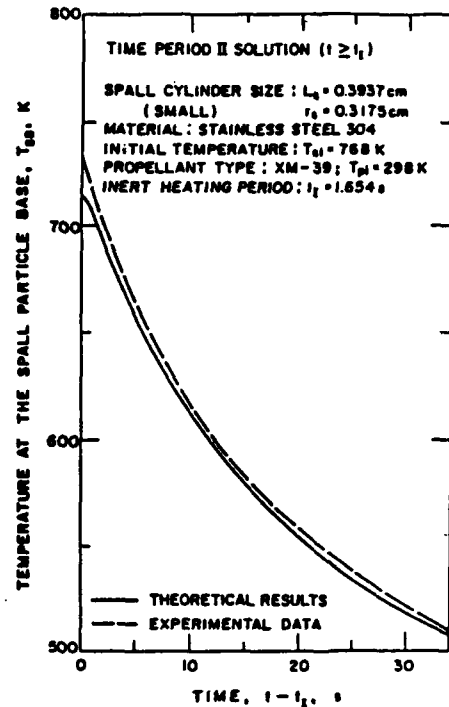


Fig. 11 Comparison of the Temperature-Time Trace at the Bottom Surface of the Spall Particle with Experimental Data

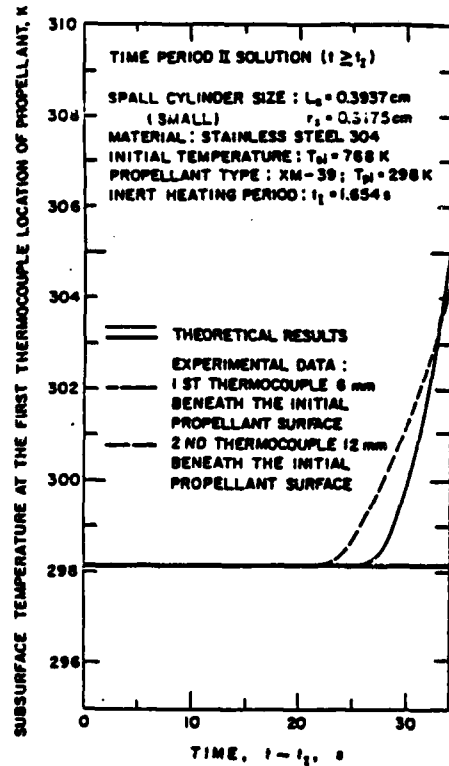


Fig. 12 Comparisons of Predicted Temperature-Time Traces at the First and Second Thermocouple Locations (6 and 12 mm Below the Propellant Surface) with Experimental Data

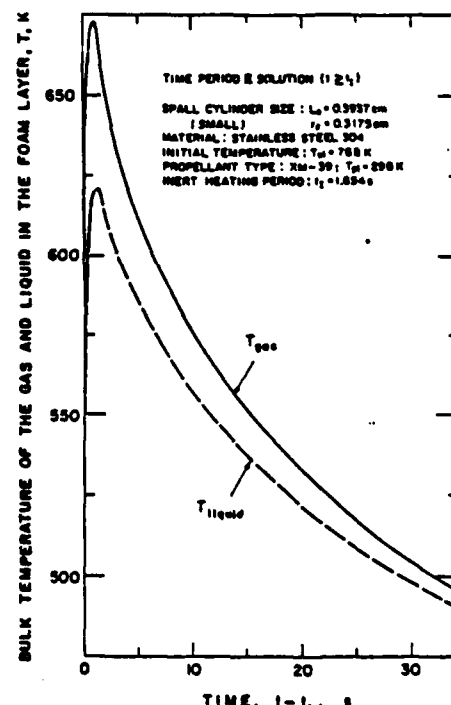


Fig. 13 Calculated Temperature-Time Traces of Gas and Liquid Phases in the Foam Layer

In addition to the quenched case discussed above, two separate HFCI tests were conducted by Miller and Cohen [13], using different spall particle sizes and initial temperature. The small cylindrical particle has a radius of 0.3175 cm and a length of .3937 cm, with an initial temperature of 986 K at the time of contact with the LOVA propellant. The large cylindrical particle has a radius of 0.4851 cm and a length of 0.98 cm, with an initial temperature of 951 K at the time of contact with the LOVA propellant. In both cases, the propellant ignited. The pyrolyzed gases are not luminous near the base region of the spall particle. The observed luminous flame is above the initial propellant surface. The flame widens abruptly at 5.2 and 1.2 s, corresponding to the small and large particles, respectively. Widening of the flame could be considered as onset of sustained ignition from the experimental point of view.

To validate the theoretical model with the ignited cases, both tests were simulated. Results are discussed below. Figure 14 shows the comparison of calculated trajectories of spall particles with experimental data. The small particle has a slightly higher initial temperature than the large one, and hence sinks into the LOVA propellant at a slightly higher velocity (see Fig. 15). At a later time, the velocity of the large particle is higher since it contains more thermal energy. The calculated trajectory shown in Fig. 14 overpredicts the experimental data by 25% at the end of the run. However, the agreement is still acceptable for most of the event. For these two cases, the particles sink continuously as the propellant reaches sustained ignition conditions. The calculated sinking velocity variations with respect to time, shown in Fig. 15, exhibit spikes during the initial interval when the particles are extremely hot.

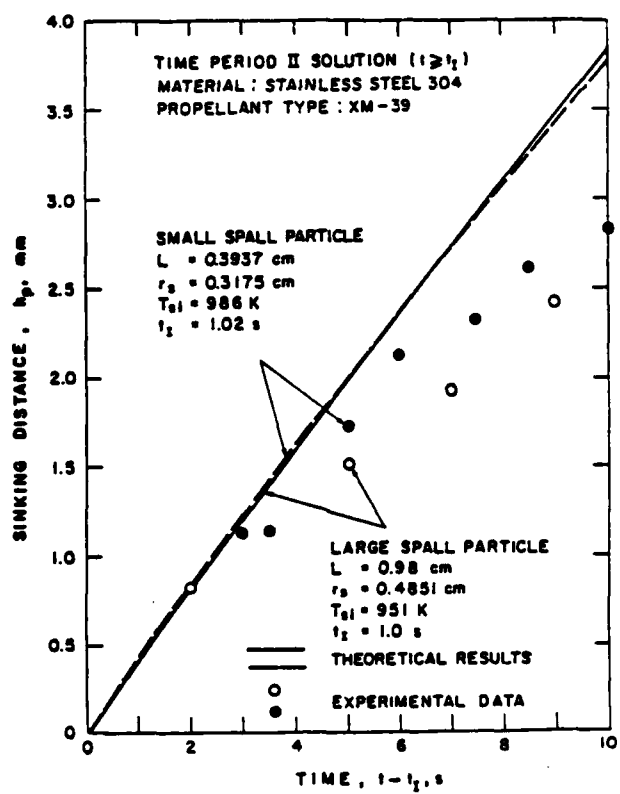


Fig. 14 Comparison of Calculated Time Variations of Sinking Distances with Experimental Data

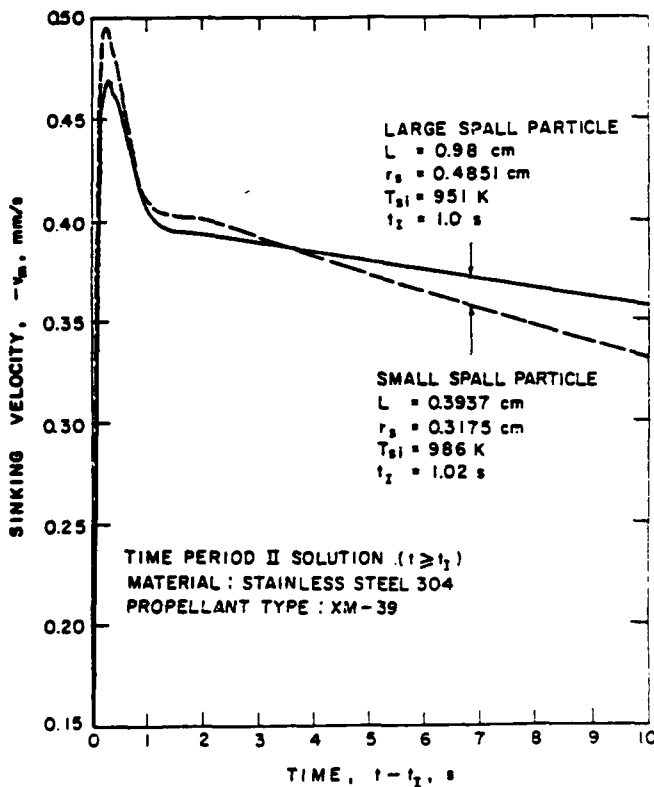


Fig. 15 Calculated Time Variations of Sinking Velocity

Figure 16 shows the comparison of calculated temperature-time traces at the base of the spall particle with experimental data. During the early phase, the base temperature for small particles is higher than that for large particles; the trend reverses at the later phase of Time Period II (when spall particles sink into the LOVA propellant). Calculated results are in good agreement with experimental data in terms of the trend mentioned above, as well as the magnitude and slope of these traces. It is interesting to note that the average temperature at the spall particle base drops continuously even after onset of sustained ignition; this is believed to be the result of incomplete combustion in the foam layer. Gaseous pyrolysis products in the bubbles take time to reach the fully reacted state. Heat release in the foam zone is sufficiently low to produce a relatively cool layer of foam material which reduces the energy of the spall particle. The above effect can be seen

from the plot of the calculated bulk temperatures of the gas and liquid phases in the foam layer (see Fig. 17). The temperatures of both phases are lower than the average temperature of the spall particle base. The calculated void fraction variations with respect to time is shown in Fig. 18. After the initial intensive heating in time period II, the void fraction reduces slightly with respect to time.

Comparisons of calculated temperature-time traces at the center of spall particles with experimental data is shown in Fig. 19. Agreement is quite reasonable, and the trend is identical to that described for spall particle base. Before completion of the computation of 10 s for the time period II, the center temperatures are always higher than those at the spall particle base.

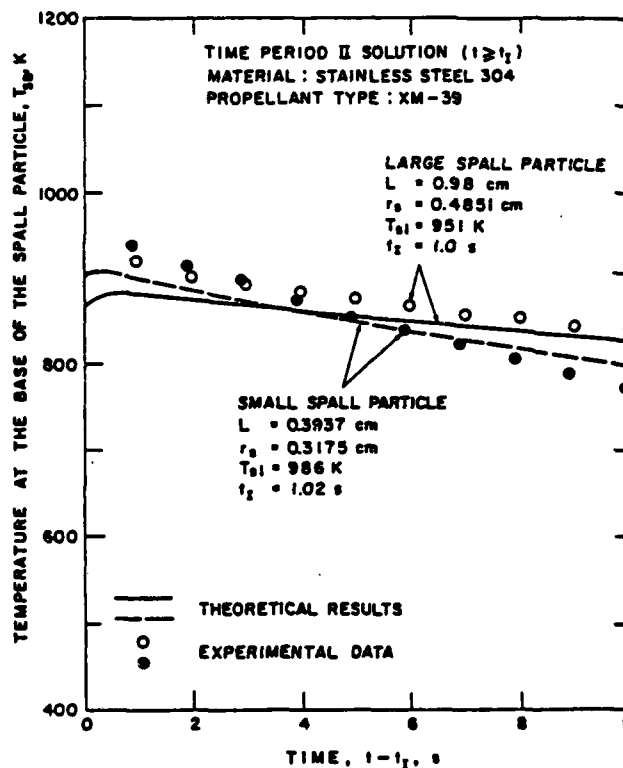


Fig. 16 Comparison of Calculated Temperature-Time Traces at the Base of the Spall Particle with Experimental Data

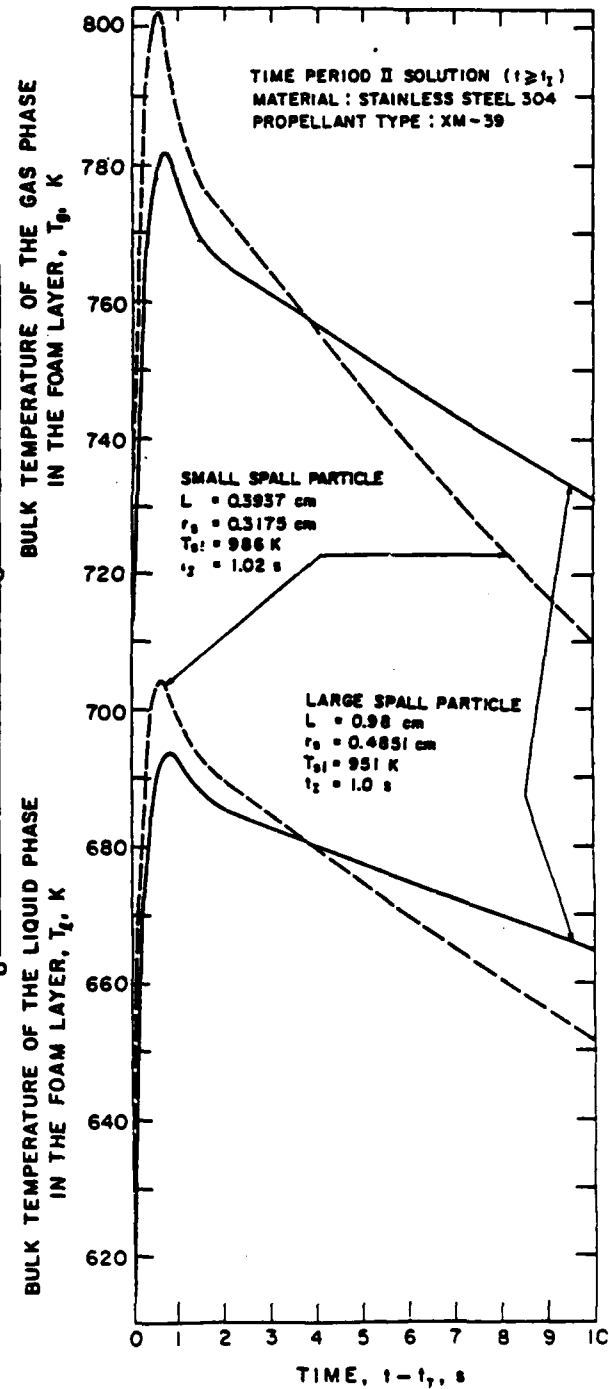


Fig. 17 Calculated Bulk Temperatures of the Gas and Liquid Phases in the Foam Layer

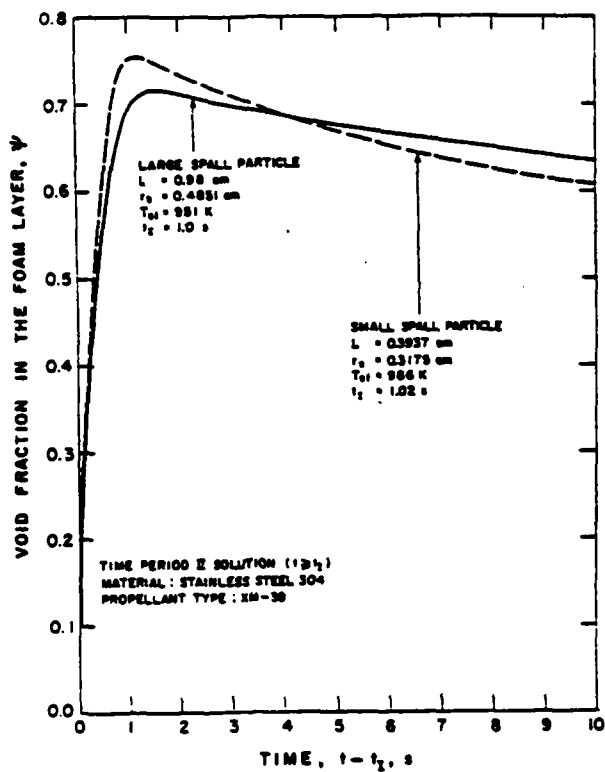


Fig. 18 Calculated Time Variations of Void Fractions in Foam Layers

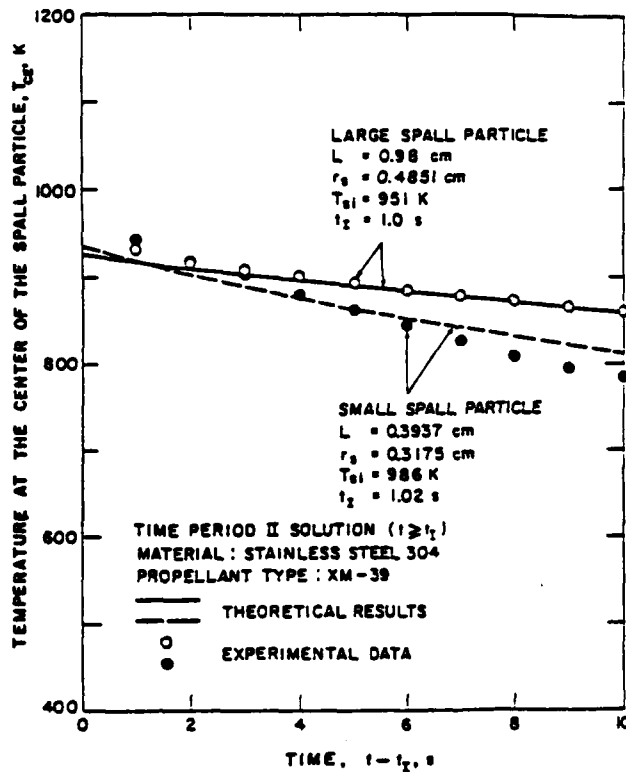


Fig. 19 Comparison of Calculated Temperature-Time Traces at the Center of Spall Particles with Experimental Data

Based upon these comparisons, it is quite obvious that the HFCI model is able to predict the quenched and ignited cases using different spall particle sizes. Also, by comparing results of the small particle ($L = 0.3937$ cm, $r_0 = 0.3175$ cm) at an initial temperature of 986 K with those for the same sized particle at 1000 K, one can observe the strong difference in solution from a quenched case to a runaway ignition. According to the test data of Miller and Cohen [13], the small particle can ignite the LOVA propellant at 986 K, which is in agreement with the prediction of ignition at 986 K.

SUMMARY AND CONCLUSIONS

- 1) The two-step chemical kinetic mechanism, proposed by Miller et al. [8], based upon DSC measurements, was incorporated into the theoretical model [12] for simulating hot fragment conductive ignition processes of LOVA propellants.
- 2) Calculated results compared well with experimental data in temperature-time traces of spall particle and propellant.
- 3) Reasonable agreement was achieved between theoretical prediction and experimental measurements in terms of the terminal position and particle trajectory of the quenched spall particle which is partially submerged in the LOVA propellant. The predicted trajectory of the spall particle also agrees quite well with measured data for ignited cases.
- 4) The controlling mechanism in the HFCI process is the competition between the rate of heat release from exothermic reactions introduced by the spall particle and the rate of heat loss to the surrounding.
- 5) The present two-step reaction model gave a reasonable numerical solution in HFCI simulation. However, a more complicated reaction model may be needed for various types of LOVA propellants. Also, additional heat transfer correlations in the foam zone of the pyrolysis product of various propellants should be developed for more accurate predictions of HFCI processes.
- 6) From HFCI point of view, it is highly desirable to have LOVA propellants with cool pyrolysis products in the foam layer which can effectively quench the hot spall particle. Also, it is desirable to have LOVA propellants which require extended distances for development of flames.

REFERENCES

1. Gol'dshleger, U. I., Barzykin, V. V., Ivleva, T. P., "Ignition of Condensed Explosives by a Hot Spherical Particle," Combustion, Explosion and Shock Waves, Vol. 9, No. 5, 1973, pp. 642-647.
2. Wise, S., Rocchio, J. J., and Reeves, H. F., "The Ignitability of Composite Nitramine Propellants," Proceedings of the 17th JANNAF Combustion Meeting, CPIA Publication 329, Vol. III, 1980, pp. 457-475.
3. Law, H. C. and Rocchio, J. J., "The Hot Fragment Conductive Ignition Test: A Means of Evaluating Propellant Vulnerability to Spall," Proceedings of the 18th JANNAF Combustion Meeting, CPIA Publication 347, Vol. II, 1981, pp. 321-334.
4. Wise, S. and Rocchio, J. J., "Binder Requirements for Low Vulnerability Propellants," Proceedings of the 18th JANNAF Combustion Meeting, CPIA Publication 347, Vol. II, 1981, pp. 305-320.
5. Kirshenbaum, M. S., Avrami, L., and Strauss, B., "Sensitivity Characterization of Low Vulnerability (LOVA) Propellants," U.S. Army ARRADCOM Technical Report, ARLCD-TR-83005, March 1983.
6. Cohen, A., Miller, M. S., and Holmes, H. E., "Hot Fragment Ignition of LOVA and NC Propellants," Proceedings of 22nd JANNAF Combustion Meeting, CPIA Publication 432, Vol. II, 1985, pp. 529-536.
7. Cohen, A., Miller, M. S., and Holmes, H. E., "Thermocouple Measurements During Fragment Ignition of Propellant Powders," Proceedings of 23rd JANNAF Combustion Meeting, CPIA Publication 457, Vol. II, 1986, pp. 337-342.
8. Miller, M. S., Kotlar, A. J., Cohen, A., Truong, K., Puckett, D. L., and Holmes, H. E., "Effective Ignition Kinetics for LOVA Propellant," Proceedings of 23rd JANNAF Combustion Meeting, CPIA Publication 457, Vol. II, 1986, pp. 55-62.
9. Vilyunov, V. N. and Kolchin, A. K., "Ignition of Condensed Explosives by Conductive Heat Transfer from Media with Poor Thermal Conductivity," Combustion, Explosion and Shock Waves, Vol. 2, No. 3, 1966, pp. 61-65.
10. Gol'dshleger, U. I., Pribytkova, K. V., and Barzykin, V. V., "Ignition of a Condensed Explosive by a Hot Object of Finite Dimensions," Combustion, Explosions, and Shock Waves, Vol. 9, No. 1, 1973, pp. 99-102.
11. Linan, A. and Kindelan, M., "Ignition of a Reactive Solid by an Inert Hot Spot," Combustion in Reactive Systems, edited by J. Ray Bowen et al., Progress in Astronautics and Aeronautics, Vol. 76, 1981, pp. 412-426.
12. Kuo, K. K., Hsieh, W. H., Hsieh, K. C., and Miller, M. S., "Simulation of Hot Fragment Conductive Ignition Processes of Solid Propellants," presented at the ASME Winter Annual Meeting, Paper No. 86-WA-HT-13, 1986.
13. Miller, M. S. and Cohen, A., private communication, Jan.-Aug. 1987.
14. Rohsenow, W. M. and Hartnett, J. P. (ed), Handbook of Heat Transfer, Chapter 13, 1973, pp. 13-65 and 13-66.
15. Boggs, T. L., "Thermal Behavior of RDX and HMX," Chapter 3 of Fundamentals of Solid-Propellant Combustion, edited by K. K. Kuo and M. Summerfield, Progress in Astronautics and Aeronautics, Vol. 90, Nov. 1984.
16. Robertson, A. J. B., "The Thermal Decomposition of Explosives, Part II: Cyclotrimethylenetrinitramine and Cyclotetramethylene-tetranitramine," Transactions of the Faraday Society, Vol. 45, 1949, p. 85.
17. Incropera, F. P. and DeWitt, D. P., Fundamentals of Heat Transfer, John Wiley & Sons, Inc., Appendix A, 1981, pp. 761-792.
18. Anon., Handbook of Chemistry and Physics, 63rd Edition, The Chemical Rubber Co., 1983.
19. Kuo, K. K., Principles of Combustion, Wiley, Chap. 9, 1986, pp. 668-673.

Attachment 3

**Validation of a Theoretical Model
for Hot Fragment Conductive Ignition Processes
of LOVA Propellants**

VALIDATION OF A THEORETICAL MODEL FOR HOT FRAGMENT
CONDUCTIVE IGNITION PROCESSES OF LOVA PROPELLANTS*

K. C. Hsieh[‡]
Sverdrup Technology, Inc.
Middleburg Heights, OH 44130

and

W. H. Hsieh,[†] K. K. Kuo^{*}
Department of Mechanical Engineering
The Pennsylvania State University
University Park, PA 16802

and

M. S. Miller[#]
U.S. Army Ballistic Research Laboratories
Aberdeen Proving Ground, MD 21005

A comprehensive theoretical model and an efficient numerical program have been developed to simulate the hot fragment conductive ignition (HFCI) processes for characterizing the degree of vulnerability of various gun propellants. In the formulation of the theoretical model, three sets of governing equations and their boundary conditions were derived for different regions consisting of the hot spall particle, the LOVA propellant, and the foam layer produced by liquefaction, pyrolysis, and decomposition of the propellant. In terms of chemical kinetic scheme, a two-step reaction model is proposed, based upon DSC experiments. The model contains an endothermic decomposition process followed by an exothermic pyrolysis of the propellant. Calculated results compared well with experimental data in temperature-time traces, trajectory of spall particles sinking into the LOVA propellant, and terminal position of the particle.

NOMENCLATURE

A	Arrhenius frequency factor of chemical reaction of melt or foam layer in Region 1, kg/m ³ -s	E_a	activation energy of chemical reaction of melt or foam layer, J/mole
A_1	Interface area between liquid melt and gas bubbles, m ²	ΔH_f°	heat of formation, J/kg
C_p	constant-pressure specific heat, J/kg-K	L_m	height of melt or foam layer in Region 1, m
C_s	specific heat of spall particle, J/kg-K	$\dot{m}_{\text{gnet},1}$	net rate of production of gaseous mass in Region 1 of foam layer, kg/s
D_b	averaged diameter of bubbles generated	Q_L	heat release due to exothermic reaction from liquid melt to gaseous products, J/kg
		Q_{melt}	heat of endothermic reaction from solid propellant to liquid melt, J/kg
		q_{gas}	heat flux transferred to gas phase from spall particle base, W/m ²
		$q_{\text{gas-liq}}$	heat flux transferred to liquid phase from gas phase through interfaces, W/m ²
		q_{liq}	heat flux transferred to liquid phase from spall particle base, W/m ²
		$q_{\text{liq-solid}}$	heat flux transferred to propellant surface from foam layer, W/m ²

*This work was performed under contract DAAK11-83-C-0015, sponsored by the Applied Ballistic Branch of the Ballistic Research Laboratories under the support and encouragement of Dr. Joseph J. Rocchio and Mr. Norman Gerri. The authors would like to thank Dr. A. Cohen for his input in supplying HFCI data.
 ‡Research Engineer
[†]Research Associate
 *Distinguished Alumni Professor of Mechanical Engineering
[#]Research Physicist

q_{pr}^*	heat flux transferred to LOVA propellant from melt or foam layer in Region 1, W/m^2
q_{spall}^*	heat flux at base of spall particle, W/m^2
R_u	Universal gas constant, 8314.4 J/kg-mole K
r_s	radius of spall particle, m
$T_b (=T_{\text{sat}})$	boiling temperature of liquid melt, K
T_g	gas temperature, K
\bar{T}_m	bulk temperature of melt or foam layer, K
T_{melt}	melting temperature of LOVA propellant, K
T_p	temperature of LOVA propellant, K
T_{ps}	average surface temperature of LOVA propellant exposed to air, K
T_s	temperature of spall particle, K
v_{lr}	radial velocity of melt or foam layer in Region 1, m/s
v_s or $-v_m$	sinking velocity of spall particle, m/s
z	axial distance above base of spall particle, m
z^*	axial distance below instantaneous surface of propellant under foam layer, m
<u>Greek Symbols</u>	
α	thermal diffusivity, m^2/s
δ_{pr}	thermal penetration depth from propellant surface, m
λ	thermal conductivity, W/m-K
ρ	density, kg/m^3
ψ	average porosity (void fraction) of foam layer in Region 1
μ	dynamic viscosity, kg/m-s
<u>Subscripts</u>	
g	gas-phase
i	initial condition
l	liquid-phase
$melt$	melt liquid melt
pr or p	propellant
$-$	room condition
1	Region 1 of foam layer
<u>Superscript</u>	
*	$T^* = T - T_{\text{ref}}$

INTRODUCTION

In the selection of low vulnerability ammunition (LOVA) propellants, go/no-go ignition tests with hot metallic elements are often conducted to simulate hot fragment conductive ignition (HFCI) processes. These hot fragments can be considered as those generated from the penetration of armor plates by shaped charge jets or kinetic energy penetrators. One way to negate the threat of propellant ignition by hot spalls is to use a propellant which is resistant to conductive ignition. A number of investigations on this subject have been conducted, both theoretically and experimentally, in recent years [1-12]. Since a review of pertinent work is given in the paper by Kuo et al. [12], detailed reviews are omitted here. Only major findings of HFCI processes are listed below.

- Binders of nitramine composite propellants were found to have a strong effect on conductive ignition. Some binders can act as fire retardant coolants.
- The relative susceptibility of LOVA propellants to ignition by spall particles can be determined from ignition map based upon the plot of the initial temperature versus weight of the spall fragment.
- The contact resistant between hot particle and propellant significantly affects the delay time for onset of runaway ignition.
- Binders which endothermically decompose under acid catalysis are more desirable for LOVA propellant binder ingredients.
- The ignition temperatures of LOVA propellants are similar to their nitramine fillers.
- For certain LOVA propellants, liquefaction and bubble formation were observed during conductive heating. This suggests that the thermal insulation properties of binder products may be important in the determination of ignition sensitivities of LOVA propellants.
- Based upon surface thermocouple measurements during HFCI tests, the initial condensed phase reactions are endothermic. The endothermicity of these reactions showed good correlation with propellant sensitivity for thermal ignition.
- The minimum spall particle temperature (for a fixed spall particle weight) depends strongly on binder composition.
- Chemical reactions leading to ignition of certain LOVA propellants during HFCI experiments can be idealized as a two-step sequence of global reactions in which an endothermic reaction is followed by an exothermic reaction.

Several attempts were made to model the hot fragment conductive ignition processes [9-11]; however, these models have serious limitations in simulating actual HFCI processes. The model proposed in Ref. 9 is strictly one-dimensional, and allows no space for the products in the gas or liquid phases to exit at the interface between

propellant samples and hot inert fragments. The model proposed in Ref. 10 requires no depletion of propellant when the hot fragment penetrates the combustible material. Also, no surface reaction is allowed in the model. An interesting theoretical analysis of the ignition of reactive solids by direct contact with a hot inert body was performed by Linan and Kindelan [11]. Their analysis considered both cylindrical and spherical geometries. Asymptotic solutions for large activation energies were obtained. The solution indicated the existence of an ignition boundary beyond which runaway ignition occurred. Although the theoretical results indicated the correct trend in terms of inert particle initial temperature and particle size, their solutions were not compared with any experimental data. Furthermore, the assumption of high activation energies are invalid for various LOVA propellants. There was no provision for the development of a foam layer at the interface region between hot fragment and propellant.

A comprehensive theoretical model was recently developed by Kuo et al. [12] to describe the heat transfer processes in hot fragment and solid propellant, as well as the development of a foam and/or melt layer which has been experimentally observed at the interface zone between solid propellant surface and hot spall particle. In this model, the liquefaction, surface reaction, and gas-phase reactions in the foam layer were considered. The effect of binder composition can also be studied by using measured kinetic data from separate DSC experiments for LOVA propellants with various binders. Thus, the ability of resisting conductive ignition of new propellant formulations can be evaluated for achieving reduced system vulnerability.

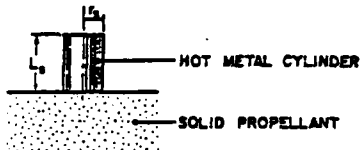
Although the model presented in Ref. 12 includes both reacting and non-reacting cases, only the non-reacting part of the model was verified by ice-melting and evaporation experiments. The main objective of this paper is to verify the chemically reacting part of the model. The latest reaction mechanism and data obtained by Miller et al. [8] have been incorporated into the model. Numerical simulation of HFCI processes of certain LOVA propellants have been conducted, and the results are compared with the data obtained by Miller and Cohen [13] for model validation.

METHOD OF APPROACH

Description of Physical Events

In an HFCI experiment, a hot metal particle comes into contact with a cold propellant at Time 0. In the early phase of the process (Time Period I), heat is conducted from the hot particle to the propellant without any phase change or pyrolysis (see Fig. 1). As time progresses, the temperature of the propellant increases and that of the particle decreases. Following a period of inert heating, the propellant starts to decompose, melt, and/or gasify (Time Period II). During Time Period II, a foam or melt layer usually exists near the interface region between the hot fragment and solid propellant. Since the density of the metal particle is much higher than the density of the decomposed propellant, it displaces the decomposed propellant and becomes imbedded in (sinks into) the propellant, as shown in Fig. 1.

TIME PERIOD I (BEFORE THE FORMATION OF A MELT LAYER)



TIME PERIOD II (AFTER THE FORMATION OF A MELT LAYER)

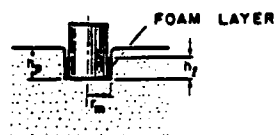


Fig. 1 Physical Event of Hot Fragment Conductive Ignition (HFCI) Processes Represented by Various Cases in Two Different Time Periods

The decomposed species can further react exothermically in the gas phase, foam layer, and/or condensed (solid, liquid) phase to cause ignition. If the rate of heat release in the foam layer is lower than that of the heat loss to the surrounding and ambient materials, the spall particle will be quenched without introducing ignition. Self-sustained ignition will occur only if the rate of heat generated by the exothermic reactions exceeds the rate of heat loss. In view of the importance of chemical reactions in the foam layer and surface region of solid propellants, effective kinetic mechanisms must be determined and accurate kinetic data obtained. This information and data are then fed into the theoretical model for realistic simulations.

Determination of Effective Ignition Kinetics for the Sample Propellant

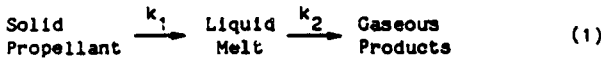
Efforts to identify elementary reactions and measure their reaction rates were ruled out as probably infeasible from a technical standpoint, and certainly inappropriate to the scope of the modeling effort and the resources available for numerical computations.

Since the main interest in these reactions is the energy source (or sink) terms in heat transfer equations, Differential Scanning Calorimetry (DSC) was chosen as a suitable technique for measuring reactive heat exchange of decomposing propellant in contact with a metal surface. Operated in ramp mode, this instrument can increase the sample temperature linearly with time at rates up to 100°C/min. Although ignition by hot fragments could involve much higher instantaneous heating rates, these high rates cannot be sustained for any appreciable time due to conductive and convective loss mechanisms. Because observations of hot fragment ignition under controlled conditions indicate that 5 seconds or more are required to establish ignition, the 100°C/minute limitation may not be too restrictive.

The propellant used in this study has a unimodal distribution of RDX particle sizes (about 5 micron average). The DSC test samples were microtomed to a uniform thickness of about 0.4 mm with mass of about 1 mg ($\pm 5\%$) and placed in covered and crimped pans perforated in four places

with a straight pin. The pan perforations allow for pressure release, while retaining the bulk of any decomposition heat resulting from reactions occurring at or very near the propellant surface. Thus, the technique does not distinguish between energetic reactions in the solid, liquid, or gas phase; the goal is only to measure net "localized" energy release (or absorption).

DSC thermograms for the test propellant used here typically exhibited an endotherm of about 20 cal/g, starting at about 185°C and followed by an exotherm of about 300 cal/g which peaks at about 260°C. At the onset of this study, the intention was to treat the exotherm as a simple global reaction and the endotherm as a phase change. Ultimately, both were described as separate single reactions, each with its own set of kinetic parameters. A detailed analysis was reported in Ref. 8. The reaction mechanism proposed by Miller et al. [8] is a two-step sequence of global reactions represented by the following equations.



where the specific reaction rate constants k_1 and k_2 can be expressed in the Arrhenius form

$$k_1 = A_1 \exp\left(-\frac{E_1}{R_u T}\right) \quad (2)$$

$$k_2 = A_2 \exp\left(-\frac{E_2}{R_u T}\right) \quad (3)$$

In the curve-fitting process, Miller et al. found that the Arrhenius coefficient, A_1 , can be satisfactorily represented by a constant, and A_2 can either be approximated by constants or expressed as a power law of heating rate (r) in their DSC experiments, i.e.,

$$A_2 = \text{constant} \quad \text{or} \quad A_2 = a_2 r^{b_2} \quad (4)$$

A typical comparison of the data with the fitted curve is shown in Fig. 2. The constant A_2 fitted curve is slightly different from the curve shown in Fig. 2, and is equally acceptable for numerical simulation of HFCI processes. Considering the enormous simplification of the actual chemistry afforded by the irreversible two-step idealization, the quality of representation is quite good. Good representations of the data are found for a wide range of heating rates and inert gas purge flow rates. The DSC data for the sample propellant is summarized in Table 1.

where Q_1 and Q_2 are the specific heat release for endothermic and exothermic reactions.

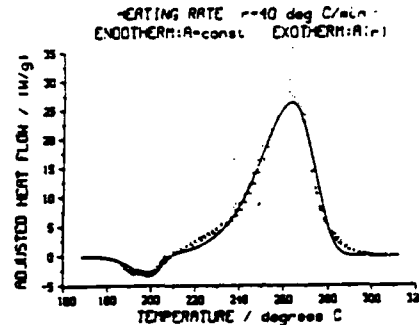


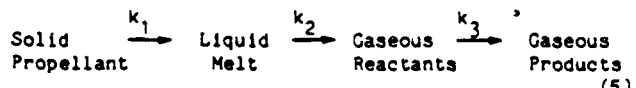
Fig. 2 Comparison of Composite DSC Thermograms (Points) to Fitted Curve Using Heating Rate Dependent A_2 Factor

Incorporation of Two-Step Global Reaction Kinetics into the HFCI Theoretical Model

Before describing the specific steps taken in incorporating the two-step global reaction kinetics into the HFCI model, it is useful to give a brief summary of the model structure. As described in Ref. 12, the physical model is divided into various regions (see Fig. 3): 1) spall particle region; 2) foam layer region 1; 3) foam layer region 2; and 4) LOVA propellant region. Each region has its own governing equations and boundary conditions.

In order to incorporate the two-step global kinetics into the HFCI model, the main modification is concentrated on the formulation of foam layer Region 1, which is the area controlling the onset of ignition.

Due to the limited kinetic data resources available for LOVA propellants at the time the HFCI model was initially formulated, a more general consecutive three-step reaction from solid propellant to gaseous products was adopted, i.e.,



With the consideration of the third reaction, the heat released in the gas-phase reaction could increase the temperature of the gases in the foam layer. However, from the DSC experiments [8], a two-step global reaction was proposed, as discussed above.

Table 1. Kinetic Constants Determined from DSC

A_1 (s^{-1})	A_2 (s^{-1})	E_1 (Kcal/mol)	E_2 (Kcal/mol)	a_2 (s^{b_2-1}/k^{b_2})	b_2 (--)	Q_1 (cal/g)	Q_2 (cal/g)
1.31×10^{31}	1.98×10^{14}	69.4	38.2	----	----	-21.1	297
$\pm 0.57 \times 10^{31}$	$\pm 0.80 \times 10^{14}$	± 0.4	± 0.4	----	----	± 5.6	± 26
----	----	----	47.2	7.79×10^{17}	-0.516	----	297
----	----	----	± 0.4	$\pm 2.89 \times 10^{17}$	± 0.014	----	± 26

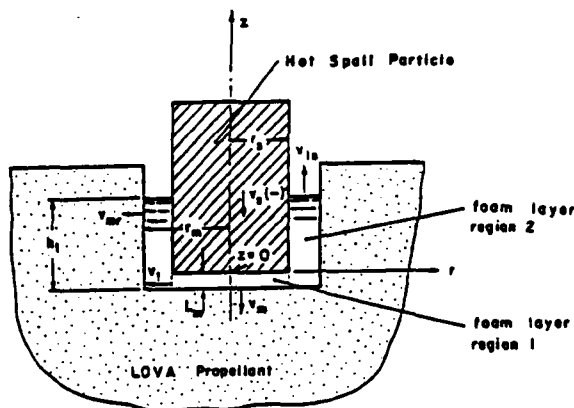


Fig. 3 Schematic Diagram of the Model

Based upon two-step reaction kinetics and energy flux balance shown in Fig. 4a, the equation describing the rate of change of gas-phase temperature can be derived as follows.

$$\begin{aligned} \psi \pi r_s^2 L_m \rho_p C_p \frac{dT_g}{dt} &= \dot{q}_{\text{gas}}'' \psi \pi r_s^2 - \dot{q}_{\text{gas-liquid}}'' A_1 \\ &+ \dot{m}_{g_{\text{net}}} [(C_{pL} T_i'' + \Delta H_{f,i}^0) - (C_{pg} T_g'' + n \Delta H_{f,g}^0)] \\ &- RT_{\text{ref}} \rho_g v_{irr}^2 \pi r_s^2 L_m \psi f \end{aligned} \quad (6)$$

where n can be considered as the combustion efficiency in the foam layer.

For the liquid phase, the balance of energy fluxes are given in Fig. 4b, and the equation of liquid-phase temperature can be written as

$$\begin{aligned} (1-\psi) \pi r_s^2 L_m \rho_L C_v \frac{dT_L}{dt} &= v_m \rho_p \pi r_s^2 C_{pL} (T_L - T_{ps}) \\ &+ \dot{q}_{\text{liq}}'' (1-\psi) \pi r_s^2 - \dot{q}_{\text{liq-solid}}'' \pi r_s^2 + \dot{q}_{\text{gas-liquid}}'' A_1 \end{aligned} \quad (7)$$

From the mass balances for both gas and liquid phases, the following equations can be obtained after certain manipulations.

$$\begin{aligned} \frac{D\psi}{dt} &= \frac{(1-\psi)R}{(1-\psi+f\psi) \pi r_s^2 L_m C_p P} [\dot{q}_{\text{gas}}'' \psi \pi r_s^2 - \dot{q}_{\text{gas-liquid}}'' A_1 \\ &+ RT_{\text{ref}} \rho_g v_{irr}^2 \pi r_s^2 L_m \psi f + \dot{m}_{g_{\text{net}}} Q_L] \\ &+ \frac{(1-\psi) \rho_L + f \psi \rho_g}{(1-\psi+f\psi) \rho_g} \frac{\dot{m}_{g_{\text{net}}}'}{L_m \pi r_s^2 \rho_L} + \frac{f \psi \rho_{pr}}{(1-\psi+f\psi) L_m \rho_L} v_m \end{aligned} \quad (8)$$

where

$$Q_L = (C_{pL} T_i'' + \Delta H_{f,i}^0) - (C_{pg} T_g'' + n \Delta H_{f,g}^0) \quad (9)$$

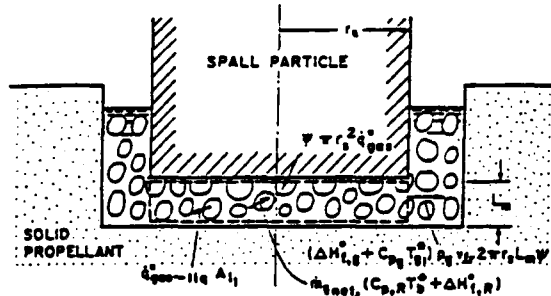


Fig. 4a Energy Fluxes Associated with the Gas Phase in Region 1 (The Thickness of Foam Layer is Highly Exaggerated)

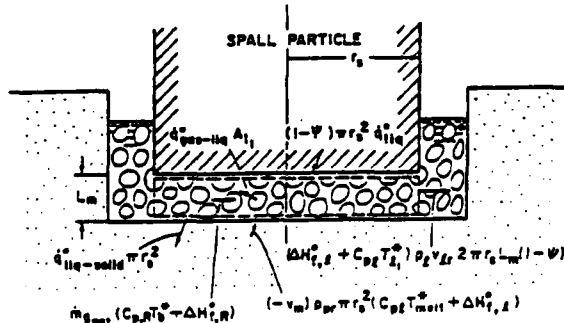


Fig. 4b Energy Fluxes Associated with the Liquid Phase in Region 1 (Thickness of Foam Layer is Highly Exaggerated)

$$v_{irr} = \frac{R}{2\pi L_m C_p P} [\dot{q}_{\text{gas}}'' \psi \pi r_s^2 - \dot{q}_{\text{gas-liquid}}'' A_1 + \dot{m}_{g_{\text{net}}} Q_L] \quad (10)$$

$$+ \frac{\rho_L - \rho_g}{\rho_L \rho_g} \frac{\dot{m}_{g_{\text{net}}}'}{2\pi L_m r_s} - \frac{r_s \rho_{pr}}{2L_m \rho_L} v_m \} / [(1-\psi+f\psi) - \frac{RT_{\text{ref}} \psi f}{C_p \rho_g g}] \quad (10)$$

In addition to the above four governing equations (three ODES, one algebraic equation), the perfect gas law is used to evaluate gas density. The energy flux balance at the interface between liquid melt and propellant surface can be given as

$$\dot{q}_{\text{liq-solid}}'' = \dot{q}_{\text{pr}}'' + Q_{\text{melt}} (v_s) \rho_{pr} \quad (11)$$

where the heat of reaction Q_{melt} is defined as

$$Q_{\text{melt}} = (\Delta H_{f,i}^0 + C_{pL} T_i'') - (\Delta H_{f,pr}^0 + C_{pr} T_{\text{melt}}'') \quad (12)$$

The endothermic reaction from solid propellant to liquid melt absorbs heat from liquid phase via the last term in Eq. (11). The liquid phase is heated by energy transferred from gas phase through bubble interfaces in the foam layer. This mechanism is modeled as $\dot{q}_{\text{gas-liquid}}'' A_1$ in Eq. (7). The exothermic reaction (from liquid melt to gaseous products) releases heat to elevate gas-phase temperature via the source term associated with $\dot{m}_{g_{\text{net}}}'$ in Eq. (6).

In order to close the above system, the parameter f , which relates v_{lpr} (the radial velocity of the liquid phase at the lateral surface of foam layer in region 1) and v_{erg} ($v_{erg} = f v_{lpr}$), was expressed as

$$f = C \left[\frac{m_{g_{net}}}{\pi r_s^2 (-v_m + v)} \right]^n \quad (13)$$

The above equation is based upon various limiting conditions given below.

Case 1: $f = 0$, when the volumetric gas generation rate is much smaller than the volumetric regression rate of the melt layer, i.e.

$$\pi r_s^2 (-v_m) \gg m_{g_{net}} / \rho_g$$

$$\text{Case 2: } f = 1, \text{ when } \pi r_s^2 (-v_m) = m_{g_{net}} / \rho_g$$

$$\text{Case 3: } f \gg 1, \text{ when } \pi r_s^2 (-v_m) \ll m_{g_{net}} / \rho_g$$

To avoid singularity at the onset of melting or liquefaction of LOVA propellants, a small parameter, ϵ , in the order of 0.0001 is inserted in the denominator of Eq. (13). The coefficient C and exponent n are taken to be the unit in the HFCI simulation.

The foam layer region 1 thus contains six major unknown parameters (ψ , T_g , T_l , v_{lpr} , f , ρ_g , solved from Eqs. (6), (7), (8), (10), and (13), and the perfect gas law.

Empirical Correlations and Input Parameters

The exothermic chemical reaction plays an important role in the HFCI process, since high rates of heat release could lead to runaway ignition. Therefore, it is necessary to acquire an appropriate correlation for the chemical reaction rate. The kinetic data used in numerical calculations was obtained from Miller's DSC experiments [8]. The rate of production of gaseous mass in Region 1 of the foam layer is expressed as

$$\dot{m}_{g_{net}} = c_L \pi r_s^2 (1-\psi) \rho_l A_2 \exp\left(-\frac{E_a}{R T}\right) \quad (14)$$

where A_2 is the same as A_2 given in Table 1, and c_L is a constant smaller than 1. The temperature distribution in the liquid phase of the foam layer is not strictly uniform. Most of the liquid is at a temperature lower than the liquid surface temperature of bubbles. This can influence the value of c_L . Also, the reacting surface layer of bubbles could be a small fraction of the liquid in the foam layer. Furthermore, the Arrhenius law is highly nonlinear. All of these factors could influence the effective mass generation rate. In the present lumped parameter analysis for the foam layer, the selected value of c_L in HFCI simulation is 0.02 for all cases studied.

In addition to the kinetic correlation, suitable empirical correlations for heat fluxes (e.g., $q_{liq-solid}$, q_{liq} , q_{gas} , and $q_{gas-liq}$) are also needed to properly predict heat transfer rates and system eigenvalues, that is, the sinking velocity (v_s or $-v_m$) and the propellant surface temperature (T_{ps}). The heat transfer coefficients for $q_{liq-solid}$, q_{liq} , and q_{gas} are adopted in the combined form of forced convection and conduction. In the early stage of time period II (described in physical events) or before propellant ignition, the radial velocity in Region 1 of the foam layer can be quite high. Therefore, the forced convection effect dominates heat transfer among the spall particle, foam layer, and propellant. However, in the quenched cases, the conduction heat transfer is not the main mechanism during most of time period II. Some of the heat transfer correlations used are given in Ref. 12. In consideration of various forms of heat transfer correlation, it is noted that the heat transfer measurements available for foam layers are very scarce. In fact, heat transfer rates of foams generated by liquefaction and pyrolysis of solid propellant are completely unavailable. This is an area requiring further research. The heat fluxes mentioned above can be expressed as follows:

$$q_{gas} = h_{conv} (\bar{T}_{SB} - T_g) \quad (15)$$

$$q_{liq} = h_{conv} (\bar{T}_{SB} - T_l) \quad (16)$$

$$q_{liq-solid} = h_{conv} (\bar{T}_m - T_{ps}) \quad (17)$$

$$\text{where } \bar{T}_m = \frac{(1-\psi) \rho_l C_p T_l + \psi \rho_g C_p T_g}{(1-\psi) \rho_l C_p + \psi \rho_g C_p} \quad (18)$$

The heat flux at propellant surface (q_{pr}) is calculated from the following equation, as described in Ref. 12.

$$\frac{d\delta_{pr}}{dt} = 3\lambda_p \left(\frac{T_{ps} - T_{pi}}{\delta_{pr}} \right) \quad (19)$$

where the coefficient $3\lambda_p$ results from a third-order polynomial approximation for the temperature profile. The time variation of the thermal wave penetration depth, δ_{pr} , is determined from

$$\frac{d\delta_{pr}^2}{dt} = 24 \alpha_{pr} + 8 v_m \delta_{pr} - \frac{2\delta_{pr}^2}{(T_{ps} - T_{pi})} \frac{dT_{ps}}{dt} \quad (20)$$

After δ_{pr} is solved from Eq. (20), the propellant surface temperature can be determined from Eq. (11) through the use of Eqs. (17) and (19).

The sinking velocity can then be calculated by

$$v_s = \left(\frac{q_{liq-solid}}{\rho_{pr} Q_{melt}} \right)^{1/2} \quad (21)$$

In addition to the above correlations and data provided in Table 1, a set of input data was prepared and listed in Table 2. The thermodynamic and transport properties were obtained from open literature [14-19].

Table 2. Input Data Used in the HFCI Simulation

Region	Parameter	Value	Unit
Spall	r_s	0.3175×10^{-2} or 0.4851×10^{-2}	m
	L_s	0.3937×10^{-2} or 0.98×10^{-2}	m
Particle	λ_s	16.246	W/m-K
	C_s	5.02×10^2	J/kg-K
	ρ_s	8.0×10^3	kg/m ³
	λ_1	2.094×10^{-1}	W/m-K
Foam	ρ_f	1.60×10^3	kg/m ³
	C_f	1.465×10^3	J/kg-K
	μ_f	0.832×10^{-3}	kg/m-s
	$E_{a,fg}$	1.597×10^5	J/mole
Layer	A_2	1.98×10^{14}	1/s
	$\Delta H^0_{f,l}$	-6.695×10^5	J/kg
	$\Delta H^0_{f,g}$	-1.912×10^6	J/kg
	λ_g	36.29×10^{-3}	W/m-K
LOVA	C_{pg}	1.465×10^3	J/kg-K
	η	0.80	----
Propellant	C_{pr}	3.852×10^2 + $2.598 * T(K)$	J/kg-K
	ρ_{pr}	1.678×10^3	kg/m ³
	λ_{pr}	2.094×10^{-1}	W/m-K
	$\Delta H^0_{f,pr}$	-7.579×10^5	J/kg
Propellant	$E_{a,pt}$	2.9×10^5	J/mole
	A_1	1.31×10^{31}	1/s

Overall Structure of Theoretical Model

The theoretical model consists of governing equations and their associated initial and boundary conditions for the hot particle, the propellant, and the foam layer. Governing equations for the hot particle and the propellant are transient heat conduction equations written in two-dimensional cylindrical form. These equations were recast into ordinary differential equations by integral methods. In these two regions, instantaneous temperature distributions are solved from the governing equations coupled to the foam layer through flux balances at their boundaries (see Fig. 5). The solution of major unknowns in the foam layer is also delineated in the same figure.

DISCUSSION OF RESULTS

In the following, one set of HFCI simulation results is compared with experimental results, and two sets of parametric runs are presented and

discussed in detail. To study the initial temperature effect of the spall particle, two different temperatures (768 and 1000 K) were considered for the same spall particle size ($L_s = 0.3937$ cm, $R_s = 0.3175$ cm). The calculated results from the case with an initial temperature of 768 K are compared with experimental data obtained by Miller and Cohen [13]. The third set of results was obtained for studying the mass effect on the HFCI process using a large spall particle ($L_s = 0.98$ cm, $r_s = 0.4851$ cm).

Figure 6 shows a set of propellant subsurface temperature profiles at different times before the spall particle begins to sink into the LOVA propellant. As one can see from the temperature profile variation, the thermal wave penetration depth becomes deeper as time increases. However, the surface temperature remains approximately at the 735 K range.

The axial temperature variation at the center line of the spall particle is shown in Fig. 7 for different times in time period I. This figure indicates the decay of maximum temperature at a distance far from the spall particle base. The temperature gradient at the base of the spall drops from a large value upon initial contact, to a much lower level at 1.3 s. At the end of time period I, the axial temperature distribution becomes quite uniform.

In time period II, the spall particle sinks into the LOVA propellant. The calculated sinking distance versus time is compared with measured data in Fig. 8. The calculated sinking velocity is also shown in this figure. Note that the sinking velocity (the slope of the curve) increases rapidly at the very beginning, starts to decrease at $t = 0.75$ s, and approaches zero at the end of the calculation ($t=34$ s). The final calculated sinking distance is about 15% larger than the measured one. This discrepancy could be caused by errors in experimental measurement as well as any inappropriate of heat transfer correlation used in the foam layer of the theoretical model. In general, this comparison shows a reasonable agreement between calculated and measured results.

The calculated time variation of the void fraction in the foam layer [$\psi(t)$] is shown in Fig. 9. When the spall particle starts to sink into the LOVA propellant, ψ increases drastically due to intensive heating, and then slows down significantly as time increases at the end of computation; only 72% of the space in the foam layer is occupied by the gas. The calculated time variations of center and base temperatures of the spall particle are compared with thermocouple measurements at corresponding locations in Figs. 10 and 11, respectively. Comparison of the predicted base temperature is better than comparison of the predicted center temperature with experimental data. Both of these temperatures decline monotonically as the particle begins to sink into the LOVA propellant and approach asymptotic levels near the end of computation.

The calculated time variation of the instantaneous subsurface temperature of the first thermocouple location (6 mm below the initial propellant surface) compares well with measured data, as shown in Fig. 12. Like the measured data, the calculated subsurface temperature at the second thermocouple location (12 mm below the surface) shows no response at the end of calculation ($t=34$ s).

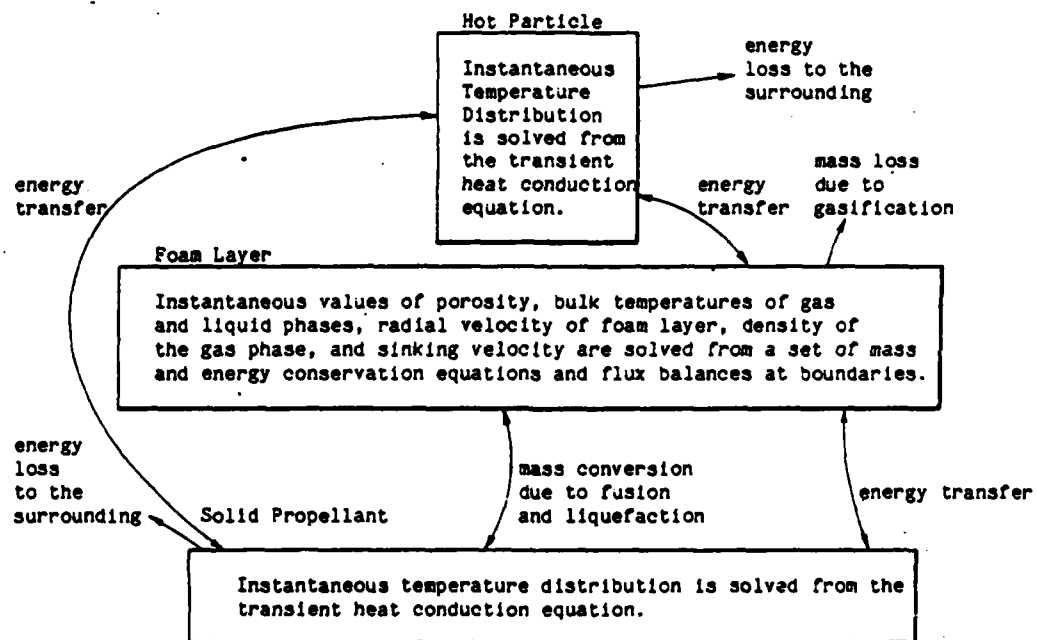


Figure 5. Block Diagram Showing the Mathematical Formulation and Coupling Relationship Between Hot Particle, Foam Layer, and Solid Propellant

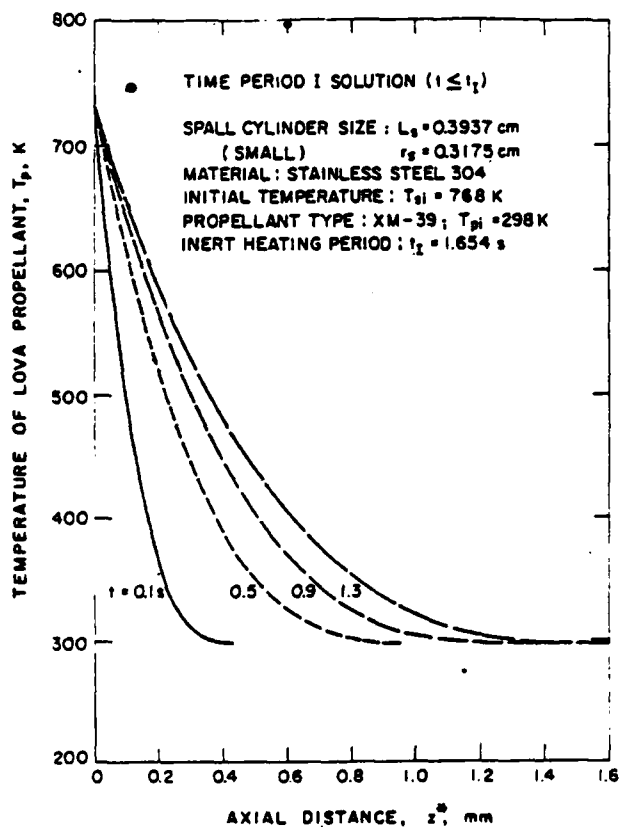


Fig. 6 Calculated Temperature Distributions in the LOVA Propellant at Various Times

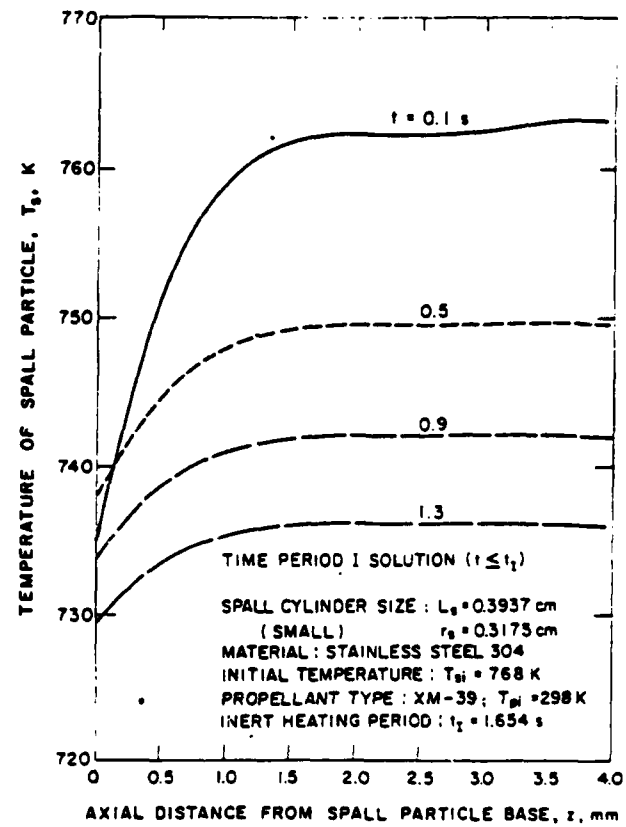


Fig. 7 Calculated Axial Temperature Distributions Along the Centerline of the Spall Particle at Various Times

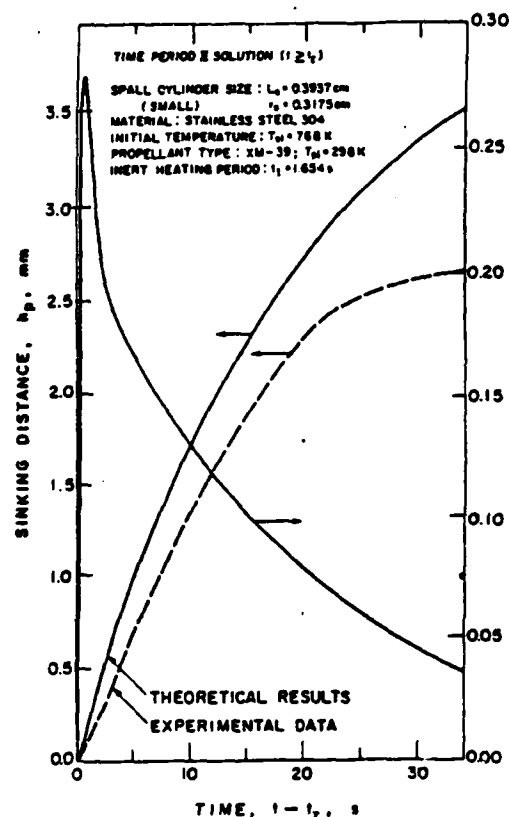


Fig. 8 Comparison of Calculated Time Variations of Sinking Distances with Experimental Data and Calculated Time Variation of Sinking Velocity of the Spall Particle

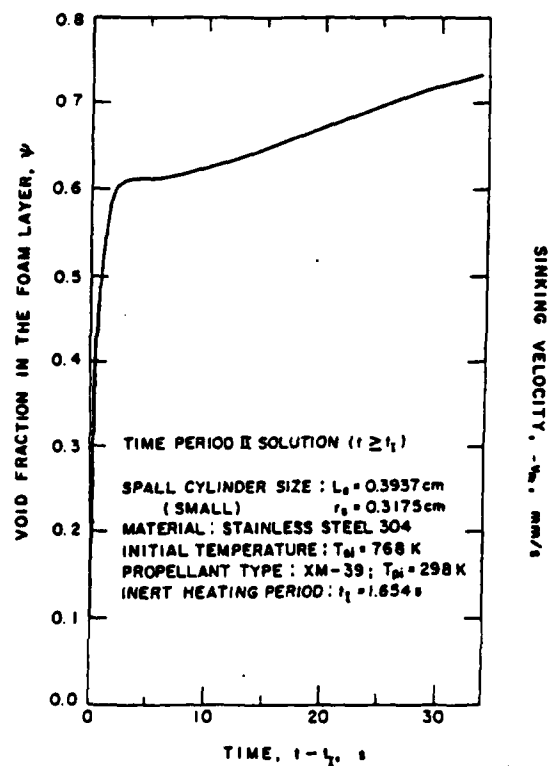


Fig. 9 Calculated Time Variation of the Void Fraction in the Foam Layer

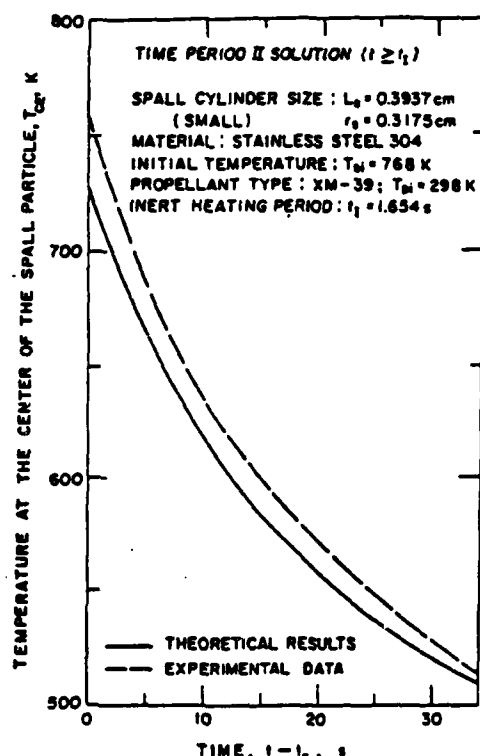


Fig. 10 Comparison of Calculated Temperature-Time Trace at the Center of the Spall Particle with Experimental Data

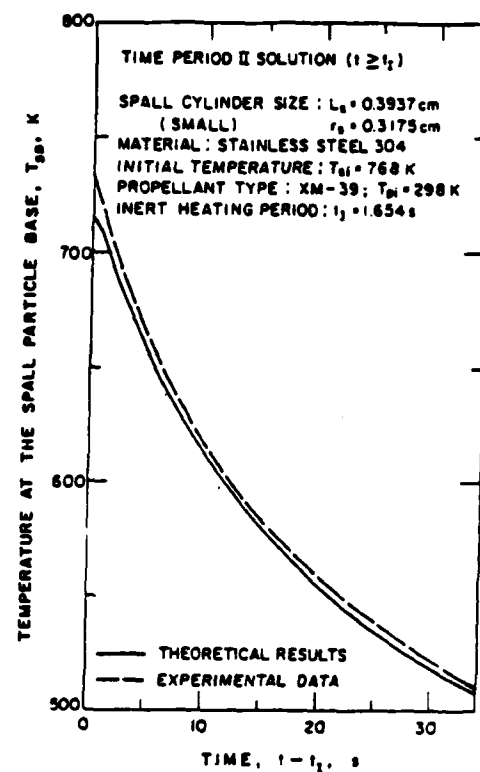


Fig. 11 Comparison of the Temperature-Time Trace at the Bottom Surface of the Spall Particle with Experimental Data

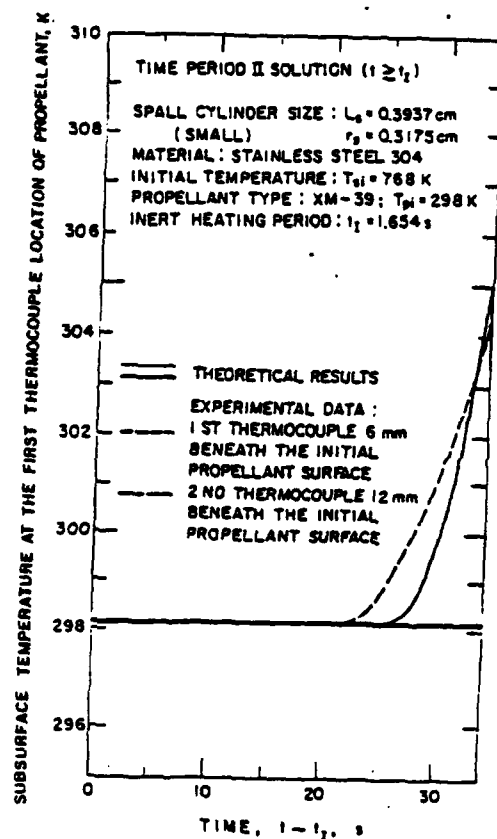


Fig. 12 Comparisons of Predicted Temperature-Time Traces at the First and Second Thermocouple Locations (6 and 12 mm Below the Propellant Surface) with Experimental Data

Comparison of bulk temperatures of gas and liquid phases in the foam layer is shown in Fig. 13. During time period II, the gas-phase temperature is always higher than that of the liquid. The temperature difference decreases monotonically and reaches a small difference near the end of computation.

In addition to the quenched case discussed above, two separate HFCI tests were conducted by Miller and Cohen [13], using different spall particle sizes and initial temperature. The small cylindrical particle has a radius of 0.3175 cm and a length of .3937 cm, with an initial temperature of 986 K at the time of contact with the LOVA propellant. The large cylindrical particle has a radius of 0.4851 cm and a length of 0.98 cm, with an initial temperature of 951 K at the time of contact with the LOVA propellant. In both cases, the propellant ignited. The pyrolyzed gases are not luminous near the base region of the spall particle. The observed luminous flame is above the initial propellant surface. The flame widens abruptly at 5.2 and 1.2 s, corresponding to the small and large particles, respectively. Widening of the flame could be considered as onset of sustained ignition from the experimental point of view.

To validate the theoretical model with the ignited cases, both tests were simulated. Results are discussed below. Figure 14 shows the comparison of calculated trajectories of spall particles with experimental data. The small

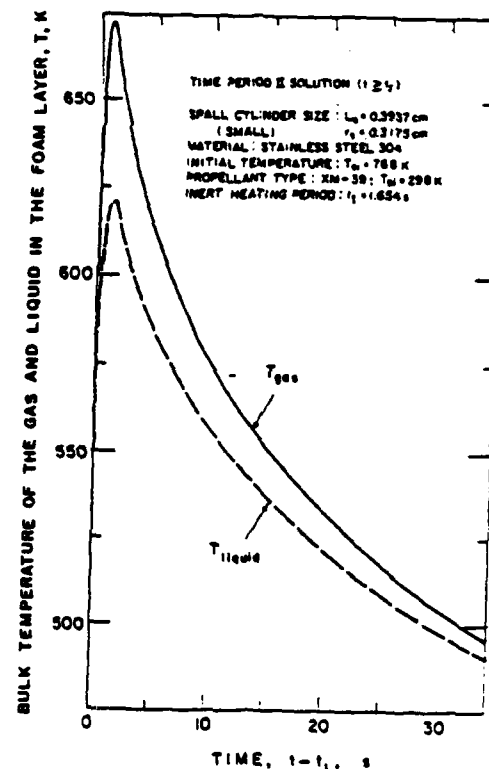


Fig. 13 Calculated Temperature-Time Traces of Gas and Liquid Phases in the Foam Layer

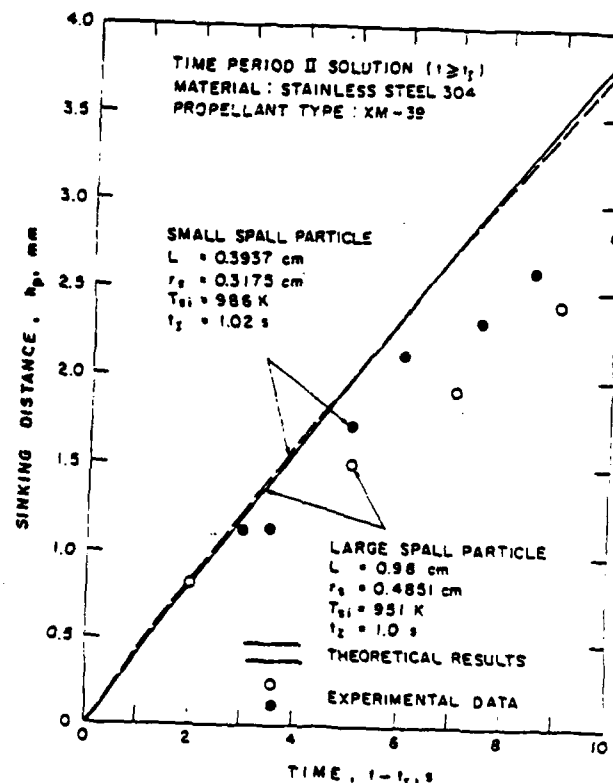


Fig. 14 Comparison of Calculated Time Variations of Sinking Distances with Experimental Data

particle has a slightly higher initial temperature than the large one, and hence sinks into the LOVA propellant at a slightly higher velocity (see Fig. 15). At a later time, the velocity of the large particle is higher since it contains more thermal energy. The calculated trajectory shown in Fig. 14 overpredicts the experimental data by 25% at the end of the run. However, the agreement is still acceptable for most of the event. For these two cases, the particles sink continuously as the propellant reaches sustained ignition conditions. The calculated sinking velocity variations with respect to time, shown in Fig. 15, exhibit spikes during the initial interval when the particles are extremely hot.

Figure 16 shows the comparison of calculated temperature-time traces at the base of the spall particle with experimental data. During the early phase, the base temperature for small particles is higher than that for large particles; the trend reverses at the later phase of Time Period II (when spall particles sink into the LOVA propellant). Calculated results are in good agreement with experimental data in terms of the trend mentioned above, as well as the magnitude and slope of these traces. It is interesting to note that the average temperature at the spall particle base drops continuously even after onset of sustained ignition; this is believed to be the result of incomplete combustion in the foam layer. Gaseous pyrolysis products in the bubbles take time to reach the fully reacted state. Heat release in the foam zone is sufficiently low to

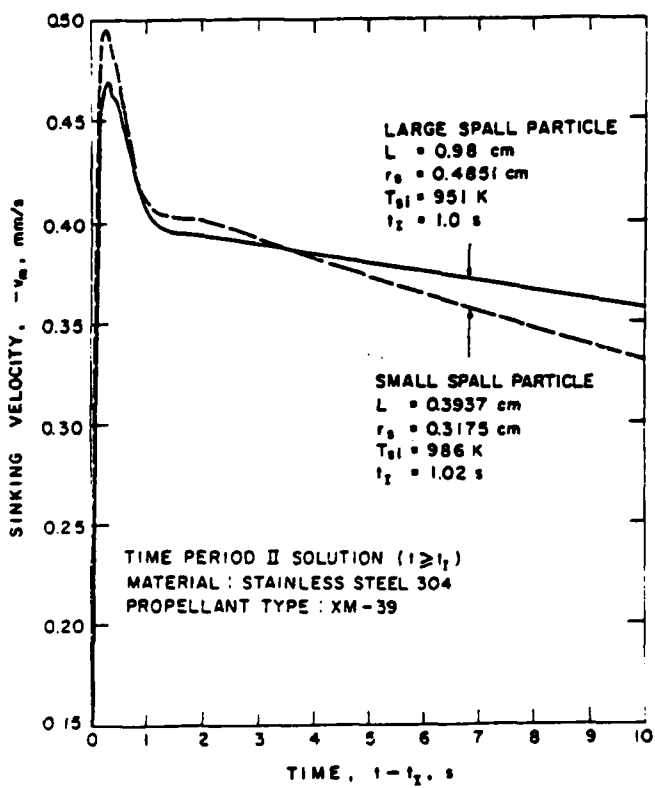


Fig. 15 Calculated Time Variations of Sinking Velocity

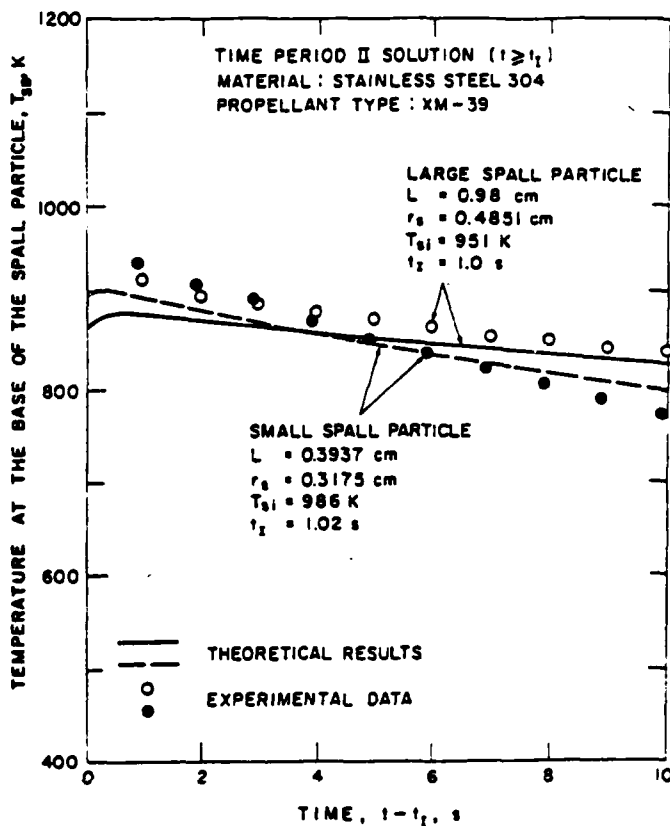


Fig. 16 Comparison of Calculated Temperature-Time Traces at the Base of the Spall Particle with Experimental Data

produce a relatively cool layer of foam material which reduces the energy of the spall particle. The above effect can be seen from the plot of the calculated bulk temperatures of the gas and liquid phases in the foam layer (see Fig. 17). The temperatures of both phases are lower than the average temperature of the spall particle base. The calculated void fraction variations with respect to time is shown in Fig. 18. After the initial intensive heating in time period II, the void fraction reduces slightly with respect to time.

Comparisons of calculated temperature-time traces at the center of spall particles with experimental data is shown in Fig. 19. Agreement is quite reasonable, and the trend is identical to that described for spall particle base. Before completion of the computation of 10 s for the time period II, the center temperatures are always higher than those at the spall particle base.

Based upon these comparisons, it is quite obvious that the HFCI model is able to predict the quenched and ignited cases using different spall particle sizes. Also, by comparing results of the small particle ($L = 0.3937 \text{ cm}$, $r_s = 0.3175 \text{ cm}$) at an initial temperature of 986 K with those for the same sized particle at 1000 K, one can observe the strong difference in solution from a quenched case to a runaway ignition. According to the test data of Miller and Cohen [13], the small particle can ignite the LOVA propellant at 986 K, which is in agreement with the prediction of ignition at 986 K.

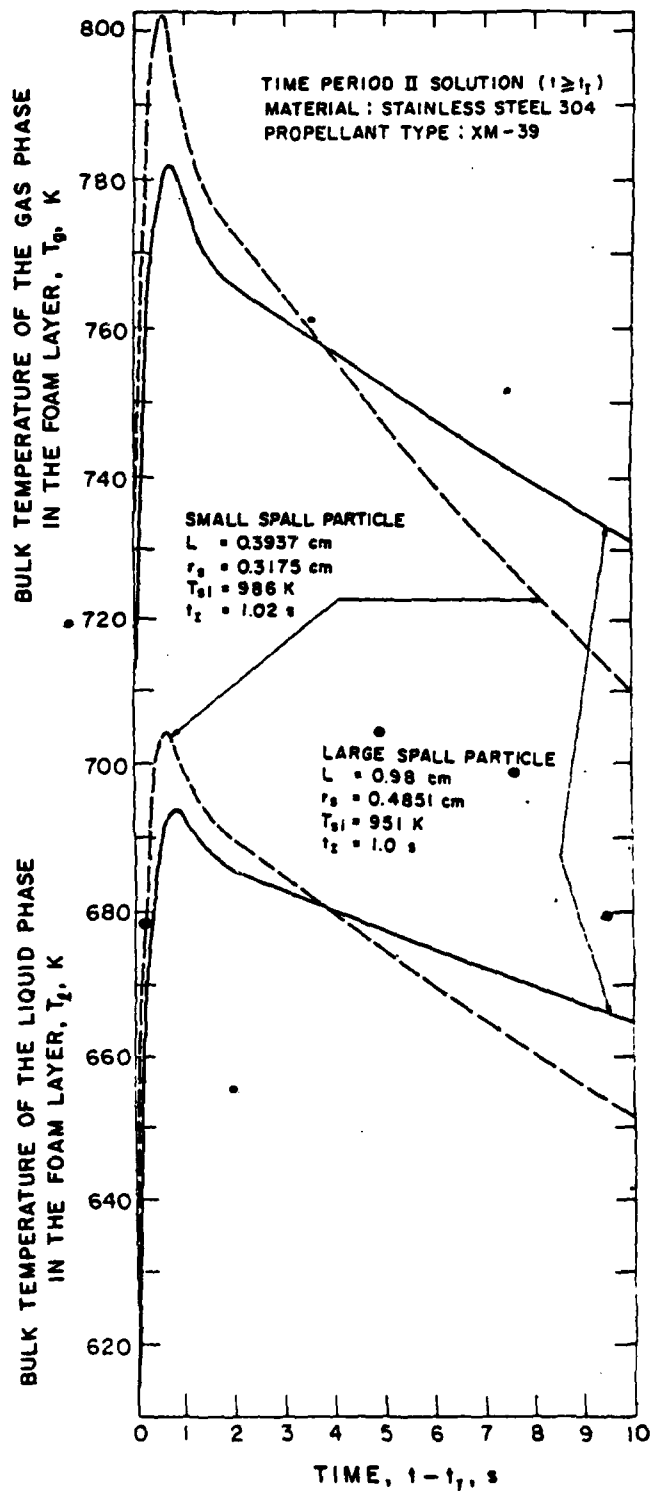


Fig. 17 Calculated Bulk Temperatures of the Gas and Liquid Phases in the Foam Layer

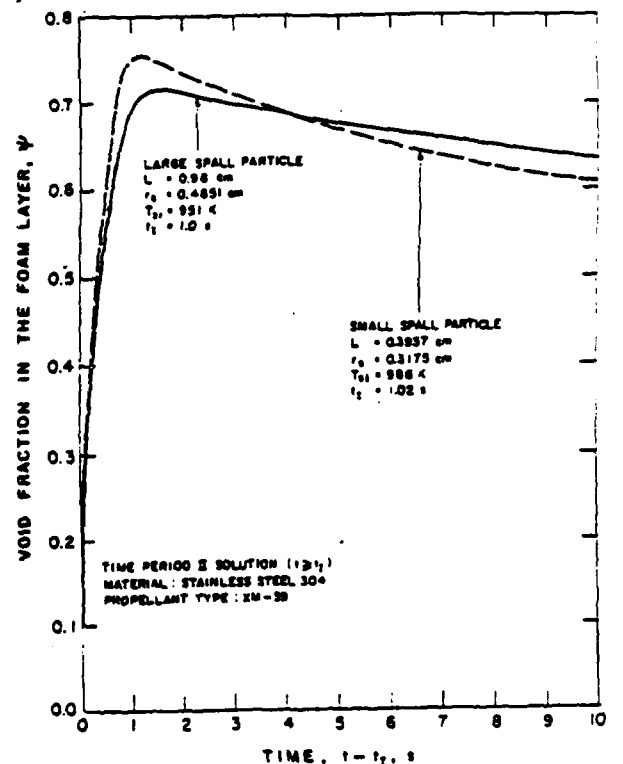


Fig. 18 Calculated Time Variations of Void Fractions in Foam Layers

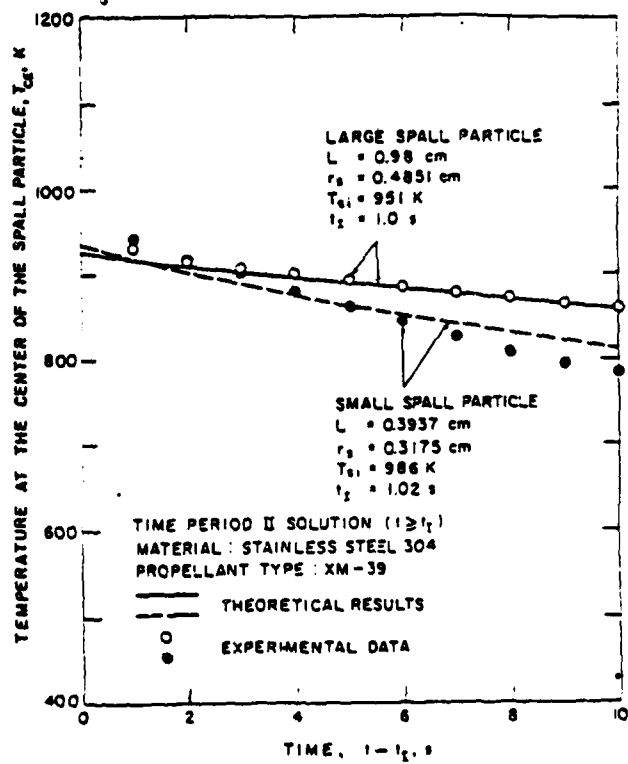


Fig. 19 Comparison of Calculated Temperature-Time Traces at the Center of Spall Particles with Experimental Data

SUMMARY AND CONCLUSIONS

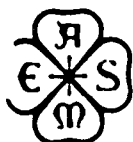
- 1) The two-step chemical kinetic mechanism, proposed by Miller et al. [8], based upon DSC measurements, was incorporated into the theoretical model [12] for simulating hot fragment conductive ignition processes of LOVA propellants.
- 2) Calculated results compared well with experimental data in temperature-time traces of spall particle and propellant.
- 3) Reasonable agreement was achieved between theoretical prediction and experimental measurements in terms of the terminal position and particle trajectory of the quenched spall particle which is partially submerged in the LOVA propellant. The predicted trajectory of the spall particle also agrees quite well with measured data for ignited cases.
- 4) The controlling mechanism in the HFCI process is the competition between the rate of heat release from exothermic reactions introduced by the spall particle and the rate of heat loss to the surrounding.
- 5) The present two-step reaction model gave a reasonable numerical solution in HFCI simulation. However, a more complicated reaction model may be needed for various types of LOVA propellants. Also, additional heat transfer correlations in the foam zone of the pyrolysis product of various propellants should be developed for more accurate predictions of HFCI processes.
- 7) From HFCI point of view, it is highly desirable to have LOVA propellants with cool pyrolysis products in the foam layer which can effectively quench the hot spall particle. Also, it is desirable to have LOVA propellants which require extended distances for development of flames.

REFERENCES

1. Gol'dshleger, U. I., Barzykin, V. V., Ivleva, T. P., "Ignition of Condensed Explosives by a Hot Spherical Particle," Combustion, Explosion and Shock Waves, Vol. 9, No. 5, 1973, pp. 642-647.
2. Wise, S., Rocchio, J. J., and Reeves, H. F., "The Ignitability of Composite Nitramine Propellants," Proceedings of the 17th JANNAF Combustion Meeting, CPIA Publication 329, Vol. III, 1980, pp. 457-475.
3. Law, H. C. and Rocchio, J. J., "The Hot Fragment Conductive Ignition Test: A Means of Evaluating Propellant Vulnerability to Spall," Proceedings of the 18th JANNAF Combustion Meeting, CPIA Publication 347, Vol. II, 1981, pp. 321-334.
4. Wise, S. and Rocchio, J. J., "Binder Requirements for Low Vulnerability Propellants," Proceedings of the 18th JANNAF Combustion Meeting, CPIA Publication 347, Vol. II, 1981, pp. 305-320.
5. Kirshenbaum, M. S., Avrami, L., and Strauss, B., "Sensitivity Characterization of Low Vulnerability (LOVA) Propellants," U.S. Army ARRADCOM Technical Report, ARLCD-TR-83005, March 1983.
6. Cohen, A., Miller, M. S., and Holmes, H. E., "Hot Fragment Ignition of LOVA and NC Propellants," Proceedings of 22nd JANNAF Combustion Meeting, CPIA Publication 432, Vol. II, 1985, pp. 529-536.
7. Cohen, A., Miller, M. S., and Holmes, H. E., "Thermocouple Measurements During Fragment Ignition of Propellant Powders," Proceedings of 23rd JANNAF Combustion Meeting, CPIA Publication 457, Vol. II, 1986, pp. 337-342.
8. Miller, M. S., Kotlar, A. J., Cohen, A., Truong, K., Puckett, D. L., and Holmes, H. E., "Effective Ignition Kinetics for LOVA Propellant," Proceedings of 23rd JANNAF Combustion Meeting, CPIA Publication 457, Vol. II, 1986, pp. 55-62.
9. Vilyunov, V. N. and Kolchin, A. K., "Ignition of Condensed Explosives by Conductive Heat Transfer from Media with Poor Thermal Conductivity," Combustion, Explosion and Shock Waves, Vol. 2, No. 3, 1966, pp. 61-65.
10. Gol'dshleger, U. I., Pribytkova, K. V., and Barzykin, V. V., "Ignition of a Condensed Explosive by a Hot Object of Finite Dimensions," Combustion, Explosions, and Shock Waves, Vol. 9, No. 1, 1973, pp. 99-102.
11. Linan, A. and Kindelan, M., "Ignition of a Reactive Solid by an Inert Hot Spot," Combustion in Reactive Systems, edited by J. Ray Bowen et al., Progress in Astronautics and Aeronautics, Vol. 76, 1981, pp. 412-426.
12. Kuo, K. K., Hsieh, W. H., Hsieh, K. C., and Miller, M. S., "Simulation of Hot Fragment Conductive Ignition Processes of Solid Propellants," presented at the ASME Winter Annual Meeting, Paper No. 86-WA/HT-13, 1986.
13. Miller, M. S. and Cohen, A., private communication, Jan.-Aug. 1987.
14. Rohsenow, W. M. and Hartnett, J. P. (ed.), Handbook of Heat Transfer, Chapter 13, 1973, pp. 13-65 and 13-66.
15. Boggs, T. L., "Thermal Behavior of RDX and HMX," Chapter 3 of Fundamentals of Solid-Propellant Combustion, edited by K. K. Kuo and M. Summerfield, Progress in Astronautics and Aeronautics, Vol. 90, Nov. 1984.
16. Robertson, A. J. B., "The Thermal Decomposition of Explosives, Part II: Cyclotrimethylenetrinitramine and Cyclotetramethylene-tetranitramine," Transactions of the Faraday Society, Vol. 45, 1949, p. 85.
17. Incopera, F. P. and DeWitt, D. P., Fundamentals of Heat Transfer, John Wiley & Sons, Inc., Appendix A, 1981, pp. 761-792.
18. Anon., Handbook of Chemistry and Physics, 63rd Edition, The Chemical Rubber Co., 1983.
19. Kuo, K. K., Principles of Combustion, Wiley, Chap. 9, 1986, pp. 668-673.
20. Rohsenow, W. M. and Hartnett, J. P. (ed.), Handbook of Heat Transfer, Chapter 13, 1973, pp. 13-65 and 13-66.

Attachment 4

Notice of Publication Acceptance



The American Society of Mechanical Engineers

JOURNAL OF HEAT TRANSFER

Contributions to Transactions of ASME by the Heat Transfer Division

16 December 1987

Senior Technical Editor
Professor Gerard M. Faeth
Aerospace Engineering Department
The University of Michigan
Ann Arbor, Michigan 48109-2140

(313) 764-7200

Professor K.K. Kuo
The Pennsylvania State University
208 Mechanical Engineering Building
University Park, PA 16802

Reference: Paper No. 87-F-509, K.K. Kuo, W.H. Hsieh, K.C. Hsieh, M.S. Miller

Dear Ken:

I am very pleased to inform you that the above-referenced full length paper is accepted for publication in the Journal of Heat Transfer. It has been routed to ASME. You will receive galley proofs directly from them.

Your contribution to the journal is appreciated.

With best regards.

Sincerely,

G.M. Faeth

GMF:sc
cc: W.A. Sirignano

DISTRIBUTION LIST

<u>No. Of Copies</u>	<u>Organization</u>	<u>No. Of Copies</u>	<u>Organization</u>
12	Administrator Defense Technical Info Center ATTN: DTIC-DDA Cameron Station Alexandria, VA 22304-6145	1	Commander US Army Aviation Systems Command ATTN: AMSAV-DACL 4300 Goodfellow Blvd. St. Louis, MO 63120-1798
1	HQ DA (SARD-TR) Washington, DC 20310-0001	1	Director US Army Aviation Research and Technology Activity Ames Research Center Moffett Field, CA 94035-1099
1	Commander US Army Materiel Command ATTN: AMCDRA-ST 5001 Eisenhower Avenue Alexandria, VA 22333-0001	4	Commander US Army Research Office ATTN: R. Ghirardelli D. Mann R. Singleton R. Shaw P.O. Box 12211 Research Triangle Park, NC 27709-2211
1	Commander US Army Laboratory Command ATTN: AMSLC-DL Adelphi, MD 20783-1145		
1	Commander Armament RD&E Center US Army AMCCOM ATTN: SMCAR-MSI Picatinny Arsenal, NJ 07806-5000	1	Commander US Army Communications - Electronics Command ATTN: AMSEL-ED Fort Monmouth, NJ 07703-5022
1	Commander Armament RD&E Center US Army AMCCOM ATTN: SMCAR-TDC Picatinny Arsenal, NJ 07806-5000	2	Commander Armament R&D Center US Army AMCCOM ATTN: SMCAR-LCA-G, D.S. Downs J.A. Lannon Dover, NJ 07801
1	Director Benet Weapons Laboratory Armament RD&E Center US Army AMCCOM ATTN: SMCAR-LCB-TL Watervliet, NY 12189-4050	1	Commander Armament R&D Center US Army AMCCOM ATTN: SMCAR-LC-G, L. Harris Dover, NJ 07801
1	Commander US Army Armament, Munitions and Chemical Command ATTN: SMCAR-ESP-L Rock Island, IL 61299-5000		

DISTRIBUTION LIST

<u>No. Of Copies</u>	<u>Organization</u>	<u>No. Of Copies</u>	<u>Organization</u>
1	Commander Armament R&D Center US Army AMCCOM ATTN: SMCAR-SCA-T, L. Stiefel Dover, NJ 07801	1	Commander Naval Air Systems Command ATTN: J. Ramnarace, AIR-54111C Washington, DC 20360
2	Commander US Army Missile Command ATTN: AMSMI-RD AMSMI-AS Redstone Arsenal, AL 35898-5000	1	Commander Naval Surface Weapons Center ATTN: J.L. East, Jr., G-23 Dahlgren, VA 22448-5000
2	Commander US Army Missile Command ATTN: AMSMI-RK, D.J. Ifshin W. Wharton Redstone Arsenal, AL 35898	2	Commander Naval Surface Weapons Center ATTN: R. Bernecker, R-13 G.B. Wilmot, R-16 Silver Spring, MD 20902-5000
1	Commander US Army Missile Command ATTN: AMSMI-RKA, A.R. Maykut Redstone Arsenal, AL 35898-5249	5	Commander Naval Research Laboratory ATTN: M.C. Lin J. McDonald E. Oran J. Shnur R.J. Doyle, Code 6110 Washington, DC 20375
1	Commander US Army Tank Automotive Cmd ATTN: AMSTA-TSL Warren, MI 48397-5000	1	Commanding Officer Naval Underwater Systems Center Weapons Dept. ATTN: R.S. Lazar/Code 36301 Newport, RI 02840
1	Director US Army TRADOC Analysis Cmd ATTN: ATAA-SL White Sands Missile Range, NM 88002-5502	1	Superintendent Naval Postgraduate School Dept. of Aeronautics ATTN: D.W. Netzer Monterey, CA 93940
1	Commandant US Army Infantry School ATTN: ATSH-CD-CSO-OR Fort Benning, GA 31905-5660	4	AFRPL/DY, Stop 24 ATTN: R. Corley R. Geisler J. Levine D. Weaver Edwards AFB, CA 93523-5000
1	Office of Naval Research Department of the Navy ATTN: R.S. Miller, Code 432 800 N. Quincy Street Arlington, VA 22217	1	AFRPL/MKPR, Stop 24 ATTN: B. Goshgarian Edwards AFB, CA 93523-5000

DISTRIBUTION LIST

<u>No. Of Copies</u>	<u>Organization</u>	<u>No. Of Copies</u>	<u>Organization</u>
1	AFOSR ATTN: J.M. Tishkoff Bolling Air Force Base Washington, DC 20332	1	Atlantic Research Corp. ATTN: M.K. King 5390 Cherokee Avenue Alexandria, VA 22314
1	AFWL/SUL Kirtland AFB, NM 87117-5800	1	Atlantic Research Corp. ATTN: R.H.W. Waesche 7511 Wellington Road Gainesville, VA 22065
1	Air Force Armament Laboratory ATTN: AFATL/DLODL Eglin AFB, FL 32542-5000	1	AVCO Everett Rsch. Lab. Div. ATTN: D. Stickler 2385 Revere Beach Parkway Everett, MA 02149
1	NASA Langley Research Center Langley Station ATTN: G.B. Northam/MS 168 Hampton, VA 23365	1	Battelle Memorial Institute Tactical Technology Center ATTN: J. Huggins 505 King Avenue Columbus, OH 43201
4	National Bureau of Standards ATTN: J. Hastie M. Jacox T. Kashiwagi H. Semerjian US Department of Commerce Washington, DC 20234	1	Cohen Professional Services ATTN: N.S. Cohen 141 Channing Street Redlands, CA 92373
1	OSD/SDIO/UST ATTN: L.H. Caveny Pentagon Washington, DC 20301-7100	1	Exxon Research & Eng. Co. ATTN: A. Dean Route 22E Annandale, NJ 08801
1	Aerojet Solid Propulsion Co. ATTN: P. Micheli Sacramento, CA 95813	1	Ford Aerospace and Communications Corp. DIVAD Division Div. Hq., Irvine ATTN: D. Williams Main Street & Ford Road Newport Beach, CA 92663
1	Applied Combustion Technology, Inc. ATTN: A.M. Varney P.O. Box 17885 Orlando, FL 32860	1	General Applied Science Laboratories, Inc. 77 Raynor Avenue Ronkonkoma, NY 11779-6649
2	Applied Mechanics Reviews The American Society of Mechanical Engineers ATTN: R.E. White A.B. Wenzel 345 E. 47th Street New York, NY 10017	1	General Electric Armament & Electrical Systems ATTN: M.J. Bulman Lakeside Avenue Burlington, VT 05401

DISTRIBUTION LIST

<u>No. Of Copies</u>	<u>Organization</u>	<u>No. Of Copies</u>	<u>Organization</u>
1	General Electric Company 2352 Jade Lane Schenectady, NY 12309	1	Lockheed Missiles & Space Co. ATTN: George Lo 3251 Hanover Street Dept. 52-35/B204/2 Palo Alto, CA 94304
1	General Electric Ordnance Systems ATTN: J. Mandzy 100 Plastics Avenue Pittsfield, MA 01203	1	Los Alamos National Lab ATTN: B. Nichols T7, MS-B284 P.O. Box 1663 Los Alamos, NM 87545
2	General Motors Rsch Labs Physics Department ATTN: T. Sloan R. Teets Warren, MI 48090	1	National Science Foundation ATTN: A.B. Harvey Washington, DC 20550
2	Hercules, Inc. Allegany Ballistics Lab. ATTN: R.R. Miller E.A. Yount P.O. Box 210 Cumberland, MD 21501	1	Olin Corporation Smokeless Powder Operations ATTN: V. McDonald P.O. Box 222 St. Marks, FL 32355
1	Honeywell, Inc. Government and Aerospace Products ATTN: D.E. Broden/ MS MN50-2000 600 2nd Street NE Hopkins, MN 55343	1	Paul Gough Associates, Inc. ATTN: P.S. Gough 1048 South Street Portsmouth, NH 03801-5423
1	IBM Corporation ATTN: A.C. Tam Research Division 5600 Cottle Road San Jose, CA 95193	2	Princeton Combustion Research Laboratories, Inc. ATTN: M. Summerfield N.A. Messina 475 US Highway One Monmouth Junction, NJ 08852
1	IIT Research Institute ATTN: R.F. Remaly 10 West 35th Street Chicago, IL 60616	1	Hughes Aircraft Company ATTN: T.E. Ward 8433 Fallbrook Avenue Canoga Park, CA 91303
2	Director Lawrence Livermore National Laboratory ATTN: C. Westbrook M. Costantino P.O. Box 808 Livermore, CA 94550	1	Rockwell International Corp. Rocketdyne Division ATTN: J.E. Flanagan/HB02 6633 Canoga Avenue Canoga Park, CA 91304

DISTRIBUTION LIST

<u>No. Of Copies</u>	<u>Organization</u>	<u>No. Of Copies</u>	<u>Organization</u>
4	Sandia National Laboratories Combustion Sciences Dept. ATTN: R. Cattolica S. Johnston P. Mattern D. Stephenson Livermore, CA 94550	1	United Technologies ATTN: A.C. Eckbreth East Hartford, CT 06108
1	Science Applications, Inc. ATTN: R.B. Edelman 23146 Cumorah Crest Woodland Hills, CA 91364	3	United Technologies Corp. Chemical Systems Division ATTN: R.S. Brown T.D. Myers (2 copies) P.O. Box 50015 San Jose, CA 95150-0015
1	Science Applications, Inc. ATTN: H.S. Pergament 1100 State Road, Bldg. N Princeton, NJ 08540	1	Universal Propulsion Company ATTN: H.J. McSpadden Black Canyon Stage 1 Box 1140 Phoenix, AZ 85029
3	SRI International ATTN: G. Smith D. Crosley D. Golden 333 Ravenswood Avenue Menlo Park, CA 94025	1	Veritay Technology, Inc. ATTN: E.B. Fisher 4845 Millersport Highway P.O. Box 305 East Amherst, NY 14051-0305
1	Stevens Institute of Tech. Davidson Laboratory ATTN: R. McAlevy, III Hoboken, NJ 07030	1	Brigham Young University Dept. of Chemical Engineering ATTN: M.W. Beckstead Provo, UT 84601
1	Thiokol Corporation Elkton Division ATTN: W.N. Brundige P.O. Box 241 Elkton, MD 21921	1	California Institute of Tech. Jet Propulsion Laboratory ATTN: MS 125/159 4800 Oak Grove Drive Pasadena, CA 91103
1	Thiokol Corporation Huntsville Division ATTN: R. Glick Huntsville, AL 35807	1	California Institute of Technology ATTN: F.E.C. Culick/ MC 301-46 204 Karman Lab. Pasadena, CA 91125
3	Thiokol Corporation Wasatch Division ATTN: S.J. Bennett P.O. Box 524 Brigham City, UT 84302	1	University of California, Berkeley Mechanical Engineering Dept. ATTN: J. Daily Berkeley, CA 94720

DISTRIBUTION LIST

<u>No. Of Copies</u>	<u>Organization</u>	<u>No. Of Copies</u>	<u>Organization</u>
1	University of California Los Alamos Scientific Lab. P.O. Box 1663, Mail Stop B216 Los Alamos, NM 87545	1	University of Illinois Dept. of Mech. Eng. ATTN: H. Krier 144MEB, 1206 W. Green St. Urbana, IL 61801
2	University of California, Santa Barbara Quantum Institute ATTN: K. Schofield M. Steinberg Santa Barbara, CA 93106	1	Johns Hopkins University/APL Chemical Propulsion Information Agency ATTN: T.W. Christian Johns Hopkins Road Laurel, MD 20707
2	University of Southern California Dept. of Chemistry ATTN: S. Benson C. Wittig Los Angeles, CA 90007	1	University of Michigan Gas Dynamics Lab Aerospace Engineering Bldg. ATTN: G.M. Faeth Ann Arbor, MI 48109-2140
1	Case Western Reserve Univ. Div. of Aerospace Sciences ATTN: J. Tien Cleveland, OH 44135	1	University of Minnesota Dept. of Mechanical Engineering ATTN: E. Fletcher Minneapolis, MN 55455
1	Cornell University Department of Chemistry ATTN: T.A. Cool Baker Laboratory Ithaca, NY 14853	3	Pennsylvania State University Applied Research Laboratory ATTN: K.K. Kuo H. Palmer M. Micci University Park, PA 16802
1	Univ. of Dayton Rsch Inst. ATTN: D. Campbell AFRPL/PAP Stop 24 Edwards AFB, CA 93523	1	Pennsylvania State University Dept. of Mechanical Engineering ATTN: V. Yang University Park, PA 16802
1	University of Florida Dept. of Chemistry ATTN: J. Winefordner Gainesville, FL 32611	1	Polytechnic Institute of NY Graduate Center ATTN: S. Lederman Route 110 Farmingdale, NY 11735
3	Georgia Institute of Technology School of Aerospace Engineering ATTN: E. Price W.C. Strahle B.T. Zinn Atlanta, GA 30332	2	Princeton University Forrestal Campus Library ATTN: K. Brezinsky I. Glassman P.O. Box 710 Princeton, NJ 08540

DISTRIBUTION LIST

<u>No. Of Copies</u>	<u>Organization</u>	<u>No. Of Copies</u>	<u>Organization</u>
1	Princeton University MAE Dept. ATTN: F.A. Williams Princeton, NJ 08544	1	Virginia Polytechnic Institute and State University ATTN: J.A. Schetz Blacksburg, VA 24061
1	Purdue University School of Aeronautics and Astronautics ATTN: J.R. Osborn Grissom Hall West Lafayette, IN 47906	1	Commandant USAFAS ATTN: ATSF-TSM-CN Fort Sill, OK 73503-5600
1	Purdue University Department of Chemistry ATTN: E. Grant West Lafayette, IN 47906	1	F.J. Seiler Research Lab (AFSC) ATTN: S.A. Shakelford USAF Academy, CO 80840-6528
2	Purdue University School of Mechanical Engineering ATTN: N.M. Laurendeau S.N.B. Murthy TSPC Chaffee Hall West Lafayette, IN 47906	1	Freedman Associates ATTN: E. Freedman 2411 Diana Road Baltimore, MD 21209-1525
1	Rensselaer Polytechnic Inst. Dept. of Chemical Engineering ATTN: A. Fontijn Troy, NY 12181	<u>Aberdeen Proving Ground</u>	
1	Stanford University Dept. of Mechanical Engineering ATTN: R. Hanson Stanford, CA 94305	Dir, USAMSAA ATTN: AMXSY-D AMXSY-MP, H. Cohen	
1	University of Texas Dept. of Chemistry ATTN: W. Gardiner Austin, TX 78712	Cdr, USATECOM ATTN: AMSTE-TO-F	
1	University of Utah Dept. of Chemical Engineering ATTN: G. Flandro Salt Lake City, UT 84112	Cdr, CRDEC, AMCCOM ATTN: SMCCR-RSP-A SMCCR-MU SMCCR-SPS-IL	

USER EVALUATION SHEET/CHANGE OF ADDRESS

This laboratory undertakes a continuing effort to improve the quality of the reports it publishes. Your comments/answers below will aid us in our efforts.

1. Does this report satisfy a need? (Comment on purpose, related project, or other area of interest for which the report will be used.) _____

2. How, specifically, is the report being used? (Information source, design data, procedure, source of ideas, etc.) _____

3. Has the information in this report led to any quantitative savings as far as man-hours or dollars saved, operating costs avoided, or efficiencies achieved, etc? If so, please elaborate. _____

4. General Comments. What do you think should be changed to improve future reports? (Indicate changes to organization, technical content, format, etc.) _____

BRL Report Number _____ Division Symbol _____

Check here if desire to be removed from distribution list.

Check here for address change.

Current address: Organization _____
Address _____

-----FOLD AND TAPE CLOSED-----

Director
U.S. Army Ballistic Research Laboratory
ATTN: SLCBR-DD-T(NEI)
Aberdeen Proving Ground, MD 21005-5066

OFFICIAL BUSINESS
PENALTY FOR PRIVATE USE \$300



NO POSTAGE
NECESSARY
IF MAILED
IN THE
UNITED STATES



Director
U.S. Army Ballistic Research Laboratory
ATTN: SLCBR-DD-T(NEI)
Aberdeen Proving Ground, MD 21005-9989

Director
U.S. Army Ballistic Research Laboratory
ATTN: SLCBR-DD-T(NEI)
Aberdeen Proving Ground, MD 21005-5066

- PASTE LABEL HERE -